CHEMI-IONISATION PROCESSES IN GAS PHASE METAL OXIDATION REACTIONS

A Thesis submitted to the University of Southampton
for the degree of Master of Philosophy

Andrew Mark Shaw, BA

Department of Chemistry
University of Southampton

October 1990

It looked cockeyed, but in reality it was not:
it was the theory of quantum mechanics.

Richard Feynman

Memorandum

This thesis is an account of original research performed by the author in the Department of Chemistry, University of Southampton, between October 1989 and August 1990. Where findings of other works have been used, due reference has been given.

Acknowledgements

I should like to thank my supervisor Professor John Dyke for his advice and many stimulating discussions during the period of this work. I am indebted to Dr. Tamas Veszpremi with whom I worked closely and learnt a great deal. Gratitude is also due to many unnamed colleagues that have provided a stimulating atmosphere for research. Finally, I should like to thank the USAF for the sponsorship of the project.

I am deeply grateful for the continuing support and humour of my parents and brother throughout my years of study.

UNIVERSITY OF SOUTHAMPTON

ABSTRACT

FACULTY OF SCIENCE

CHEMISTRY

Master of Philosophy

CHEMI-IONISATION PROCESSES IN GAS PHASE METAL OXIDATION REACTIONS

by Andrew Mark Shaw

The work presented in this thesis is a study of chemi-ionisation processes in gas phase metal oxidation reactions in relation to atmospheric meteor chemistry. The majority of the work has concentrated on experimental development of an existing electron spectrometer to tailor its performance to the study of chemi-ionisation reactions. A new furnace assembly has been has been designed and implemented and a 600 a.m.u. quadrupole mass spectrometer has been incorporated in the ionisation chamber of the electron spectrometer. This allowed observed electron spectra to be correlated with observed ion signals.

A series of investigations has been undertaken to study the gas phase oxidation reactions of the alkaline earth metals Mg, Ca, Sr, and Ba with the oxidants $O_2(X^3\Sigma_g^-)$, $O_2(a^1\Delta_g)$ and $O(^3P)$. The results have been interpreted in terms of a simple thermodynamic model that was consistent with the reactions proceeding *via* long lived collision intermediates. The electron energy distributions were interpreted in terms of a simple potential energy curve model. The possibility of the inclusion of an associative ionisation reaction into a kinetic model of metal chemistry in the upper atmosphere is considered.

Contents

Chapter 1

Introduction.

The formation of ions from the collision of two neutral species is an important elementary process in many gas phase reactions. One such reaction is that of chemi-ionisation. Following Fontijn (1,2), a chemi-ionisation process may be defined as " a process by which the number of elementary charge carriers is increased as a direct result of the formation of new chemical bonds.". A chemi-ionisation process was first proposed to explain the presence of ions in irradiated Cs and Hg vapour when the wavelength of the radiation was longer than that required for atomic ionisation (3,4). The formation of ions was attributed to the following process:

1.1 $$Cs + h\nu \rightarrow Cs(mP)$$
$$Cs(mP) + Cs \rightarrow Cs_2^+ + e^-$$

(where Cs(mP) is an excited state of caesium). Since their discovery, chemi-ionisation processes have been used to explain ionisation phenomena in a diverse array of disciplines from upper atmosphere chemistry (5) and hydrocarbon flame chemistry (6) to ionisation in shock waves (7) and detonations (8). Most of the early investigations have been reviewed elsewhere (1,2).

The chemi-ionisation reaction is one of a number of possible reactions that can occur on collision of two neutral particles. Disposal of the available reactant electronic energy makes a variety of processes possible leading to excited products which may chemiluminesce, or to ground state neutral products, energy being conserved within any given reaction (9,10). Aside from the 'dark' neutral channels and the chemiluminescent neutral channels, there are a range of ionic reaction pathways which may be broadly classified into five simple classes:

1.2	$A + BC \rightarrow A^+ + BC + e^-$	Simple Ionisation
1.3	$A + BC \rightarrow ABC^+ + e^-$	Associative Ionisation
1.4	$A + BC \rightarrow A + B + C^+ + e^-$	Dissociative Ionisation
1.5	$A + BC \rightarrow AB^+ + C + e^-$	Re-arrangement Ionisation
1.6	$A^* + BC \rightarrow A + BC^+ + e^-$	Penning ionisation

where A^* denotes an atom in an electronically excited state.

Only processes 1.3 and 1.5 may be classified as chemi-ionisation reactions according to Fontijn's definition. Most of the processes 1.2 to 1.5 are endothermic for reactants in their ground states (conversely the reverse reactions are strongly exothermic). However there are some metal gas phase

oxidation reactions which are exothermic for ground state reactants and these are the subject of this work.

Metal oxidation reactions are of special importance in atmospheric chemistry with regard to the ablation of meteors. According to radar observations the flux of meteor material into the Earth's atmosphere is about 10^5 Kg daily (11). The ablation process occurs at altitudes of 80 - 100 km in the upper atmosphere. The ablated meteor material forms isolated regions in the atmosphere known as Sporadic E Regions (12,13), but the mechanism of formation whilst much studied, is little understood. Anomalous radar echoes from these regions, first observed during the Second World War, are thought to be due to the presence of ions. The processes leading to ionisation are of scientific and military interest. Scientifically, the scattering phenomenon has been developed into the technique of meteor radar used to study the composition of the upper atmosphere (14).

Ionised material derived from meteors in the atmosphere is known to be responsible for the scattering of electromagnetic radiation from sporadic E regions. Calculations suggest that the electron/ion density is too high to be entirely due to ionisation by short wavelength solar radiation (11). This suggests that other processes, possibly chemi-ionisation reactions, are responsible for some of the ionisation especially at night. In considering the possibility of chemi-ionisation, some knowledge of the chemical composition of meteors and meteorites is required. All elements known on Earth are present to a greater or lesser extent in meteorite samples analysed to date (15). A few non-terrestrial minerals have been identified: the actual mineral composition being a property dependent on the history of the meteorite (16). The observed metal content of the atmosphere correlates well with known meteor composition (8), the most abundant metals being Fe, Mg, Ni, Ca, and Sc, and the non-metal Si. Sr and Ba are present in trace quantities, a few ppm, but Ba is added to the atmosphere as a tracer for upper atmospheric wind patterns (17). A further important consideration is the translational energy of the meteor material. A meteor is thought to enter the atmosphere with speeds of between 11 km/s and 100 km/s. Thus knowledge of reactions at hyperthermal collisions energies will be important in determining the role of chemi-ionisation reactions in the chemistry of metals in the upper atmosphere.

A further consideration is the composition of the upper atmosphere since this determines the possible collision partners for metal oxidation reaction. A large number of molecules in the upper atmosphere are ionised or in excited states as a result of absorption of solar radiation (18,19). Therefore, some investigation of reactions involving neutral excited species, will also provide information to assist the understanding of chemi-ionisation processes in sporadic E region chemistry.

The simplest chemi-ionisation process is that of associative ionisation (equation 1.3) for which a thermodynamic balance enables an estimation to be made of the available energy for the emitted electron; i.e. for the process,

1.7 $$A + B \rightarrow AB^+ + e^-$$

The emitted electron may have a maximum kinetic energy, E_e, given by

1.8 $$E_e = IE(AB) - D_0(AB)$$

where E_e is the maximum electron energy, IE is the first ionisation energy and D_0 is the dissociation energy of AB. This expression assumes that the product ion is formed in its ground electronic state. For most metal compounds, reactions 1.2 -1.5 are strongly endothermic and if the reactions are to occur this endothermicity has to be overcome. This can be achieved in two ways. Either the reactants can be involved in hyperthermal collisions where the relative translational energy provides the excess energy (20) or one of the reactants may be excited electronically, usually a noble gas metastable (Penning ionisation). However there are some lanthanide metal oxidation reactions for which process 1.3, associative ionisation, is exothermic for reactants in their ground states (2,21). The lanthanide monoxides have strong metal oxygen bonds but low ionisation energies. This has been discussed in the context of the lanthanide contraction present across the lanthanide series (22,23).

In the case of electronically excited reactants the symmetry of the excited state may be important providing information on state-to-state correlated reaction cross-sections (24,25). For translationally excited reactants, the threshold region is of most interest giving information on the relative velocity dependence of the transition probability.

The most commonly used experimental technique, with the exception of electron spectroscopy, monitors the progress of a chemi-ionisation reaction by detecting the ions using mass spectrometry. This has led to some determinations of absolute reaction cross-sections by study of chemi-ionisation reactions under molecular beam conditions (26,27,28). This is achieved by comparing the product ion current of the reaction of interest with the product ion current of a reaction with a known absolute cross-section and reagent concentrations. The chosen standard is (26)

1.9 $$U + O_2 \rightarrow UO_2^+ + e^-$$

The cross-section for the reaction is $\sigma = 1.68 \pm 0.27 \times 10^{-17}$ cm^2 (ie.$\approx$0.1A^2). This was an unfortunate choice of standard as there are thought to be nearly 200 potential energy surfaces correlating different electronic states in the reactants with states in the ion which are populated at the temperatures of evaporation, 2000 K. The observed cross-section represents the sum of all the allowed state-to-state cross-sections, modified by the electronic partition function such that any given state-to-state reaction may have a larger cross-section but is only poorly populated. The U + O_2 cross-section is lower than those observed for associative ionisation leading to the formation of noble gas dimers which are typically 50 A^2 (29,30). The large reaction cross-sections have been explained by invoking a long-range electron transfer such as the harpooning mechanism (31,32) which is thought to occur early on in the collision. This mechanism is thought to occur in the reactions of alkaline metals with halogen molecules (31).

The majority of investigations to date have studied chemi-ionisation processes involving electronically excited reactants (1,2), usually noble gases or metals, but recently in this laboratory attention has been directed towards those reactions for which both reactants are in their ground electronic states (21). The thermodynamic balance, equation 1.8, suggests that for the reaction to be exothermic the formation of a strong chemical bond must be associated with a molecule having a low ionisation energy. The lanthanide metals with oxidants such as $O_2(X^3\Sigma_g^-)$, $O_2(a^1\Delta_g)$, $O(^3P)$, $O_3(X^1A_1)$, $N_2O(X^1\Sigma^+)$ and $OH(X^2\Pi)$ are candidates for such processes. The technique of Chemi-Electron Spectroscopy has been used to study some of these reactions (21,33), and, by using the high kinetic energy onset of the observed electron energy distribution an estimate of the reaction enthalpy may be obtained. The first reaction to be studied using this technique was:

1.10 $$O(^3P) + CH(X^2\Pi) \rightarrow HCO^+(X^1\Sigma^+) + e^-$$

by Jonathan *et al* (34), where the band maximum of the electron kinetic energy was measured as 0.23 ± 0.02 eV comparing favourably with the reaction enthalpy ΔH=-0.18 ± 0.03 eV, determined from available thermodynamic data. This reaction is now the subject of further study (35).

The chemi-ionisation reaction of uranium with oxygen has also been studied by chemi-electron spectroscopy (36,37) because of its importance as a standard in determining reaction cross-sections and its large ground state reaction enthalpy (equation 1.7). The chemi-electron spectrum recorded for this reaction showed one band with an electron kinetic energy maximum of 0.67 ± 0.08 eV, and a long tail to higher kinetic energy. The spectrum was initially thought to be due to the reaction,

1.11 $$U + O_2 \rightarrow UO_2^+ + e^-$$

However, kinetic modelling of the U + O_2 reaction under the experimental effusive beam conditions suggests the observed spectrum arises from the following process,

1.11 a) $$U + O_2 \rightarrow UO + O$$

b) $$U + O \rightarrow UO^+ + e^-$$

This conclusion is consistent with the ratio of the observed reaction cross-sections for the two associative ionisation channels, 1.10 and 1.11 b) (26). The high kinetic energy onset from the observed chemi-electron band compares more favourably with the reaction enthalpy for the formation of UO^+, 1.11, than for the formation of UO_2^+, 1.10. It will be useful to confirm this by measurement of the electron and ion spectra simultaneously - this is now possible with the developments made during the period of this work.

The objective of this present work is to design and implement modifications to an existing electron spectrometer to allow measurement of chemi-ions and chemi-electrons from chemi-ionisation reactions within the same experiment. This was achieved by inclusion of a 600 a.m.u. quadrupole mass spectrometer to allow study of reactions of metals potentially important in meteor chemistry. The results obtained within this work will be interpreted in terms of a simple potential energy surface model with some refinements.

In the following chapters a description of the experimental methods used and details of the modifications will be given. Present theoretical understanding of chemi-ionisation will be reviewed as it pertains to the interpretation of experimental results. The results of a series of investigations into oxidation reactions of the alkaline earth metals and metal oxides with oxygen and water will be presented and discussed. Prospects for future experiments will be considered.

References

(1) A.Fontijn. *Prog.React.Kinet.* 6,75,(1971).

(2) A.Fontijn. *Pure and Applied Chemistry* 39(3),287,(1974).

(3) F.L.Mohler, P.D.Foote & R.L.Chenault. *Phys.Rev.* 26,195,(1926).

(4) F.L.Arnot & J.C.Milligan. *Proc.Roy.Soc.* A153,359,(1936).

(5) T.L.Brown. *Chem.Rev.* 73,645,(1973).

(6) H.G.Calcote. *Combust.Flame.* 42,215,(1981).

(7) S.Matsuda & D.Gutman. *J.Chem.Phys.* 54,453,(1971).

(8) T.L.Brown. *Chem.Rev.* 73,645,(1973).

(9) A.Kowalski & M.Menzinger. *J.Phys.Chem* 94,1899,(1990).

(10) M.Menzinger. *Adv.Chem.Phys* 42,1,(1980).

(11) V.N.Lebedinets & V.B.Shusukova. *Geomag.Aeron.* 14,228,(1974).

(12) J.D.Whitehead. *Rev.Geophys.Space.Phys.* 8,65,(1970).

(13) J.D.Whitehead. *J.Atm.Terrest.Phys.* 51,401,(1989).

(14) S.K.Avery. *Adv.Space.Res.* 10,193,(1990).

(15) B.Mason. *Handbook of Elemental Abundances in Meteorites*, Gordon and Breach Science Publishers, New York (1971).

(16) B.Mason. *Meteorites*, J.Wiley & Sons, New York, (1962).

(17) S.Daputz, L.Haser & K.W.Michel. *Z.Naturforsch* A29,411,(1974)

(18) R.P.Wayne *Chemistry of Atmospheres*, Clarendon Press, Oxford (1985).

(19) A.F.Arnold in *Atmospheric Chemistry* , Ed E.D.Goldbery. Springer-Verlag, Berlin (1982).

(20) C.E.Young, R.B.Cohen & P.M.Dehmer, L.G.Pobo *J.Chem.phys* 65,2562,(1976).

(21) M.C.R.Cockett. Ph.D. Thesis, Southampton University (1990).

(22) K.S.Pitzer. *Acc.Chem.Res.* 12,271,(1979).

(23) P.Pyykko, J.P.Desclaux. *Acc.Chem.Res.* 12,278,(1979).

(24) S.Wexler. *Ber.Buns.Ges.* 77,606,(1973).

(25) T.Bregal & A.J.Yencha *et al.* *Z.Phys.D.* 13,51,(1984).

(26) W.L.Fite, H.H.Lo & P.Irving. *J.Chem.Phys* 60,1236,(1974).

(27) J.C.Halle, H.H.Lo & W.L.Fite. *J.Chem.Phys.* 73,5681,(1980).

(28) W.L.Fite, T.A.Patterson & M.W.Siegal U.S. Air Force Report, AFGL-TR-77-0030 Hanscom AFB, USA (1978).

(29) M.Menzinger in *Gas-Phase Chemiluminescence and Chemi-Ionisation*, Ed. A.Fontijn. North-Holland, Amsterdam (1985).

(30) P.M.Becker & F.W.Lampe. *J.Chem.Phys.* 42,3857,(1965).

(31) R.D.Levine & R.B.Bernstein. *Molecular Reaction Dynamics and Chemical Reactivity.* Oxford University Press, Oxford (1987).

(32) L.Barbier, A.Pesnelle & M.Cheret. *J.Phys.D* 20,1249,(1987).

(33) M.C.R.Cockett, J.M.Dyke, A.M.Ellis, M.Feher & A.Morris.
J.Am.Chem.Soc. 111,5944,(1989).

(34) N.Jonathan, A.Morris, M.Okuda & D.J.Smith.
J.Chem.Phys. 55,3046,(1971).

(35) T.G.Wright. Private Communication.

(36) M.Feher. Ph.D. Thesis, Southampton University (1987)

(37) J.Baker, M.Barnes, M.C.R.Cockett, J.M.Dyke, A.M.Ellis, M.Feher,
E.P.F.Lee, A.Morris & H.Zamanpour. *J.Elec.Spec.* 51,487,(1990).

Chapter 2

Theoretical Considerations.

The Two-State potential energy curve model - Classical Theory.

The theory for chemi-ionisation has been developed from the theory of Penning ionisation processes (1). As with Penning ionisation, chemi-ionisation reactions in the gas phase produce ionic products from the collision of two neutral molecules. The chemi-ionisation channel is one of a number of possible reaction channels that may occur on collision of two neutral atoms or molecules (2). Qualitative interpretation of Penning ionisation and chemi-ionisation has been made in terms of a simple two-state potential energy curve model. A discussion of this model as it relates to the experimentally observable parameters in a chemi-electron spectrum will follow. Some consideration of its limitations will also be given.

Separation of electronic and nuclear motion within the Born-Oppenheimer approximation allows the collision to be described in terms of adiabatic potential energy surfaces (1). The ionisation process (2.1) occurs by a transition from the potential energy surface of the colliding neutrals to the product ion surface. The overall process may be written:

2.1 $$A + B \rightarrow AB^{+} + e^{-}$$

As the two neutrals collide they form a quasi-bound state which autoionises making a vertical, Franck-Condon-type transition from the initial surface $V_0(R)$ to the bound ionic surface $V_+(R)$, R being the internuclear separation (see figure 2.1), (2,3). The two neutral particles approach on a potential surface which may correlate with the ground state of AB, but in general to any state of AB, AB^* as can be seen in figure 2.1. The transition probability between the two surfaces, at a given internuclear separation, is given by the autoionisation width $\Gamma(R)$ (units of energy) which is related to the autoionisation life-time, $\tau(R)$, by the uncertainty relation, $\hbar = h/2\pi$, (2)

2.2 $$\Gamma(R) = \hbar/(\tau(R))$$

By analogy with Fermi's Golden Rule (4,5), $\Gamma(R)$ is given by,

2.3 $$\Gamma(R) = 2\pi\rho \, |\langle i|V|f\rangle|^2$$

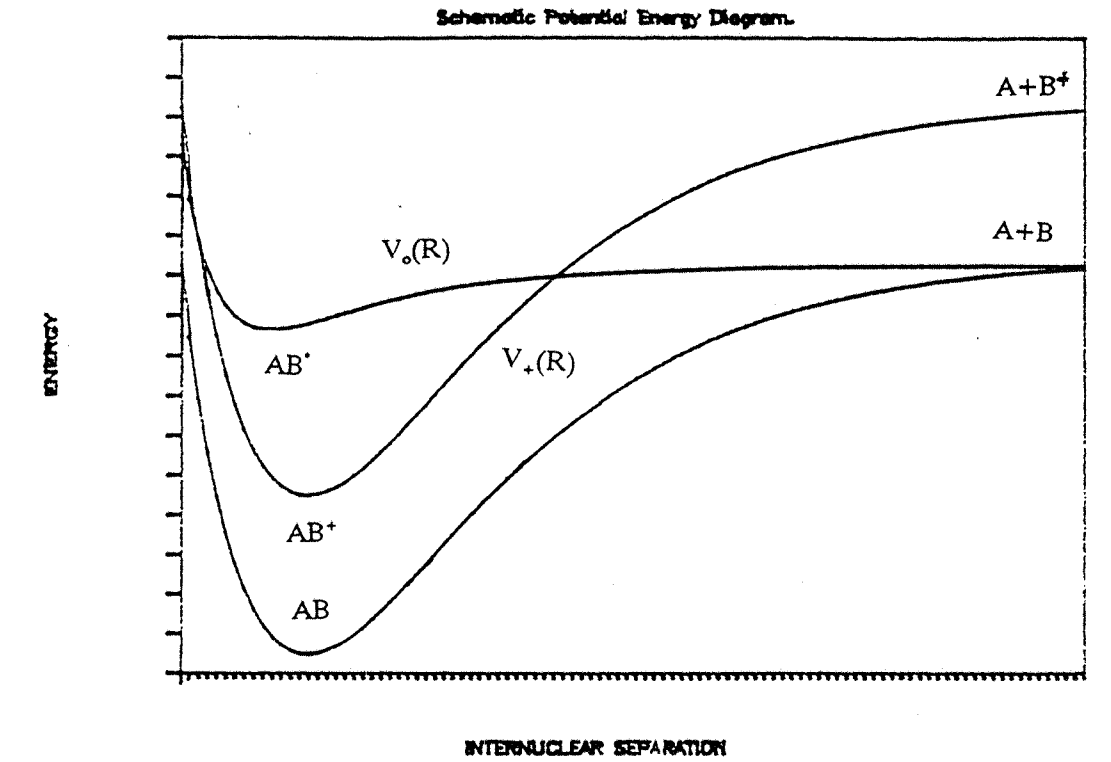

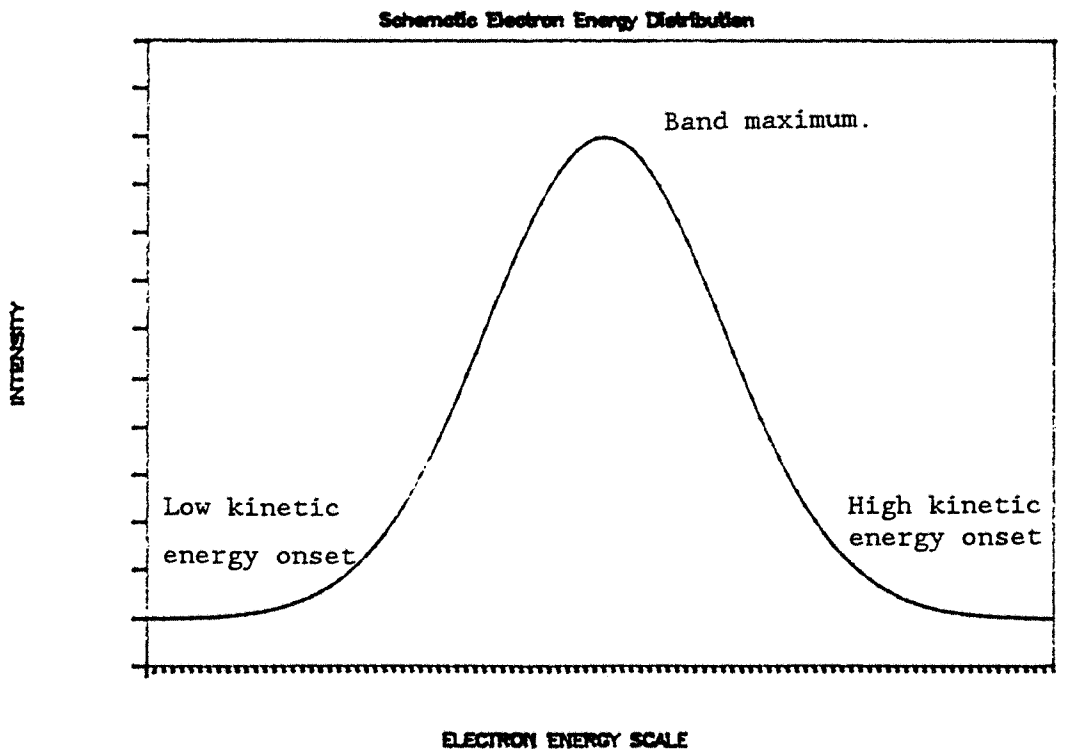

Figure 2.1 (a) Schematic potential energy curve diagram
(b) Schematic electron energy distribution

where $<i|$ is the initial state and $|f>$ is the final state, V is the interaction Hamiltonian and ρ is the density of states, the number of states per unit energy. The autoionisation width is thought to vary exponentially with R, decreasing with increasing R (7).

The transition between the two adiabatic potential surfaces results in the ejection of an electron of energy E_e which, for reactants in their ground states, is given by,

2.4 $$E_e = IE(AB) - D_0(AB) - \Delta E$$

where IE(AB) is the first ionisation energy of AB and $D_0(AB)$ is the dissociation energy of AB. ΔE is a term allowing for the relative translational energy in the initial and final channels, and the possibility of AB^+ being formed with internal energy (eg vibrationally or rotationally excited) (2). From a typical electron energy distribution, where transitions to individual vibrational states of the ion have not been resolved (shown in Figure 2.1), three parameters may be obtained: i) the low kinetic energy onset; ii) the most probable electron energy transition; and iii) the high kinetic energy onset. The latter may be equated with a lower limit of the reaction enthalpy in the approximation that $\Delta E \rightarrow 0$.

If the life-time of the quasi-bound autoionising state is long, the uncertainty in the energy is small, it may be possible to resolve ionisations to individual vibrational levels of the ion (subject to instrumental resolution) (4). However, the collision velocities of the two neutrals, both with assumed Boltzmann distributions, will contribute to the width of each vibrational component, and as a result a broad band envelope with no resolved vibrational structure may be observed.

The kinetic energy distribution of the ejected electrons from process 2.1 is dependent on the relative positions of the two adiabatic electron energy curves, their shapes and the probability of transition between the two surfaces $\Gamma(R)$ (equation 2.3) (2,5). In terms of this potential energy curve model, three limiting cases have been distinguished (6). The first is the crossing-point case, figure 2.2 a). In this case, the two potential curves cross each other at a moderately steep angle so that the overlap between the vibrational wavefunctions is only significant at the crossing point. This process is analogous to pre-dissociation and has been used to explain the observed dynamics of the reaction (8),

2.5 $$N + O \rightarrow NO^+ + e^-$$

The second case is the classical turning point case, figure 2.2 b). In this case the two particles approach on the upper surface reaching the minimum separation where the relative velocity of the two particles is nearly zero. This is the classical turning point. The most intense transition occurs vertically to the ionic potential surface from the classical turning point where the Franck-Condon factors are the largest. This mechanism has been invoked to explain the majority of observed chemi-electron spectra to date (9,10).

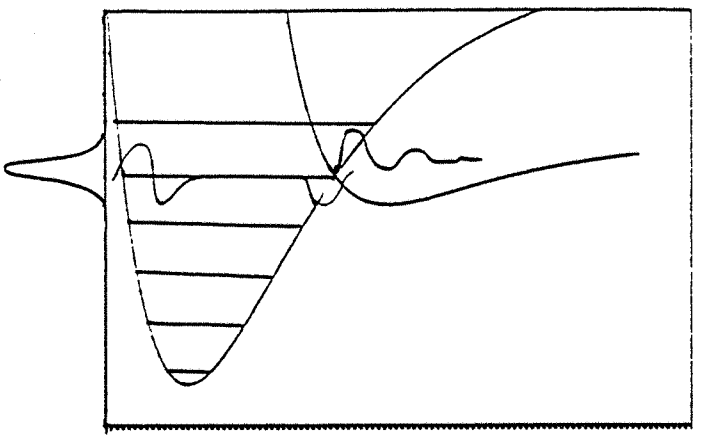

(a) Curve crossing case

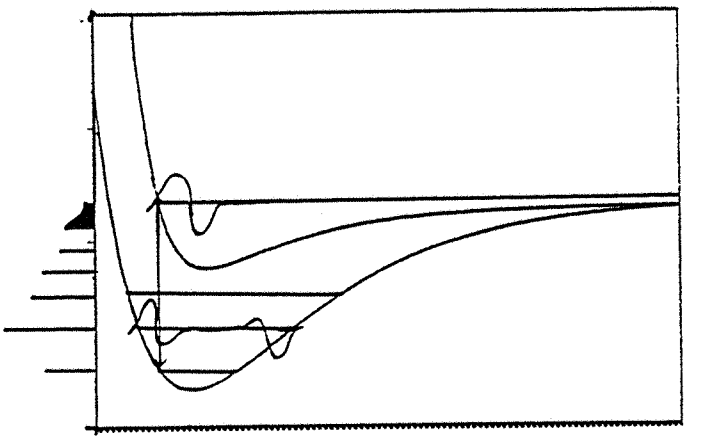

(b) Classical turning point case

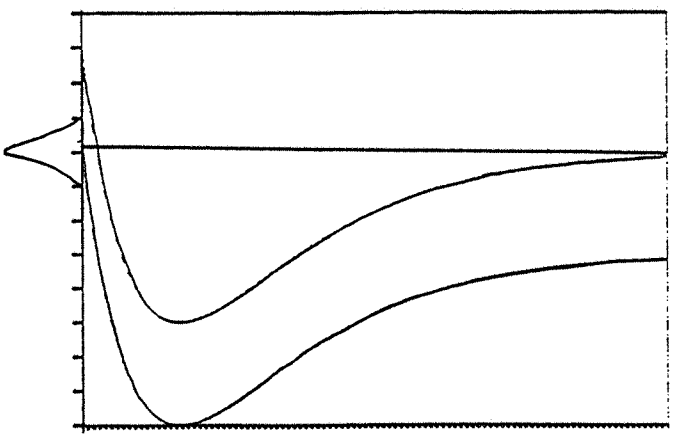

(c) Broad range case

Figure 2.2 The three limiting cases for the potential energy curve model:

(a) Curve crossing case,
(b) Classical turning point case,
(c) Broad range case.

The third case is the broad range case, figure 2.2 c). This occurs when the two curves are of similar shape and parallel over a large range of R. The electron transfer can occur over a broad range of internuclear separation giving a narrow electron energy distribution. The broad range case has been used to explain the associative ionisation of H(n=1) + H(n=3). Here the calculation of transition probability at a given internuclear separation is not valid (6), the probability accumulates over most of the width of the potential curve. This is an example of where a full quantum mechanical treatment is important.

For each of the limiting cases shown in Figure 2.2 schematic electron energy distributions are shown on the vertical axes, and are characteristic of each case.

Based on the simple potential energy curve model it is possible to calculate trajectories and hence cross-sections. The simplest theory is the classical approach of Miller (11). This theory shows the dependence of the cross-section on the relative collision velocity of the two particles and hence will show temperature dependence. Each of the three cases will have different temperature dependencies. For case one, the intersection of the two surfaces, and hence cross-section, is relatively independent of temperature, as only the Boltzmann distribution of velocities adds to the electron energy spectrum width. The resulting electrons will give a narrow band energy spectrum. Case two may give a broad energy spectrum with strong temperature dependence. With increasing relative collision velocities the time spent at the classical turning point decreases and the probability of transition and hence cross-section will be smaller. Thus the observed electron spectrum should become less intense with increasing temperature. For case three, the energy distribution is dependent on the spread of collision velocities, although the transition probability is relatively constant throughout the trajectory. Hence the electron energy distribution will have a slightly increased width with temperature although the intensity remains relatively constant.

The two-state potential energy curve model, when coupled with the computation of trajectories using classical (11), semi-classical (11,12) or quantum mechanical treatments (11,13,14), has been very useful in relating the important parameters $V_0(R)$, $V_+(R)$ and $\Gamma(R)$ to the physically observable quantities. Full scale quantum mechanical calculations are very difficult and have only been performed for the simplest systems (14,15).

The major assumption and limitation of the two-state potential energy curve model is that the incoming and outgoing local potential energy surfaces are assumed free from interaction with other surfaces (2). This is rarely true especially for systems containing heavy atoms when there may be many possible interacting potential energy surfaces. One of the more important interacting potential surfaces is the ionic surface corresponding to A^+-B^- (2). This is consistent with the classic 'ionic' bond in metal oxide or halogen systems. The transition to this surface is thought to be at long range and occurs via an electron jump 'harpoon' mechanism (16,17). An internuclear separation may be defined at which the interaction energy between the two particles equals the difference in the

ionisation energy of A and the electron affinity of B. From electrostatics the internuclear separation R_c is given by:

2.6 $$IP(A) - EA(B) = e^2 /(4\pi\epsilon_0 R_c)$$

where e is the elementary charge and ϵ_0 is the permittivity of free space (in SI units). For R_c in Å and ΔE = (IP(A)-EA(B)) in eV this becomes:

2.7 $$R_c = 14.40/(\Delta E)$$

This potential energy surface interaction is thought to be very important in the gas phase reactions of alkaline metals with halogen molecules (18,19).

Two other factors must be considered in a model of the chemi-ionisation process. Firstly, electronic selection rules control the transition from the initial state AB^* to the final state AB^+. The selection rules are thought to the same as those which apply to photoelectron spectroscopy - the main rule being only one-electron transitions between AB^* and AB^+ are allowed (20). Secondly, the symmetry of the excited state AB^* obtained from the states of A and B will be controlled by conservation of spin and orbital angular momenta along the potential energy surface.

The study of a chemi-ionisation process by chemi-electron spectroscopy, can contribute to its understanding, complementing the data from molecular beam, mass spectrometry studies. The experimental results obtained in this work are interpreted using the two state model and with some consideration of dynamic refinements.

References

(1) Z.Herman & V.Cermak. *Coll. Czech. Chem. Comm.* 31, 649, (1966).

(2) A.J.Yencha in *Gas-Phase Chemi-Luminescence and Chemi- Ionisation.* Ed.A.Fontijn. Elsevier Science, (1985).

(3) R.S.Berry. *Proc.Int.School.Phys. 'Enrico Fermi'.* 44, 193, (1968).

(4) T.Bregel, A.J.Yencha. *et al. Z.Phys D* 13, 51, (1989).

(5) W.H.Miller. *Chem.Phys.Lett.* 4, 627, (1970).

(6) S.E.Nielson & R.S.Berry in *Recent Developments in Mass Spectrometry,* Eds. K.Ogata & T.Hayakawa, Universtiy Park Press (1970)

(7) A.Niehaus. *Ber.Bunsenges.Phys.Chem.* 77, 32, (1973).

(8) J.N.Bardsley. *J.Phys.B.* 1, 349; 365, (1968).

(9) J.M.Dyke, A.M.Ellis, M.Feher & A.Morris. *Chem.Phys.Lett.* 145, 159, (1988).

(10) M.C.R.Cockett, J.M.Dyke, A.M.Ellis, M.Feher & T.G.Wright. *J.Elec.Spec.* 51, 529, (1990).

(11) W.H.Miller. *J.Chem.Phys.* 52, 3563, (1970).

(12) F.Koike & H.Nakamura. *J.Phys.Soc.Japan.* 33, 1426, (1972).

(13) W.H.Miller & H.F.Schaefer III . *J.Chem.Phys.* 53, 1421, (1970).

(14) H.Takagi & H.Nakamura. *J.Chem.Phys.* 88, 4552, (1988).

(15) R.S.Berry. *Adv.Mass.Spec.* 6, 1, (1974).

(16) M.S.Child. *Molecular Collision Theory.* Acedemic Press, London (1974).

(17) M.Menzinger in *Gas-Phase Chemi-Luminescence and Chemi- Ionisation.* Ed.A.Fontijn. Elsevier Science, (1985).

(18) A.Kowalski & M.Menzinger. *J.Phys.Chem.* 94, 1899, (1990).

(19) A.P.M.Beade. *Adv.Chem.Phys.* 30, 463, (1975).

(20) J.H.D.Eland. *Photoelectron Spectroscopy.* Butterworths, (1984).

Chapter 3

Experimental Methods.

3.1 Introduction.

The relatively new technique of chemi-electron spectroscopy has been developed to study electrons produced by gas phase chemi-ionisation reactions. This was first achieved for the reaction $O(^3P)$ + C_2H_2, both reactants being gases at room temperature (1). To extend the field of study beyond volatile reactants to the chemi-ionisation processes of metal gas phase reactions required the generation of high temperatures to give sufficient metal vapour pressure for the reaction to be observed. The initial high temperature studies of chemi-ionisation reactions concentrated on the detection of the product positive ions by mass spectrometry (2). The majority of studies have been carried out under single collision molecular beam conditions (3,4,5). To extend chemi-electron studies to metal gas phase reactions required methods used in high temperature photoelectron spectroscopy (6,7). The study of samples in the gas phase by high temperature photoelectron spectroscopy requires successful generation of the sample whilst maintaining detection of the photoelectrons. The adoption of the vapour generation/signal retention techniques of photoelectron spectroscopy has allowed study of a number of gas phase metal oxidation reactions by chemi-electron spectroscopy (8,9,10) and will be further developed and extended in this work.

The first high temperature photoelectron spectroscopy measurements used resistive heating as the heating method (11,12). The sample is placed in a metal furnace around which heating wires are wound non-inductively thereby minimising interference from induced magnetic fields. However, heating currents of c.40 amperes are required to generate sufficiently high temperatures and in practice, the induced magnetic field problem limits investigations to 1500 K. Indirect electron bombardment of the sample is a further possibility for heating but this can give rise to a large low energy electron background flux. Nevertheless these practical problems have been solved by effective shielding of the ionisation chamber and the technique has been used in photoelectron spectroscopy studies up to 2000 K (13). A technique which does not suffer from extraneous magnetic fields or stray electrons is that of laser heating (14). In this method, a powerful laser is directed onto the sample and slowly tracked across its surface. In practice, the evaporation can be a little erratic but these problems have been solved. This heating technique has been combined with laser multiphoton ionisation studies to produce some of the best resolved high temperature spectra recorded to date (14).

The heating technique used in this work is that of radiofrequency (RF) induction heating (7). In principle, a sample loaded in a furnace is placed in an alternating magnetic field of radiofrequency (1 MHz) which induces a current in the conducting material of the furnace. The current then heats the furnace ohmically. This technique suffers from RF interference of the detection electronics but pulsing the RF allows heating and detection to occur in antiphase to each other on a 50 Hz cycle. This allows generation of temperatures in excess of 2200 K and photoelectron spectra of many metals and metal oxides have been successfully recorded (7,15).

At the commencement of this work modifications were made to an existing high temperature multidetector photoelectron spectrometer (7) to tailor its performance to the investigation of chemi-ionisation processes. Initially the multidetector system was replaced with an exit slit and channeltron, single detector system. The multidetector was replaced because it suffered from problems of spectrum distortion due to non-uniform detector response across the channel plate. Further, the spread of detected energies across the plate, the detection window, was dependent on the mean pass energy of the electrons through the hemispheres. Thus throughout the energy range the width of the window changed becoming smaller for lower mean electron energies. This lead to spectral distortion which was particularly pronounced for low energy electrons.

It was also proposed to modify the instrument to allow detection of both ions and electrons produced by a chemi-ionisation reaction, within the same experiment. Previously, ion and electron investigations had been performed in separate experiments, with the same experimental conditions reproduced as closely as possible (8,9,10). It is important to measure both ions and electrons from a reaction at the same time to correlate observed electron bands with specific ion signals. The ultimate aim will be to design an instrument capable of electron and ion measurements simultaneously from the same reaction. (cf. coincidence photoelectron-photoion spectroscopy (16)). The development of the dual ion-electron instrument was thought an important step towards this objective. To this end, modifications have been made to the furnace region to improve the stability of the effusive sample beam, and a 600 a.m.u. quadrupole mass spectrometer was incorporated. Further an ion lens system was designed to extract the ions produced by reaction into the quadrupole for mass analysis.

Full consideration of the modifications made to the spectrometer will now be given, including results obtained from experiments on the previously studied La + $O_2(X^3\Sigma_g^-)$ reaction carried out to demonstrate the capabilities of the instrument.

3.2 The Basic Spectrometer.

The spectrometer essentially consists of three differentially pumped chambers: the ionisation chamber, the analyser chamber and the mass spectrometer chamber, shown schematically in Figure 3.1. All chambers are readily accessible for cleaning. The analyser chamber is separated from the ionisation chamber by the entrance slits allowing relatively high pressures in the ionisation chamber, typically $2x10^{-5}$-10^{-3} torr, whilst maintaining a constant low pressure, $8x10^{-6}$ torr, in the analyser chamber. Each chamber is differentially pumped by a 700 l/s diffusion pumps, backed by a rotary pump. A differential pressure is also maintained between the ionisation chamber and the mass spectrometer chamber. This is achieved by a separate 300 l/s diffusion pump, backed by a rotary pump. There is a small orifice, about 1mm, in the mass spectrometer chamber which allows ions to pass from the ionisation chamber into the quadrupole for mass analysis. This allows the mass spectrometer to operate at $2x10^{-6}$ torr throughout the range of pressure in the ionisation chamber.

The instrument has a helium discharge lamp as a source of v.u.v. radiation. The d.c discharge produces a number of emission lines (17) the most intense of which is the HeIα emission from the

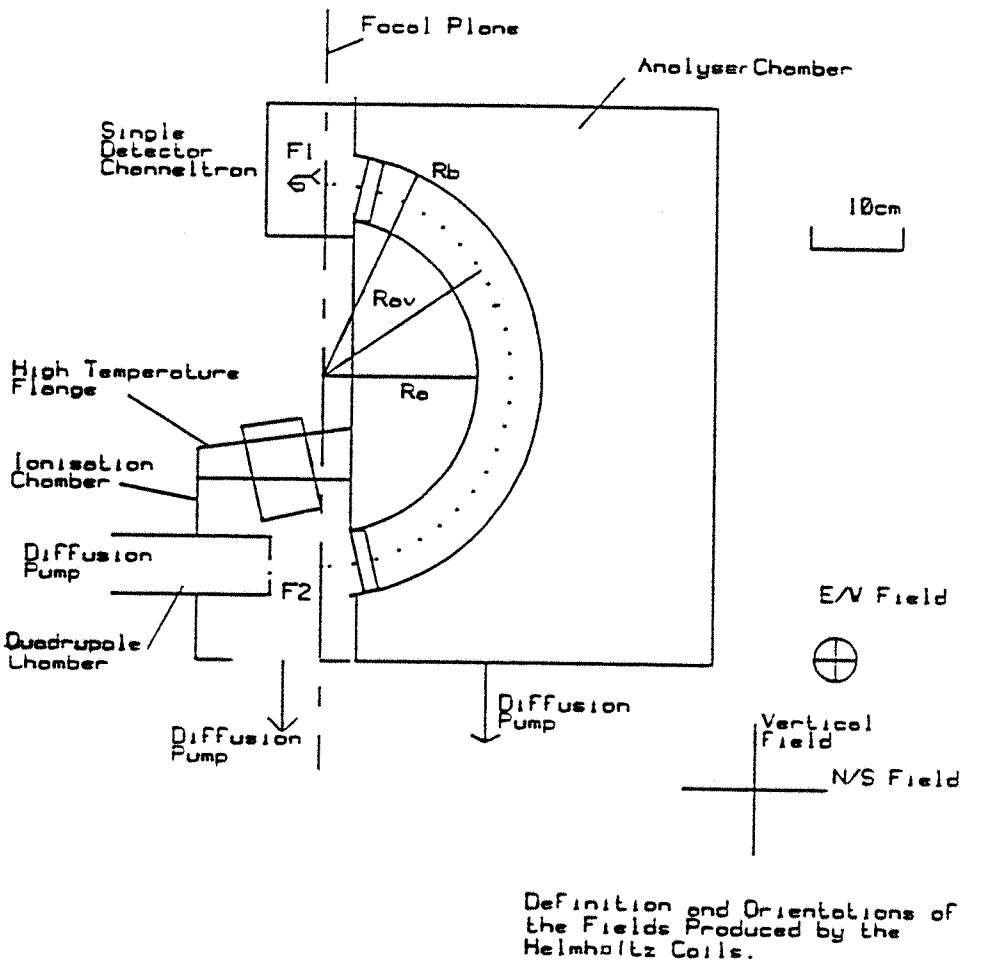

Figure 3.1 A schematic diagram of the basic spectrometer

$2^1P->1^1S$ transition producing photons of 21.219 eV. The lamp is differentially pumped to minimise the partial pressure of helium in the ionisation chamber and to reduce self reversal.

The sample vapour is generated by an inductively heated furnace and delivered as an effusive beam into the ionisation chamber. The sample then undergoes reaction, such as a metal oxidation reaction, which may produce chemi-electrons or may be photoionised to produce photoelectrons. The electrons are energy analysed by a 150° hemispherical electrostatic analyser in which electrons of different energies are separated by their trajectories in the electrostatic field of the concentric hemispheres - electrons of the correct energy passing through for detection by the channeltron placed at the exit focus. The small pulse created by the channeltron is amplified and pulse counted. The number of counts per second is plotted against the applied voltage to produce a spectrum. An internal energy calibration is added to the sample to produce electrons of known energy following photoionisation, enabling calibration of the energy scale. To ensure a uniform field within the ionisation chamber and analyser, all internal surfaces are coated with graphite by spraying with a fine colloidal suspension of graphite in isopropyl alcohol. The electrostatic analyser depends not only on the correct generation of the electric field for its operation but also on the effective annulment of any local magnetic fields. The Earth has an intrinsic magnetic field of about 600 milligauss and this needs to be annulled. For this purpose three sets of mutually perpendicular Helmholtz coils enclose the whole instrument (the directions of which are indicated in Figure 3.1). The current within these coils can be adjusted to optimise the performance of the instrument.

3.3 Sample Vapour Generation.

There are several factors to be considered in the generation of a high temperature vapour beam: 1) production of an effusive vapour beam that is stable over a reasonable length of time for experimentation; 2) protection of sensitive parts of the spectrometer, e.g. entrance slits, from radiative heating by the high temperature source; 3) collimation of the vapour beam to minimise chemical contamination within the ionisation chamber; 4) careful choice of materials which are resistant to high temperatures and chemically inert with respect to the sample. These factors prevent loss of electron signal by physical shielding and reducing stray electric fields produced by deposits of sample. With these design criteria in mind, a considerable modification to the high temperature flange has been undertaken (Figure 3.2).

The radiofrequency induction technique is based on the principle that a conductor carrying a current has associated with it a magnetic field. If the current is oscillating there is a change in the direction of the magnetic field on each cycle. This change in magnetic field flux induces a magnetic field change in any conductor/susceptor intersecting the flux. The change in magnetic field further induces a current in the susceptor. Usually these are small rapidly circulating currents known as eddy currents. Whilst the currents are present throughout the thickness of the conductor, most of the current density is at the surface. The depth, d, to which the current density falls to 1/e of its initial value (38%) is defined as the 'skin depth'. It is given by (18)

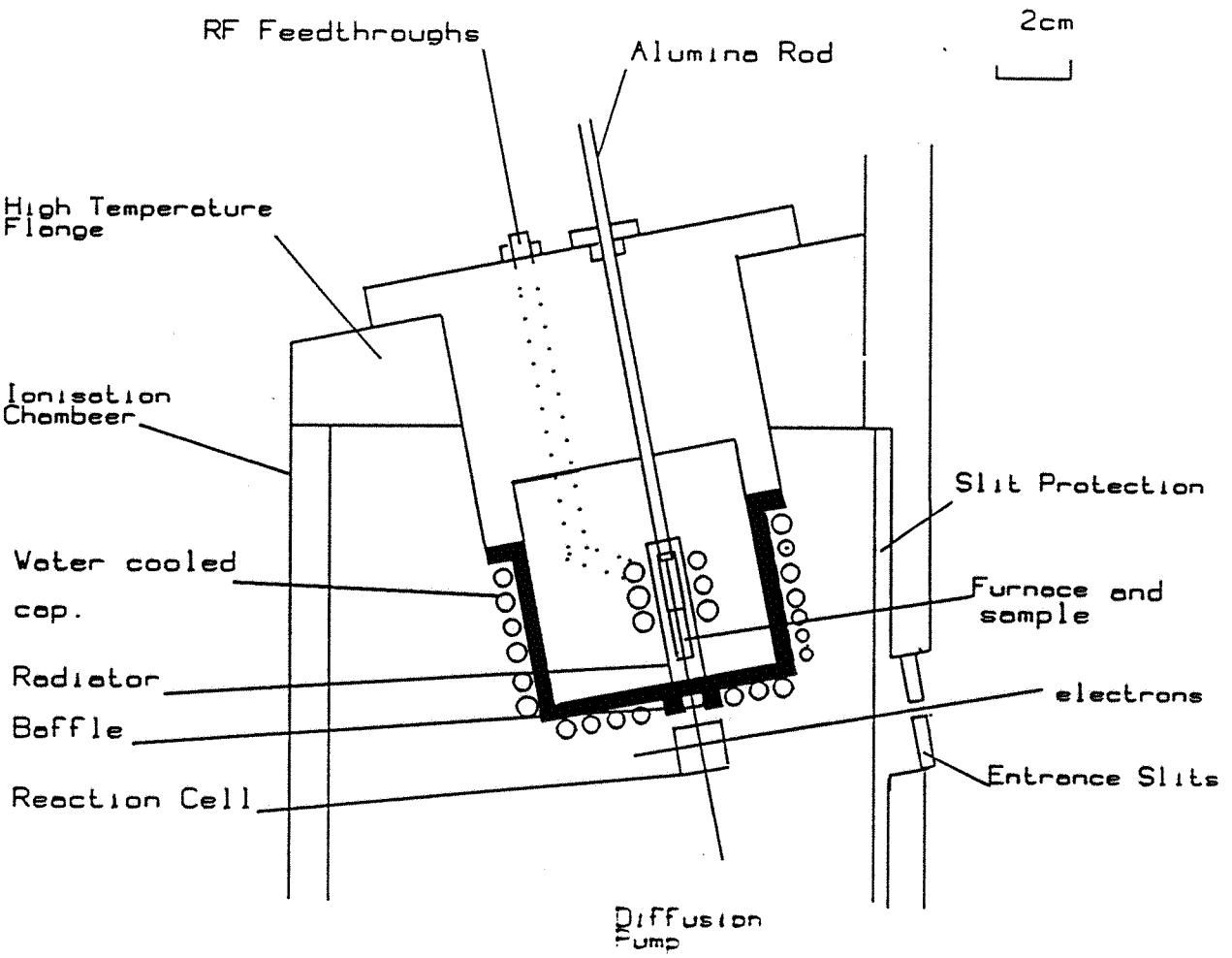

Figure 3.2 A section through the ionisation chamber showing the re-designed high temperature flange

3.1 $$d = 1/2\pi\ (\rho x10^9/\ \nu f)^{1/2}$$

where d is in cm, ρ the resistivity in ohm cm (at T in Kelvin), ν is the relative magnetic permeability of the conductor (at T in Kelvin) and f is the frequency of the RF, 1MHz in this work. In practice, the conductor is machined so that its thickness is close to the theoretical skin depth. (An extended discussion of the induction heating effect can be found elsewhere (18)). The induced eddy currents give rise to ohmic heating, where the power is given by:

3.2 $$\text{Power} = I^2R$$

where I is the induced current and R is the resistance. The conductor is chosen to maximise its heating with respect to its resistivity and skin depth. The efficiency of the heating by this method will depend on the exact geometry of the furnace arrangement; ideally this should be a 'tight coupling' configuration (18).

For the present spectrometer, the RF is generated at 1MHz external to the instrument and conveyed to the ionisation chamber by 1m long copper conduits. This passes the RF to the induction coil. The coil is made from copper tubing wound helically with approximately 7 isolated turns and is water cooled (Figure 3.2). The furnace is mounted on an alumina rod (to reduce losses by conduction) and suspended inside the induction coil in the region of maximum flux. Previous experiments with different furnace configurations have been tried in which only a cylindrical furnace was used (7). However the best arrangement, found by experiment, surrounds the furnace with a suitable material known as the susceptor or radiator. This is chosen with regard to its resistivity and permeability and is placed as close to the induction coil as possible thereby maximising the Rf flux cutting its surface. It is heated inductively and in turn, heats the furnace by radiation. The furnace, being a conductor, will also be heated directly by any stray RF, though this is thought to be a small contribution.

The major modification in this work provides a new solution of the joint heating and beam generation problem. The induction coil and furnace assembly have been placed within a water cooled cap. (Figure 3.2) The radiator is extended below the furnace such that an area between the base of the cap and the furnace is enclosed. This provides a heated region from which the effusive vapour beam is generated. Collimation of the beam is achieved by two physical structures. Firstly, at the base of the furnace a capillary is inserted and secondly at the base of the water cooled cap there is a baffle. The furnace-baffle combination produces a well collimated effusive beam which is directed at the reaction cell. This prevents sample deposition throughout the ionisation chamber which, through the production of stray electric fields, leads to electron signal degradation. Signal degradation due to sample deposition limits the useful experimental length of an evaporation. The water cooled cap also serves as a physical shield protecting the sensitive parts of the ionisation chamber from radiative heating. The entire assembly is mounted on the high temperature flange,

Figure 3.2, which is positioned on top of the ionisation chamber and aligned to target the effusive beam at the entrance focus of the analyser.

The material chosen for the radiator is tantalum. It satisfies all the requirements for a good susceptor/radiator and is easy to spot weld into the appropriate geometry. It has a skin depth of 0.5mm at an RF frequency of 1MHz. The choice of furnace material is made with regard to its refractory properties and it should be chemically inert with respect to the sample. Two frequently used materials are tungsten (m.p. 3500 K) and molybdenum (m.p. 2800 K). Molybdenum has the advantage in that it is more easily machined - tungsten has to be spark erroded. Both materials have been found to combine with samples at high temperatures forming tungstites, tungstates, molybdites and molybdates (19). The reaction of the furnace material with the sample is a constant concern and may give rise to vapour phase species which contribute to the sample beam. However, inclusion of the 600 a.m.u. quadrupole should allow direct determination of the vapour phase composition. This would provide direct confirmation of the reactants involved in a chemi-ionisation reaction.

The re-designed furnace arrangement, shown in Figure 3.2, has been found to work very well in practice allowing temperatures in excess of 2000 K to be routinely achieved with good signal retention, typically 70% of the initial signal intensity. The temperatures achieved have been calibrated with respect to the anode voltage of the RF generating circuit using a chromel/alumel thermocouple up to 2000 K. Temperatures above this are measured by focusing an optical pyrometer onto the hottest part of the furnace. Where the regions calibrated by the two techniques overlap, good agreement was found.

In practice the extended radiator and furnace arrangement within the water cooled cap provided an excellent, stable evaporation for the samples so far investigated. Before the re-design of the high temperature flange, an evaporation time of 30 mins during which measurements were possible was typically recorded from a furnace charged with a 0.5g sample . The extended radiator seems to provide a continuous hot region below the furnace, giving a useful, stable evaporation for periods of up to 4hrs from the same mass of sample. This was an important improvement in the development of the dual instrument, providing enough time during an experiment to carry out both electron and ion measurements.

3.4 Electron Spectroscopy.

Central to the measurement of chemi-electron spectra is the electron energy analyser. There are many types of analyser used in electron spectroscopy which can be broadly divided into two classes: i) retarding field analysers, and ii) deflection analysers (17). The analyser used throughout this work is the 150° hemispherical electrostatic deflection analyser. It consists of two concentric hemispheres, of mean radius 200 mm, as shown in Figure 3.1. The electrons are deflected by the field of the analyser generated by a negative potential -V on the outer hemisphere, with the inner having a voltage of equal and opposite sign, +V. For a given applied voltage V, electrons of initial energy E are detected at the exit focus. The relationship between E and V is (20,21)

3.4 $$V = E/2\ (R_b/R_a - R_a/R_b)$$

where R_b is the outer sphere radius and R_a the inner hemisphere radius, and V is the applied voltage, see Figure 3.1. For a fixed voltage on the hemispheres, there is more than one stable trajectory through the analyser for electrons of a given energy. The electrons are focused from the entrance to the exit focus - this is known as the 'double focusing' property and leads to enhanced instrument sensitivity (21). Equation 3.4 might suggest that the energy of an electron may be determined directly by measurement of the voltages applied to the hemispheres. However in practice, the presence of stray electric and magnetic fields may perturb the energy and an internal energy calibration standard is used.

A simple expression for the geometrical contribution to the instrumental resolution of the analyser can be obtained by considering the balance of forces acting on an electron for a trajectory leading to detection. The electron experiences an electrostatic force, directed towards the origin of the hemispheres, proportional to its charge and the electric field. This provides the centripetal force required to keep the electron moving in a circle, and is given by

3.4 $$eF = mv^2/r_{av}$$

where e is the charge on the electron, F the electric field, m the electron mass, v the velocity and r_{av} the mean radius. Rearrangement of this equation gives the kinetic energy $E = 1/2\ eFr_{av}$. It follows that the spread in energy ΔE at the base of the band is given by

3.5 $$\Delta E = 1/2\ eFdr_{av}$$

whence

3.6 $$\Delta E/E = dr_{av}/r_{av}$$

It can be seen the energy spread is dependent on the spread in the allowed trajectory radii. The entrance and exit slits provide a physical restriction on the allowed spread and dr_{av} can be approximated to the average slit width S/2, hence,

3.7 $$\Delta E/E = S/2r_{av}$$

Thus the geometric contribution to the instrumental resolution of the transmitted electrons depends on the average slit width and the radius of the trajectory. This is the main contribution to the experimental resolution of the spectrometer.

The resolution is routinely measured using the $Ar^+(^2P_{3/2})$<-$Ar(^1S)$ HeIα photoelectron peak width (FWHM) and is typically 30 meV (240 cm^{-1}) at ambient temperature and normal operating conditions. In this work, a loss of resolution with furnace temperature is observed; typically of 30 meV (240 cm^{-1}) measured at 298 K deteriorating to 60meV (480 cm^{-1}) at 2000 K . Hence it is possible to resolve vibrational structure for light diatomic and simple polyatomic molecules but in general, the technique must be regarded as one of low resolution.

A further property of the electrostatic analyser which is of importance to chemi-electron spectroscopy is the transmission function. This is also known as the luminosity and is a measure of the fraction of electrons produced of a given energy at the source which pass through the analyser for detection. This property is determined by the geometry of the analyser, the efficiency of the magnetic field annulment and removal of stray electric fields. For the hemispherical analyser the transmission function is linear for the electron energy in the region 2-9 eV but non-linear in the lower kinetic energy region < 2eV. Low energy electrons are the most likely products from a chemi-electron reaction and these are not well transmitted through the analyser. The transmission function of an analyser may be determined by measuring the photoelectron spectra of a number of small diatomic molecules whose relative band intensities have been established and are independent of the analyser used (22(a)). Comparison of band areas measured by a given analyser with the known band areas independent of the analyser allows the transmission function to be determined. Such a determination has been performed for the 150° hemispherical analyser of the type used in this work (22(b)), and confirms the non-linearity of the transmission function in the low energy region. Knowledge of the transmission function allows an experimental band shape to be corrected and relative band intensities determined. The effects of low energy transmission function distortion of electron bands can also be removed by pre-acceleration of the electrons before entering the analyser. This is the chosen course of action in this work.

The use of pre-acceleration exploits the geometry advantage of a 150° hemispherical analyser over a 180° analyser. The geometry of the analyser defines two foci, one at the entrance the other at the exit - they lie in a focal plane which contains the origin of the hemispheres (Figure 3.1). For a 180° analyser, the foci are at the mouth of the hemispheres and not easily accessible. With 15° removed from each end of the hemisphere the focal plane remains the same but the foci are liberated. It is then possible to arrange for electron production and detection to occur at a focus and to incorporate entrance and exit slits. A simple housing was designed to mount the single detector channeltron at the exit focus. A reaction cell was also designed to surround the entrance focus allowing a small voltage to be applied for pre-acceleration.

The reaction cell offers a number of advantages. The oxidant can be introduced through the reaction cell providing a region of increased reagent concentration, approximately an order of magnitude larger than that measured by the ionisation gauge positioned on the wall of the ionisation chamber. The increased concentration of oxidants leads to greater electron/ion yield produced from either photoionisation or chemi-ionisation. All electrons diffusing from the reaction

cell are accelerated by a few volts (typically 1.7 V) towards the entrance slits of the analyser - the two effects combined greatly enhance the signal intensity.

The pre-acceleration voltage is chosen by measurement of the photoelectron spectrum of $O_2(X^3\Sigma^-_g)$ with HeIα radiation. This produces five bands. The pre-acceleration is optimised such that all five bands of the $O_2(X^3\Sigma^-_g)$ photoelectron spectrum are visible and of acceptable relative intensity (23). The absolute energy of the detected electrons is always greater than 2 eV thereby ensuring the electron energy is in the linear transmission function region.

The procedure for recording a chemi-electron spectrum is straightforward. The oxidant gas is introduced into the reaction cell with the metal beam targeted at the analyser focus, Figure 3.2. The reaction occurs primarily within this region producing electrons in a uniform potential. The reaction however is not completely localised to the reaction cell and will occur throughout the ionisation chamber. The electrons, diffusing from the reaction cell only, are pre-accelerated and energy analysed. The chemi-electron band so produced is calibrated against the HeIα photoelectron spectrum of the oxidant, usually oxygen. For example, the first three vibronic components of the fifth band of oxygen are recorded after which the lamp power supply is turned off. A continued, constant sweep of the voltage on the hemispheres allows a linear extrapolation of the energy scale from the oxygen band components to the chemi-electron band for calibration. The lamp is switched off in preference to blocking the photon beam since this reduces the number of background electrons to zero, giving a enhanced signal to noise ratio. There are errors associated with this method of calibration primarily due to the slight non-linearity of the energy scale. In practice, a number of calibration points (typically 10) are made giving a mean value for the band maximum, quoting the standard deviation as the error. A photoelectron band is chosen for calibration as near to the observed chemi-electron band as possible to minimise the extrapolation error.

3.5 Ion Spectrometry.

To detect the positive ion products of a chemi-ionisation reaction a 0 - 600 a.m.u. quadrupole mass spectrometer has been fitted to the existing electron spectrometer. The chosen quadrupole was a SXP600, from V.G.Quadrupoles. The mass range of this quadrupole allows detection of ions containing heavy metals eg. lanthanides, and also possible contaminants from furnace materials (19). The mass spectrometer was used in this work in a non-standard mode of operation exploiting its sensitivity rather than its mass resolution. The ions from the reaction are produced externally to the quadrupole and are extracted into the spectrometer. This contrasts with its normal mode of operation where ions are produced within the source region by electron impact.

The quadrupole mass filter uses inhomogeneous oscillating electric fields to analyse ions according to their mass to charge ratio, m/e (24). The quadrupole field is generated by applying an alternating voltage $V\cos(\omega t)$ (V is the amplitude, ω is the frequency) with a direct voltage, U, to the quadrupole rods (of circular cross-section) arranged as shown in Figure 3.3. The motion of the ions in the x,y

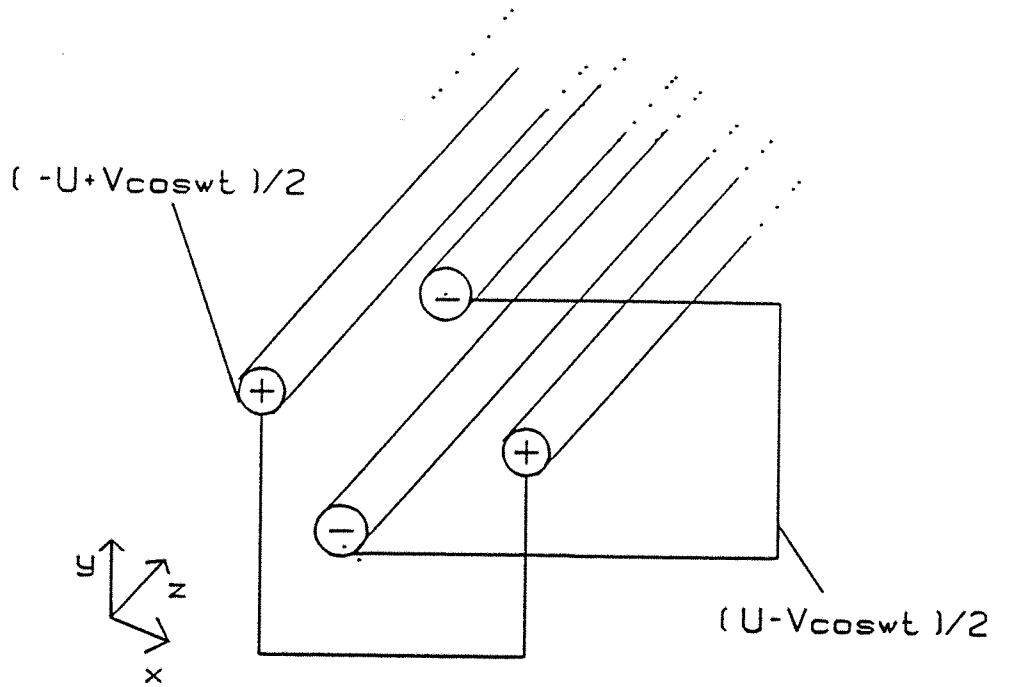

Figure 3.3 A schematic diagram of the quadrupole analyser arrangement

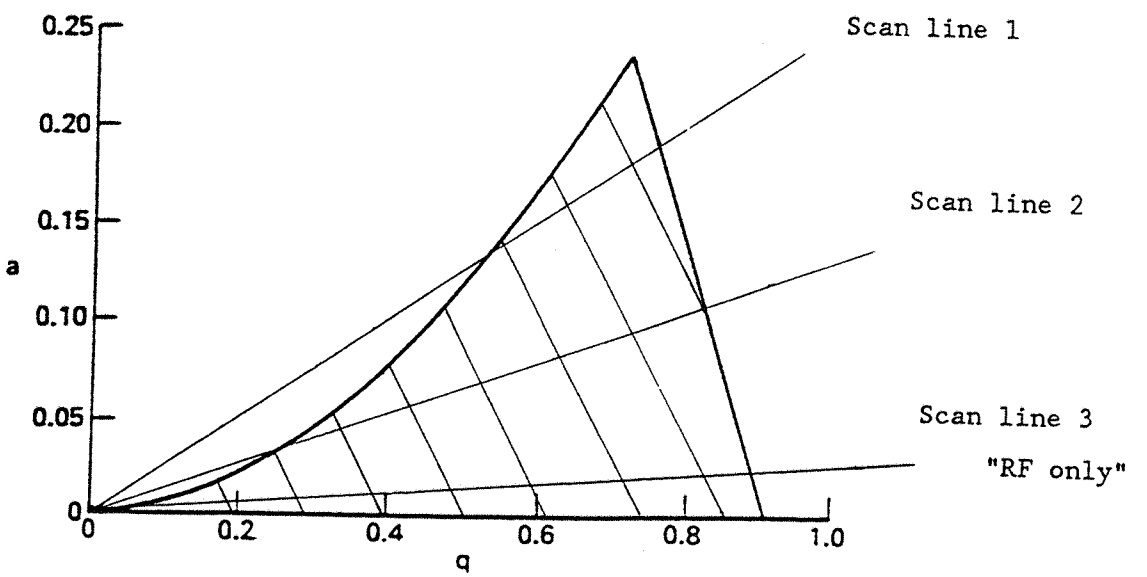

Figure 3.4 A stability diagram for the ion trajectories in a,q space
Scan lines for different resolutions are shown (see text)

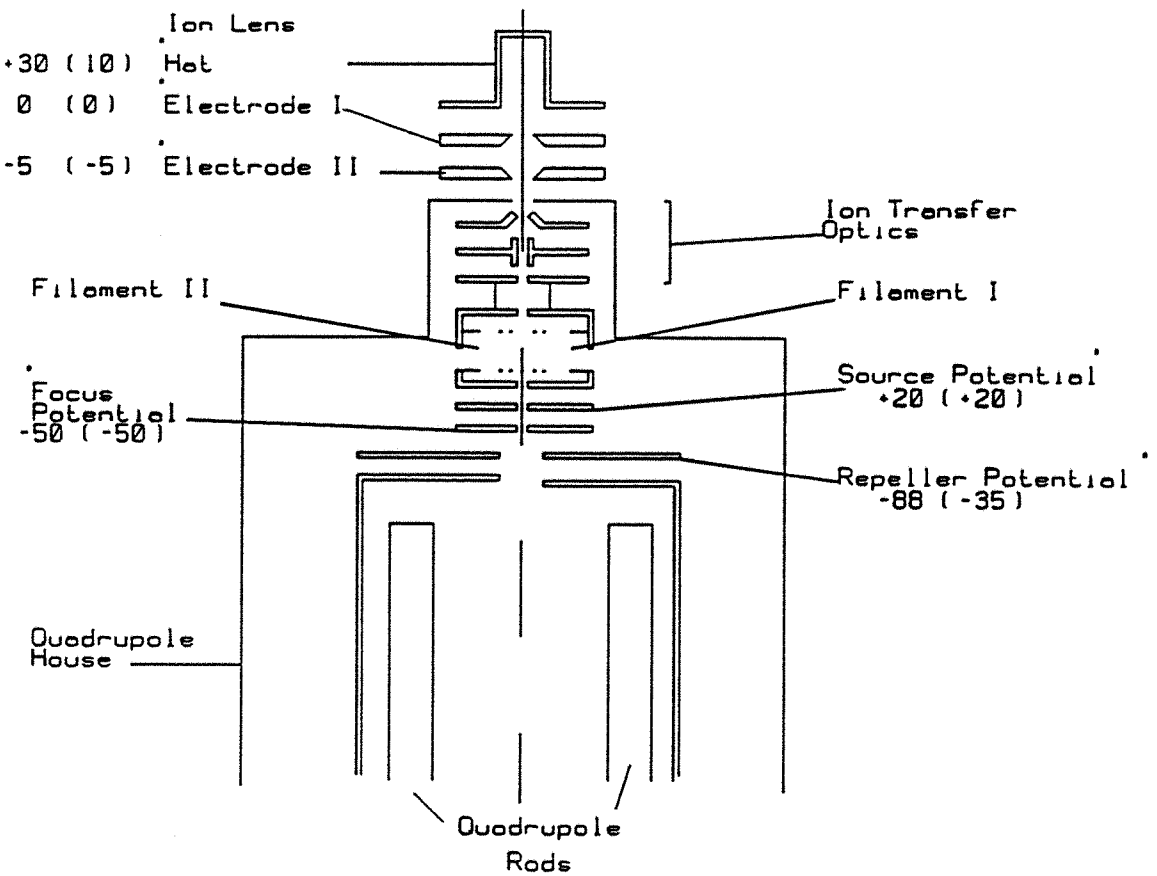

Figure 3.5 A schematic diagram of the ion lens and quadrupole optics

direction (axes defined in Figure 3.3) depends on the variation of the field in time. The velocity along the z-axis is maintained at a constant, optimised value. Thus an ion of given mass/charge ratio (m/e) will be transmitted for a given field variation and pass on for detection at the channeltron. The variation of U and V define a stability diagram for the x,y trajectories. The equations are of a form known as the Mathieu equations (24,25) and are usually expressed in terms of two parameters a, q, defined by:

3.8 $$q = 2eV/m\omega^2 r_0^2 , \qquad a = 4eU/m\omega^2 r_0^2$$

where r_0 is the quadrupole field radius (see figure 3.3). Stable trajectories for a given mass range form a region in (a,q) space shown schematically (shaded) in Figure 3.4. The ratio of a/q and hence U/V, given by the slope of the scan lines in Figure 3.4, determines the width of masses ΔM for which the trajectories are stable. If high mass resolution is required scan line 1 is used. To trade resolution for sensitivity scan line 2 is used allowing more ions to pass with poorer resolution. If scan line 3 is used nearly all trajectories are stable - this is 'RF only' mode and gives a measure of the total ion current. A mass spectrum scanned over a range of masses is obtained by varying the magnitude of the alternating voltage V and the direct voltage U but the ratio a/q is kept constant. A further possibility for generating a mass spectrum is to vary the frequency ω, but this is not used in practice (25). Unfortunately, the sensitivity of the quadrupole varies with mass (25) showing a discrimination to higher mass. This must be quantified if relative signal intensities are to be used as a measure of relative reaction cross-section (see below). A further factor affecting the peak width (resolution) given by (24),

3.9 $$\Delta M = (4x10^9/f^2 l^2) V_z$$

where, for ΔM in a.m.u., V_z is the axial velocity in eV, typically 3eV, f is the frequency in Hz and l is the length of the analyser in metres. In the normal mode of operation V_z is controlled by the potentials of the source region (see Figure 3.5) but ions produced externally can have a range of initial energies. If the initial ion energy is very large then the width ΔM also becomes large and the ions are transmitted without mass resolution. A parameter known as the pole bias (the reference voltage about which the quadrupole field is generated) can be adjusted to raise the potential of the entire quadrupole field to maintain the axial velocity at its optimum. This compensates for the spread in the initial external ion velocities.

The previous discussion suggests several important design criteria for an ion lens to extract externally produced ions into the quadrupole for mass analysis. An ion lens system has been designed with the following objectives: i) efficient extraction of ions from the reaction region; ii) extraction at the lowest possible energies to minimise ion molecule reactions; iii) production of a collimated beam of ions that can be directed into the quadrupole; and iv) the design of a pin-hole sampling system into the mass spectrometer chamber to allow the quadrupole to operate at the

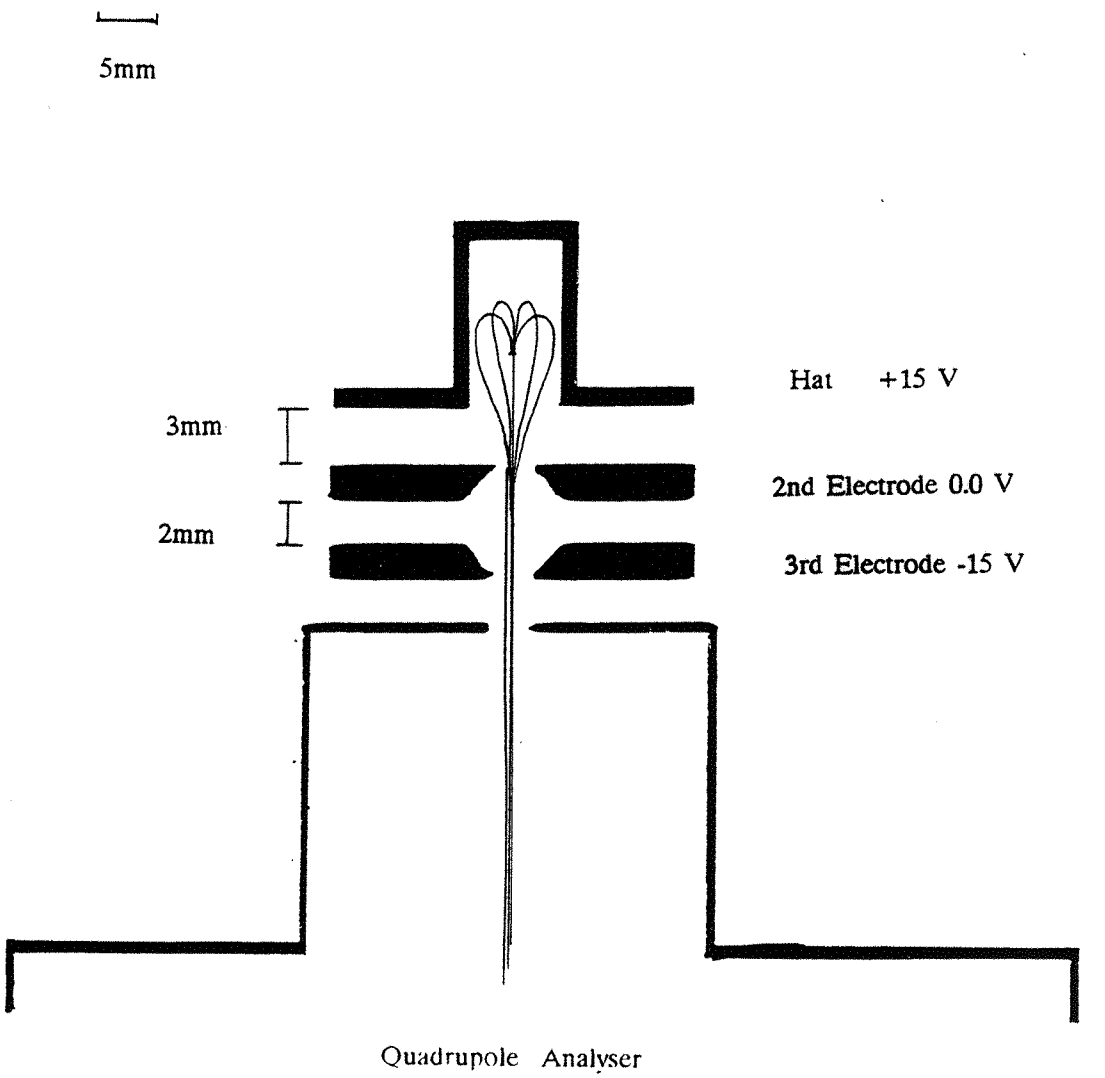

Figure 3.6. Simulated ion trajectories for the ion lens designed to extract ions into the quadrupole. The voltages shown are those optimised by simulation.

lowest possible pressure throughout the range of ionisation chamber pressures. The final design was optimised with respect to these criteria using a simulation program called SIMION (26,27). The design with some computed trajectories is shown if Figure 3.6 (see below for further discussion). The ion lens consists of three electrodes with independently variable voltages. The first component, 'the hat', is initially placed at +30V. This enables most ions to be extracted from the reaction region. Two further electrodes focus the ion beam and direct it towards the circular hole, initially 2mm, in the quadrupole housing. The hole size is chosen at the start of the experiment to limit exposure of the quadrupole to harmful oxidants, e.g. $O(^3P)$, which have been found to degrade the performance of the quadrupole rapidly.

Figure 3.6 shows the ion lens geometry optimised by computer simulation. The computed extraction efficiency depends strongly on the size of the holes in the two lower electrodes and the presence of two 'lugs' at the base of the hat which control the collimation. The trajectories are computed for positive ions of m/e 150 with initial energy 0.2 eV. This is somewhat more than the expected maximum energy but illustrates the collimation properties well. The reaction point is positioned 5 mm from the base of the hat and ions are allowed all possible initial directions. The collimation of the beam was optimised to eliminate collision with the electrodes and produce a beam to pass to the quadrupole optics. The agreement between the optimum extraction voltages, obtained by simulation, and the experimentally observed voltages is reasonable given the idealised representation of the ion lens in the simulation (27). The ion lens extraction optics and the quadrupole ion optics are shown in Figure 3.5. The ion lens voltages and the quadrupole source region voltages shown in Figure 3.5 (in brackets) are those determined experimentally for the La + O_2 reaction.

The quadrupole operation is initially optimised with respect to the electron impact mass spectrum of the residual gases in the vacuum system by adjustment of resolution and multiplier voltages to obtain an acceptable spectrum. The filament emission current is then reduced to zero to allow detection of chemi-ions. The extraction voltages are set at their initial values: hat is +30V, 0.0 V on the second component, -5V on the final electrode. These voltages are sufficient to produce secondary ions by collision: a full investigation of secondary ion production is postponed until the next section. Once an ion signal has been observed, the extraction voltages are minimised to maintain the primary ion signal and reduce the secondary ion current.

3.6 The Chemi-Electron Chemi-Ion Spectrometer.

The dual instrument combines electron spectroscopy and ion spectrometry for the study of ionic products of chemi-ionisation reactions. Both techniques are brought together in the ionisation chamber, shown schematically in Figure 3.7. The chamber contains two reaction regions. For electron spectroscopy, the oxidant is introduced into the reaction cell to react with the sample beam, thereby localising the reaction to this region. Once the electron signal is established, the reaction is switched from the reaction cell to the ion lens. The oxidant is supplied to the ion lens and removed from the reaction cell thus the reaction occurs primarily within the hat region. There is

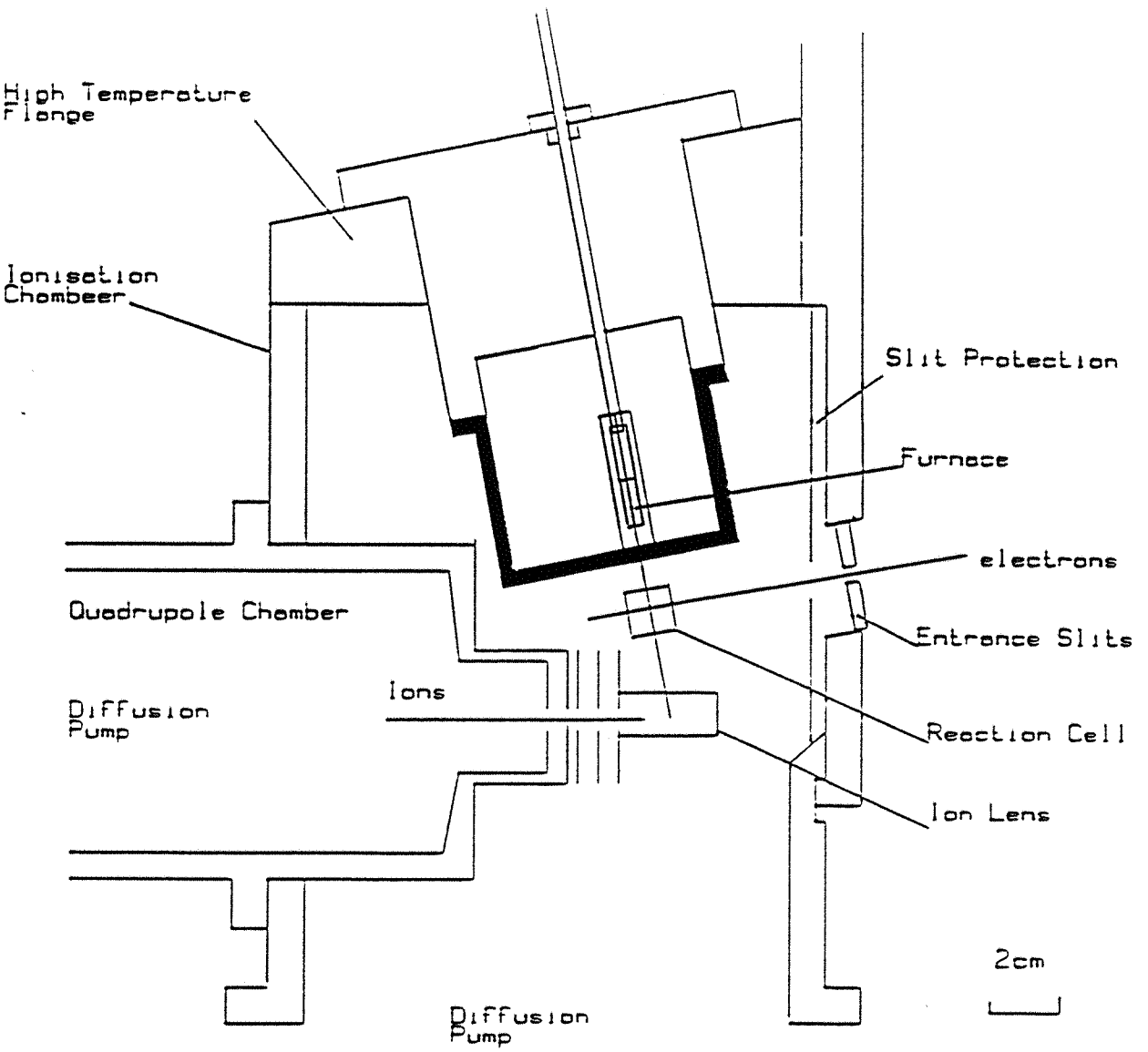

Figure 3.7 A section of the ionisation chamber of the chemi-electron, chemi-ion spectrometer

some interference between the extraction voltages of the ion lens and the electron signal, so in general the mass spectrometer is quiescent throughout the electron experiments. However, it is possible to detect ions produced in the reaction cell that diffuse down to the ion lens and in practice this is used to monitor the onset of a chemi-ionisation reaction.

The collimated metal beam passes through both reaction cell and ion lens producing a stable partial pressure of metal for study. The oxidant partial pressure cannot be measured directly within the reaction cell or ion lens but is estimated from the total pressure in the ionisation chamber measured by an ionisation gauge situated on the wall of the ionisation chamber. In practice, the partial pressures of oxidant within the ion lens or reaction cell will depend on the pumping efficiency from these regions. Also, because of the geometry used, the metal partial pressure in the ion lens will be lower than in the reaction region due to divergence of the effusive beam. Consequently, the ion/electron measurements are made under slightly different experimental conditions. This is one of the shortcomings of the instrument.

The shielding of the high temperature source from the rest of the ionisation chamber is extremely important given the close proximity of the quadrupole and other sensitive parts of the instrument. The water cooled cap works very efficiently allowing use of teflon supports for the reaction cell and teflon spacers for the ion lens.

To determine the performance of the chemi-electron, chemi-ion spectrometer an investigation of the previously studied La + $O_2(X^3\Sigma_g^-)$ reaction has been undertaken (30). A discussion of the results as the pertain to assessment of the performance of the dual instrument will be given. A full interpretation of the La + $O_2(X^3\Sigma_g^-)$ chemi-ionisation reaction may be found elsewhere (30).

The La + $O_2(X^3\Sigma_g^-)$ reaction as studied with the chemi-electron, chemi-ion spectrometer

The La + $O_2(X^3\Sigma_g^-)$ reaction has previously been studied in this laboratory by two separate experiments to determine the electron energy distribution and ions produced by the reaction (9). The chemi-electron and chemi-ion spectra obtained with the modified instrument are shown in Figures 3.8 and 3.9. The electron spectrum is somewhat more intense than previously recorded (by a factor of 5), and has a band maximum at 0.9 ± 0.1 eV, calibrated using the fourth photoelectron band of O_2. In the previous investigation (9), the band maximum is found to vary with temperature from 0.8 to 1.3 eV. This was observed as the temperature had to be continuously increased to maintain the signal intensity. The spectrum presented in Figure 3.8 was recorded reproducibly at the same temperature for a considerable length of time with no variation in position. The variation with temperature is a real effect (9) but was not investigated further here. The electron spectrometer, with new reaction cell, single detector channeltron and channeltron housing produces spectra consistent with those previously observed with enhanced sensitivity and reproducibility. The useful experimental time for which spectra can be recorded, has been increased by a factor of eight. The chemi-ion spectrum, shown in Figure 3.9, has two metal ion peaks assigned as LaO^+ and LaO_2^+ and two further ion peaks of small mass to charge ratio. To determine whether the ions observed are primary ion products of the reaction or products of ion-molecule reactions occurring

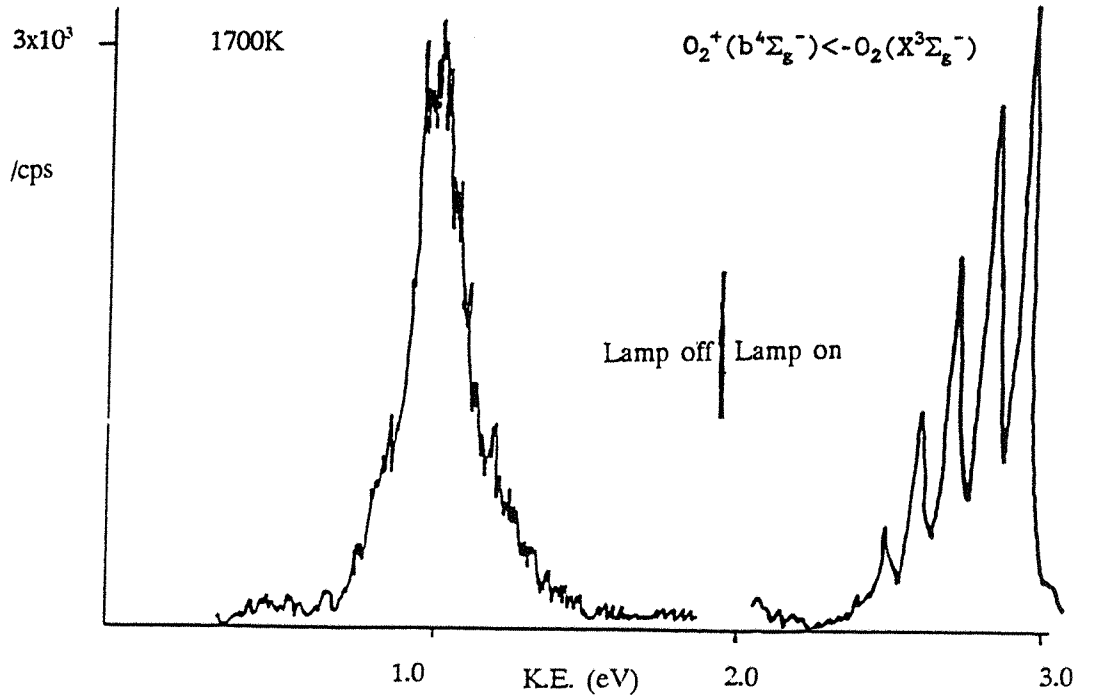

Figure 3.8 The electron spectrum recorded for the reaction La + $O_2(X^3\Sigma_g^-)$

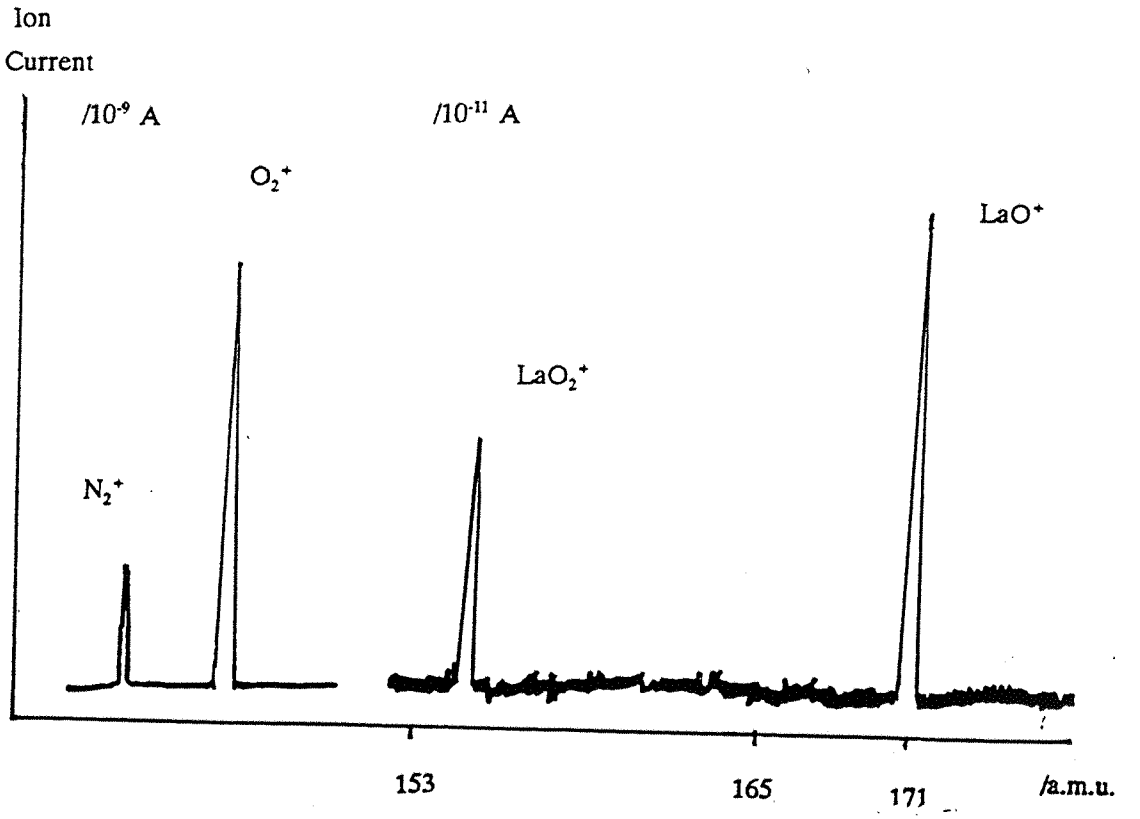

Figure 3.9 The chemi-ion spectrum recorded for the reaction
La + $O_2(X^3\Sigma_g^-)$

during extraction, an investigation of the dependence of ion intensities on extraction voltages was undertaken. The ions of m/e 28 and 32 were assigned as N_2^+ and O_2^+ respectively. These are the first ions detected at the start of an evaporation before electron or metal ion signals were observed. Their formation is attributed to the following process

3.10 $$P^+(30eV\ trans) + O_2 \rightarrow P^+ + O_2^+ + e^-$$

However an alternative reaction is possible

3.11 $$P^+(30eV\ trans) + O_2 \rightarrow P + O_2^+$$

where P^+ is a primary ion in each process produced by chemical reaction and with translational energy determined by the extraction voltages. The enthalpy for the reaction 3.10 is the first ionisation energy of O_2. Thus O_2^+ will not be observed when the extraction voltage and hence translational energy of P^+ falls below 12 V. This is contrasted with process 3.11 where the reaction enthalpy is given by $IE(O_2)$ - IE(P), the difference in the ionisation energies of the two species. For this reaction, variation of the extraction voltages will show an ion current present below 12 V. The results are presented in Figure 3.10. Extrapolation of the lines back to the horizontal axis suggests N_2^+ and O_2^+ are formed by reaction 3.10. The intercepts give a crude estimate of the first ionisation energies of N_2 and O_2: 13.6 eV for O_2 (cf 12.06 eV) and 16.9 eV for N_2 (cf 15.58 eV) (28). The secondary ion peaks are very intense, typically two orders of magnitude greater than the primary ion intensities. This 'internal amplification' further explains why secondary ion peaks are observed at lower furnace temperatures (hence lower metal partial pressures) before primary metal ions or electrons are detected.

The ion spectrum, Figure 3.9, shows two signals attributed to the metal containing ions LaO^+ and LaO_2^+. No ions of higher mass containing potential furnace materials were observed. The primary ion currents were measured with minimum extraction voltages to reduce ion-molecule reactions. Similar experiments showing variation of extraction voltages with ion current intensity suggest the ions are formed from primary chemical reactions, the relative intensities not changing over a range of voltages. The results are presented in Figure 3.10. However, absolute intensities vary as the extraction efficiency varies with voltage and the two intensities fall to zero when the voltages fall below about 6 V corresponding to poor ion extraction. The ion signals observed are attributed to the following reactions

3.12 $$La + O_2 \rightarrow LaO_2^+ + e^-$$

3.13 $$La + O_2 \rightarrow LaO + O$$

$$La + O \rightarrow LaO^+ + e^-$$

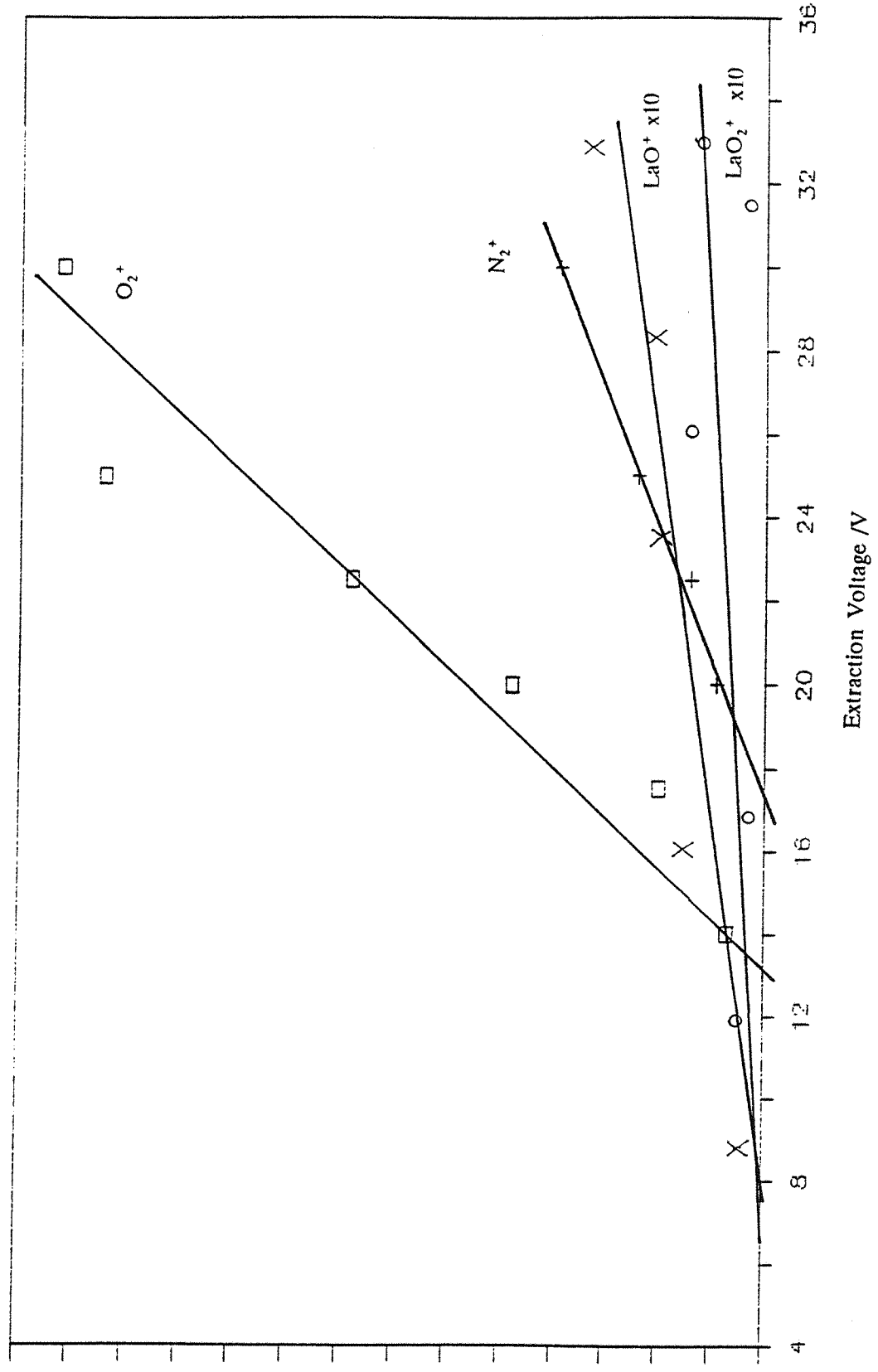

Figure 3.10 Variation of ion intensity with extraction voltages for the signals O_2^+, N_2^+, LaO^+ and LaO_2^+

This assignment is based on kinetic modelling of the effusive beam conditions and is fully discussed elsewhere (9). The relative ion intensities are in good agreement with those predicted from the kinetic model and observed experimentally (9), showing a strong dependence on the partial pressure of oxygen.

The relative intensities of ions produced by the two reaction pathways give a measure of the relative rates of the processes leading to their production. With knowledge of relative reagent concentrations it may be possible to estimate relative reaction cross-sections. This has been successfully carried out for the reaction Ce + $O_2(X^3\Sigma_g^-)$ (9). However, before measured relative ion intensities can be used in calculations of this type some correction for the mass discrimination of the quadrupole must be made. The sensitivity of the quadrupole is known to vary with mass (25), being reduced for higher masses. It is thought that heavier ions move more slowly through the fringe fields of the quadrupole than the lower mass ions and consequently the trajectories are more easily perturbed. Further, with a slower axial velocity equation 3.9 suggests the peak width will be smaller with consequently higher resolution. Thus ions of different masses are measured with inherently different resolutions providing an instrumental contribution to the relative ion intensities.

A measure of the mass discrimination was obtained by comparing the intensities of fragment ions from a mass calibration standard, produced by electron impact as measured on both the SXP600 quadrupole and a magnetic sector mass spectrometer. The fragmentation pattern for heptacosafluorotributylamine (PFTBA) generated by electron impact of electron energy 70 eV, spans the mass range 0 - 600 a.m.u.. The magnetic sector spectrometer is thought not to discriminate against mass and so a measure of the quadrupole discrimination can be obtained by plotting the ratio of ion intensities $I_m(quad)/I_m(mag)$, against mass (Figure 3.11). The ratio $I_m(quad)/I_m(mag)$, shows considerable variation over the mass range. For masses 0 - 300 a.m.u. the ratio $I_m(quad)/I_m(mag)$ varies by an order of magnitude and for masses greater than 300 a.m.u. $I_m(quad)/I_m(mag)$ it is an order of magnitude smaller again. This may be exaggerated due to variation in sample concentration during the acquisition of the spectrum. The result is however broadly in agreement with the discrimination observed elsewhere (25).

The ratio $I_m(quad)/I_m(mag)$ is a measure of the mass discrimination but it would be unwise to use it as a correction factor for relative intensities. The mass discrimination of the magnetic sector is not quantified since it includes both detector efficiencies as well as other instrumental errors all of which contribute to the instrument's response and thus Figure 3.11 may not be regarded as a calibration curve. Further, data on the fragmentation pattern of the mass calibration standard varies with the magnetic sector instrument chosen. The data for Figure 3.11 was obtained from a V.G.70 S.E. magnetic sector instrument but this may be compared with data for the same compound derived from an A.E.I. MS9 magnetic sector instrument (29) where considerable differences are observed. Figure 3.11 does however demonstrate the possible errors involved in making relative ion intensity comparisons especially when the ions are of very different masses. For ions that do not have significantly different masses, within 20 a.m.u., it is reasonable to assume the mass discrimination

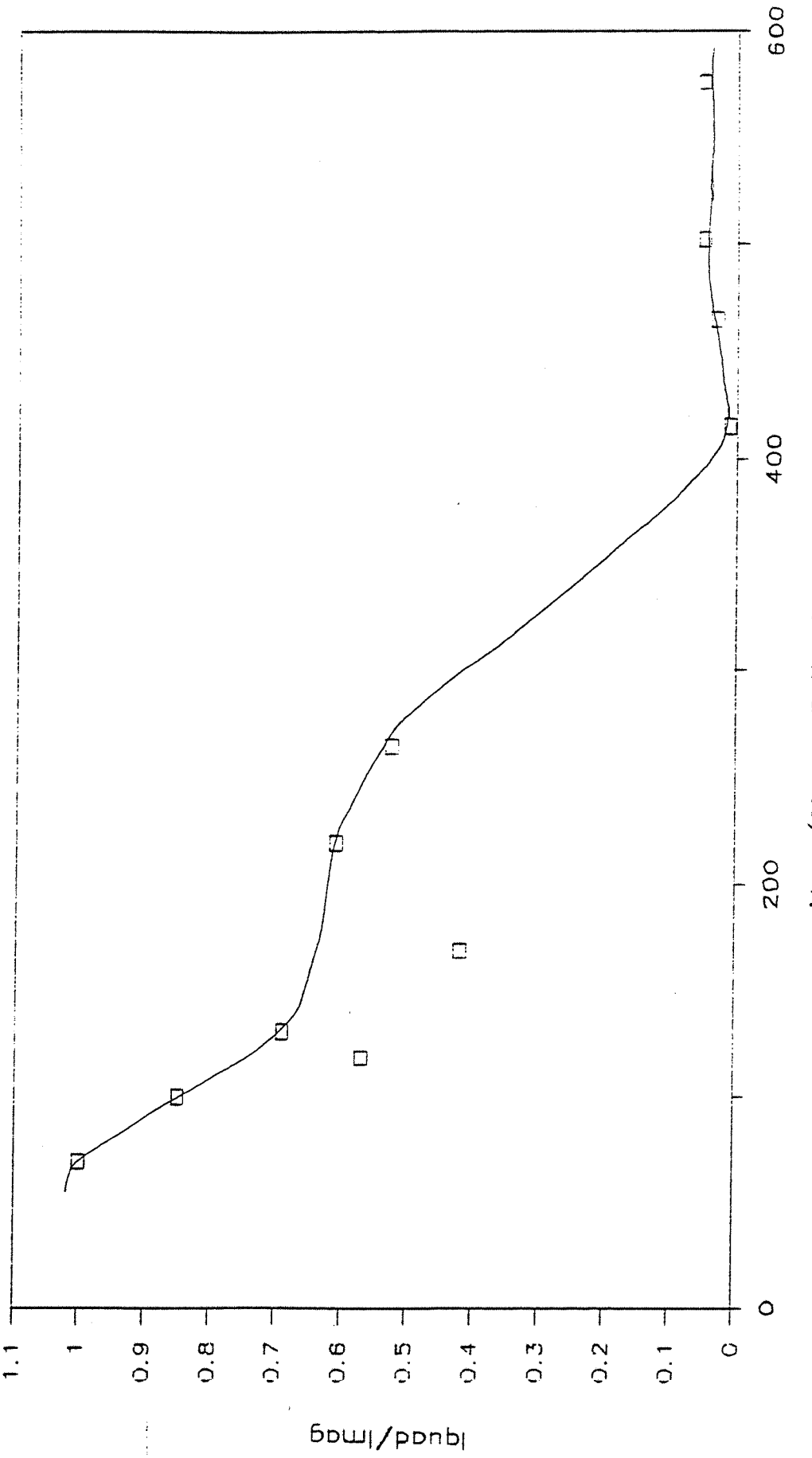

Figure 3.11 Variation of the ratio I_{quad}/I_{mag} for the spectrum of PFTBA for the V.G.SXP600 Quadrupole and the V.G.70 S.E. Magnetic Sector

is not significant. This approach will be adopted here, following a precedent set elsewhere (31).

The investigation of mass discrimination suggests a protocol for operation of the quadrupole. The variation of resolution with mass suggests that to maintain sensitivity at higher masses, the resolution of the low mass region of the spectrum obtained by electron impact of the residual gases should be reduced. This is done by varying the slope of the scan line (Figure 3.4) controlled by a potentiometer on the control panel. Once ions of higher mass are detected, mass resolution may be adjusted as required.

In conclusion, the La + O_2 investigation has shown that the dual chemi-electron, chem-ion spectrometer is capable of reproducing with good accuracy the results previously obtained. Further, the modified vapour generation system allows experiments to be performed for a period of four hours during which spectra may be recorded. The chemi-electron, chemi-ion spectrometer draws the most important conclusion that the observed kinetic energy distribution of the ejected electrons from the La + O_2 reaction, is a superposition of the energy distributions of the electrons emitted from both competing processes responsible for primary ion production. The investigation has tested the modifications made to the spectrometer and has suggested refinements to its operating technique.

References

(1) N.B.H.Jonathan, A.Morris, M.Okuda & D.J.Smith.
J.Chem.Phys. 53,3046,(1971).

(2) Z.Herman & V.Cermak. *Coll.Czech.Chem.Comm.* 31,649,(1966).

(3) H-j. Meyer, Th.Schulze & U.Ross. *Chem.Phys.* 90,185,(1984).

(4) S.Wexler. *Ber.Bunsen.Ges.Chem.* 77,606,(1984).

(5) C.E.Young, R.B.Cohen, P.M.Dehmer, L.G.Pobo & S.Wexler.
J.Chem.Phys. 65,2562,(1976).

(6) J.Berkowitz in *Electron Spectroscopy: Theory, Techniques and and Applications.* Eds. C.R.Brundle & A.D.Baker.

(7) A.Morris, J.M.Dyke, G.D.Josland, M.P.Hastings & P.D.Francis.
High Temperature Science. 22,95,(1985).

(8) J.M.Dyke, M.Feher, B.Gravenor, & A.Morris. *J.Chem.Phys.* 91,4876,(1987).

(9) M.C.R.Cockett, J.M.Dyke, A.M.Ellis, M.Feher, A.Morris.
J.Am.Chem.Soc. 111,5994,(1989).

(10) J.M.Dyke. *J.Chem.Soc.Faraday.Trans.II.* 83,69,(1987).

(11) S.T.Lee, S.Suzer, E.Mathias, R.A.Rosenburg & D.A.Shirley.
J.Chem.Phys. 63,3473,(1975).

(12) E.P.F.Lee, A.W.Potts & J.E.Bloor. *Proc.Roy.Soc.* A382,373,(1982).

(13) T.Prescher, M.Richter, B.Sonntag, & H.E.Wetzel.
Nucl.Inst.Meth.Phys.Res. A254,627,(1987).

(14) L.Sanders, A.Sappey, & J.C.Weishaar. *J.Chem.Phys.* 105,6952,(1986).

(15) D.Bulgin, J.M.Dyke. *et al. J.Elec.Spec.* 12,67,(1977).

(16) (a) J.H.D.Eland *Int.J.Mass.Spec.* 8,143,(1972)
(b) W.Habenicht, K.M-Dethlefs & E.W.Schlag. *J.Elec.Spec.* 52,697,(1990).

(17) J.H.D.Eland. *Photoelectron Spectroscopy.* Second Edition,
Butterworths, (1984).

(18) E.J.Davies & P.G.Simpson *Induction Heating Handbook.*
McGraw-Hill, Maidenhead, (1979).

(19) G.Verhagen, R.Colin, G.Exstein & J.Drowart.
Trans. Faraday. Soc. 61,1372,(1965).

(20) E.M.Purcell. *Phys.Rev.* 54,818,(1938).

(21) E.D.Sevier. *Low-Energy Electron Spectroscopy.* Wiley Interscience,(1972).

(22) (a) J.L.Gardner, & J.A.R.Samson. *J.Elec.Spec.* 8,469,(1970).
(b) T.N.Day. BSc. Thesis Southampton University, (1990).

(23) O.Edqvist, E.Lindholm, L.E.Selin & L.Asbrink.
Physica Scripta 1,25,(1970)

(24) J.H.Batey. *Vacuum.* 37,659,(1987).

(25) P.H.Dawson. *Quadrupole Mass Spectrometry and Its Applications.* Elsevier, Amsterdam (1976).

(26) SIMION D.A.Dahl Idaho National Engineering Lab,. Idaho, (1988).

(27) D.A.Dahl,J.E.Delmore & A.D.Appelhans. *Rev.Sci.Inst.* 61,607,(1990).

(28) D.W.Turner *et al Molecular Photoelectron Spectroscopy.* Wiley Interscience. Chichester, (1970).

(29) J.H.Batey Private Communication.

(30) M.C.R.Cockett Ph.D Thesis, Southampton University, 1990

(31) W.L.Fite, H.H.Lo & P.Irving. *J.Chem.Phys.* 60,1236,(1974).

Chapter 4

The Reactions of the Alkaline Earth Metals with $O_2(X^3\Sigma_g^-)$, $O_2(a^1\Delta_g)$ and $O(^3P)$.

4.1 Introduction.

As discussed in Chapter 1 the study of metal reactions that occur in the atmosphere is of importance to the understanding of radiowave transmission properties of the atmosphere. The chemistry in the upper atmosphere, above 80 km, is dominated by ion-molecule reactions involving ions formed by ionisation due to short wavelength solar radiation. To understand this chemistry it is important to develop a kinetic model of the reactions of the metals with atmospheric oxidants and, in order to do this, knowledge of the fundamental gas phase reactions must be determined by laboratory measurement. The alkaline earth metals are thought to be important components of the upper atmosphere although *in situ* mass spectrometric measurements of atmospheric composition are ambiguous (1,2). There are problems with assignment of the mass spectra where a signal observed at a given mass to charge ratio cannot be associated with a particular ion. For example MgO^+ and Ca^+ both have mass to charge ratio, m/z, of 40. One of the objectives of a kinetic model would be to aid in the assignment of mass spectra by predicting possible ratios of $[MO^+]/[M^+]$ and $[MO_2^+]/[MO^+]$ from laboratory measurements of rate constants. Thirteen reactions thought to be important in metal-oxygen upper atmosphere chemistry are presented in Table 4.1 and form the basis of the steady state kinetic model of Murad (1). Reaction 14 was not included in the model but is a possibility investigated in this work. Reactions 5 and 14 are both chemi-ionisation reactions as defined in Chapter 1, reaction 5 being dominant in the upper atmosphere where most oxygen is present in its atomic form. Investigations have been undertaken in this work to study reactions of the metals Mg, Ca, Sr and Ba with the oxidants $O_2(X^3\Sigma_g^-)$, $O_2(a^1\Delta_g)$ and $O(^3P)$.

Gas phase reactions of the alkaline earth metals have also been extensively studied because of their fundamental interest. These reactions have a special place in the history of reaction dynamics being amongst the first to be studied by crossed molecular beam techniques - "the early alkali age." (3). Reactions involving these metals have been studied under molecular beam conditions revealing a rich variety of reaction dynamics and mechanism (4 (a)-(f)). Individual studies have been directed at specific reaction channels concentrating on the neutral products and the distribution of the available reaction enthalpy between the products (5). Products of neutral reactions can also be in excited states from which chemiluminescence can occur. There have been further studies concentrating specifically on the chemi-ionisation channel (4(f)) in metal plus oxidant reactions.

Of the group II metals, the reactions of barium have been most extensively studied by a variety of techniques. In molecular beam studies the reaction

4.1 $$Ba + O_2 \rightarrow BaO + O$$

Table 4.1

Possible reactions involving metal and oxygen in the upper atmosphere. [a]

(1)	$M^+ + O_3 \rightarrow MO^+ + O_2$
(2)	$M^+ + O_2 + X \rightarrow MO_2^+ + X$
(3)	$MO_2^+ + O \rightarrow MO^+ + O_2$
(4)	$MO^+ + O \rightarrow M^+ + O_2$
(5)	$M + O \rightarrow MO^+ + e^-$
(6)	$M^+ + O_2 \rightarrow MO^+ + O$
(7)	$NO^+ + M \rightarrow M^+ + NO$
(8)	$O_2^+ + M \rightarrow M^+ + O_2$
(9)	$M + h\nu \rightarrow M^+ + e^-$
(10)	$MO + h\nu \rightarrow MO^+ + e^-$
(11)	$NO^+ + MO \rightarrow MO^+ + NO$
(12)	$O_2^+ + MO \rightarrow MO^+ + O_2$
(13)	$MO^+ + e^- \rightarrow M + O$
(14)	$M + O_2 \rightarrow MO_2^+ + e^-$

In this table M = metal, X = a third body. The concentration of X is taken to be the total number density at a given altitude.

(a) Reference 1

has received most attention (4,5,6,7) as the some BaO is formed in an electronically excited state and was once thought a possible candidate for a chemical laser. Other possible reactions such as chemi-ionisation (4(a)) have been noted as minor reaction channels. Other techniques have been used to study the reactions of both ground state and excited state metal atoms in the real time domain producing reaction rate constants complementing the results of molecular beam studies (8). However all investigations of the chemi-ionisation channel have concentrated on the detection of the ion either by fluorescence or by mass spectrometry. By contrast, some initial studies have been carried out in this laboratory to measure the electron energy distributions from the reactions of barium and strontium with $O_2(X^3\Sigma_g^-)$ (9). Both M + O_2 reactions produced electron spectra with band maxima calibrated as 0.56±0.04 eV and 0.83±0.03 eV respectively (9) although these values were thought unreliable because of a large extrapolation from the calibration band used to calibrate the energy scale. These spectra were recorded on a single detector instrument without a reaction cell and hence pre-acceleration could not be used. Some ion measurements were attempted but no ions were observed. The study of these chemi-ionisation reactions for M = Ba, Sr, Ca and Mg is continued and extended in this work.

A series of investigations has been undertaken to study the reactions of Mg, Ca, Sr, and Ba with the oxidants $O_2(X^3\Sigma_g^-)$, $O_2(a^1\Delta_g)$, and $O(^3P)$. Preliminary investigations have also been carried out for the reactions of the metal monoxides with $O_2(X^3\Sigma_g^-)$, $O_2(a^1\Delta_g)$, $O(^3P)$ and $H_2O(X^1A_1)$. All reactions have been studied by chemi-electron spectroscopy with preliminary chemi-ion measurements being performed only for the M + $O_2(X^3\Sigma_g^-)$ reactions. These investigations were carried out towards the end of extensive modifications and instrumental development that are described in Chapter 3. The results are presented in the following sections with their interpretation. Suggestions for future experiments, instrumental development and the application of the results to meteor chemistry will also be presented.

4.2 Generation of $O_2(a^1\Delta_g)$ and $O(^3P)$.

In the upper atmosphere, due to the presence of short wavelength solar radiation, oxygen is found not only in its molecular ground state but also in excited molecular states and predominantly as atomic oxygen. In the laboratory, $O(^3P)$ may be generated by microwave discharge (2.45 GHz) of flowing molecular oxygen $O_2(X^3\Sigma_g^-)$ in a boric acid coated glass inlet tube (10). The discharge produces a plasma from which $O_2(a^1\Delta_g)$ and $O(^3P)$ emerge. Boric acid has been found to improve the yield of the discharge products by preventing deactivation and recombination reactions at the wall of the inlet tube. The relative yield of each species from the discharge may be measured by recording the HeIα photoelectron spectrum; typical spectra are presented in Figure 4.1. From the absolute photoionisation cross-sections for each process (10), at the HeIα energy, the relative yields of the two products may be determined for a given set of experimental conditions. It is possible to selectively deactivate the $O(^3P)$ atoms by the inclusion of glass wool between the discharge and the spectrometer. The role of each metastable species in a reaction may then be determined by

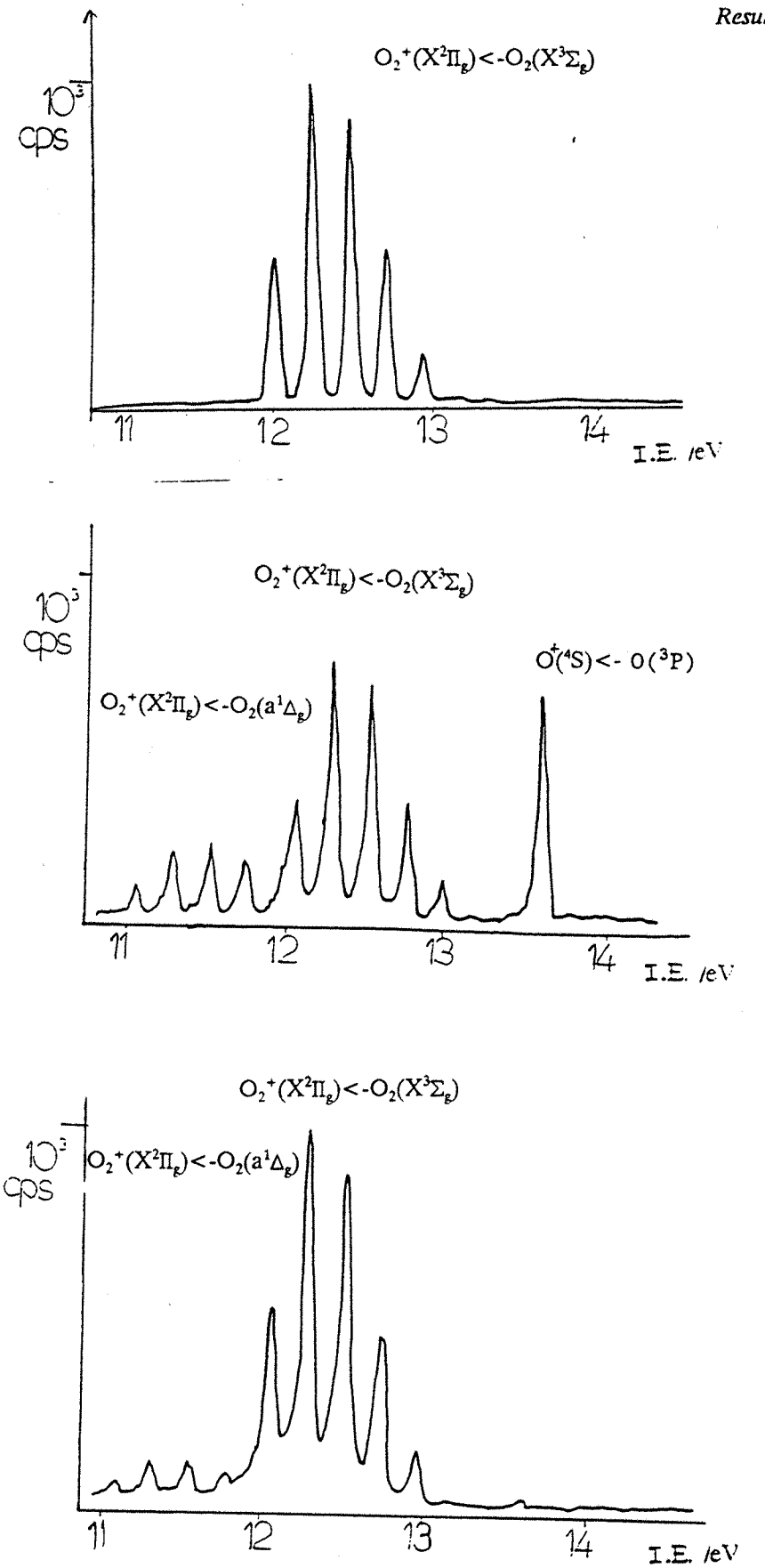

Figure 4.1 The photoelectron spectra of discharged molecular oxygen showing the yield of the discharge products:
(a) without discharge
(b) with discharge, $O_2(X^3\Sigma_g^-)$, $O_2(a^1\Delta_g)$ and $O(^3P)$
(c) with $O(^3P)$ glass wool deactivation

observing the reaction with both discharge products present and then repeating the observation with $O(^3P)$ deactivated. The deactivation efficiency depends on the physical properties of the glass wool and as a result varies from experiment to experiment. Typical relative partial pressures from a given set of experimental conditions are: $O_2(X^3\Sigma_g^-)$: $O_2(a^1\Delta_g)$: $O(^3P)$, 100:15:22, and with glass wool deactivation of $O(^3P)$, 100:12:5, consistent with those obtained elsewhere (10).

The chemi-electron, chemi-ion spectrometer has two separate inlet tubes for the oxidants, one supplying the reaction cell and the other supplying the ion lens. The yield of $O_2(a^1\Delta_g)$ and $O(^3P)$ from the discharge can only be determined for the supply to the reaction cell (by photoelectron spectroscopy) but this is not possible for the supply to the ion lens. Consequently, as the yield from the discharge is strongly dependent on the physical condition of the glass tube and the oxygen pressure, the oxidant partial pressure will be different in the two reaction regions. This is one of the shortcomings of the dual inlet system. which will be solved by the design of a parallel chemi-electron, chemi-ion spectrometer.

4.3 Results of the reactions of Ba with $O_2(X^3\Sigma_g^-)$, $O_2(a^1\Delta_g)$ and $O(^3P)$.

Barium metal (99.9% pure, BDH) was evaporated from both Mo and W furnaces at a temperature of 850±20 K. Evaporations were stable over a period of three hours during which spectra could be recorded. The observed electron spectrum is presented in Figure 4.2 a). It shows one band calibrated against the $O_2^+(B^2\Sigma_g^-)$ <- $O_2(X^3\Sigma_g^-)$ photoelectron band recorded with HeIα radiation. The band maximum was calibrated several times (≈20) during separate experiments and it was found to vary in position within the range -0.4 to +0.2 eV. This variation is greater than the experimental error in calibration (0.1 eV) and consequently represents a real effect. Several further properties of the band have been studied to establish its identity. The oxygen dependence of the band intensity was determined and found to show a maximum at $5x10^{-5}$ torr, Figure 4.3. The oxygen partial pressure is that measured by an ionisation gauge situated on the wall of the ionisation chamber. The oxidant pressure within the reaction cell is thought to be higher by an order of magnitude, than that measured by the gauge as determined by comparing the oxygen photoelectron intensity with and without the reaction cell. The band shown in Figure 4.2(a) has been found to be dependent on the barium partial pressure by switching off the heating to the furnace and its disappearance when the sample has completely evaporated. Thus the band is attributed to the gas phase reaction of Ba with $O_2(X^3\Sigma_g^-)$.

The observed variation in the position of the band and its occurrence at negative kinetic energy suggests the band may not be due to electrons but possibly negative ions. The analyser will energy analyse all negative particles but the calibration of a signal arising from negative ions against a known electron energy scale would give rise to erroneous results. The trajectories of electrons are sensitive to small field variations so bands associated with electrons will move with the perturbation and the linearity of the electron energy scale will be retained. However, the perturbation of possible ion trajectories by local fields will be smaller as a result of the ions' greater inertia and consequently ions may be apparently shifted in energy with respect to an electron-calibrated energy scale. The

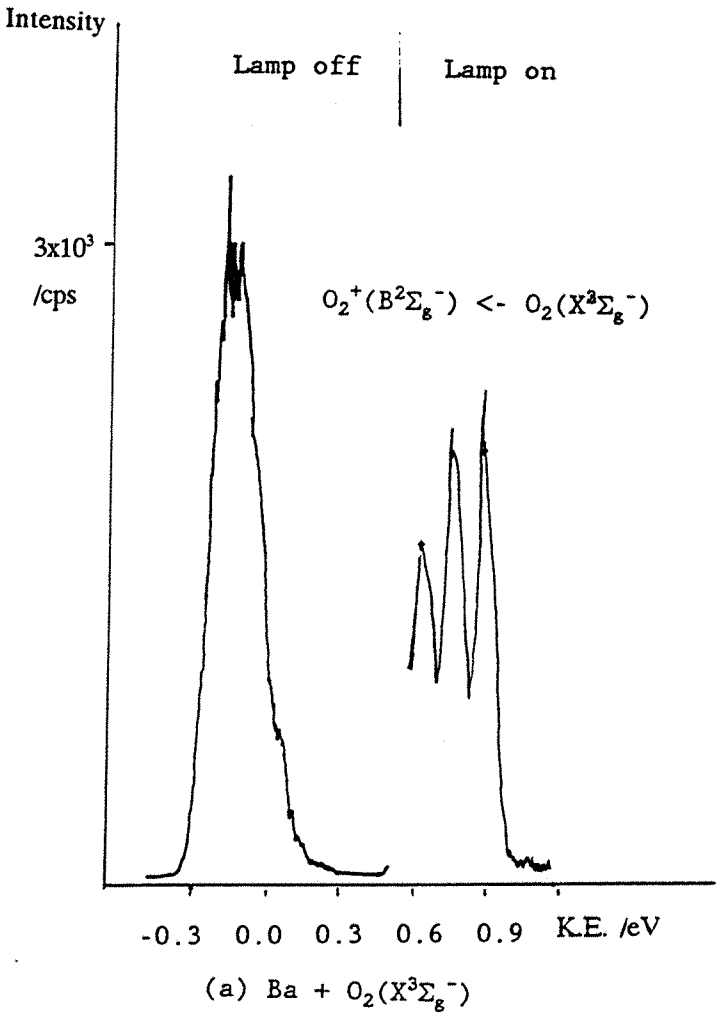

(a) Ba + $O_2(X^3\Sigma_g^-)$

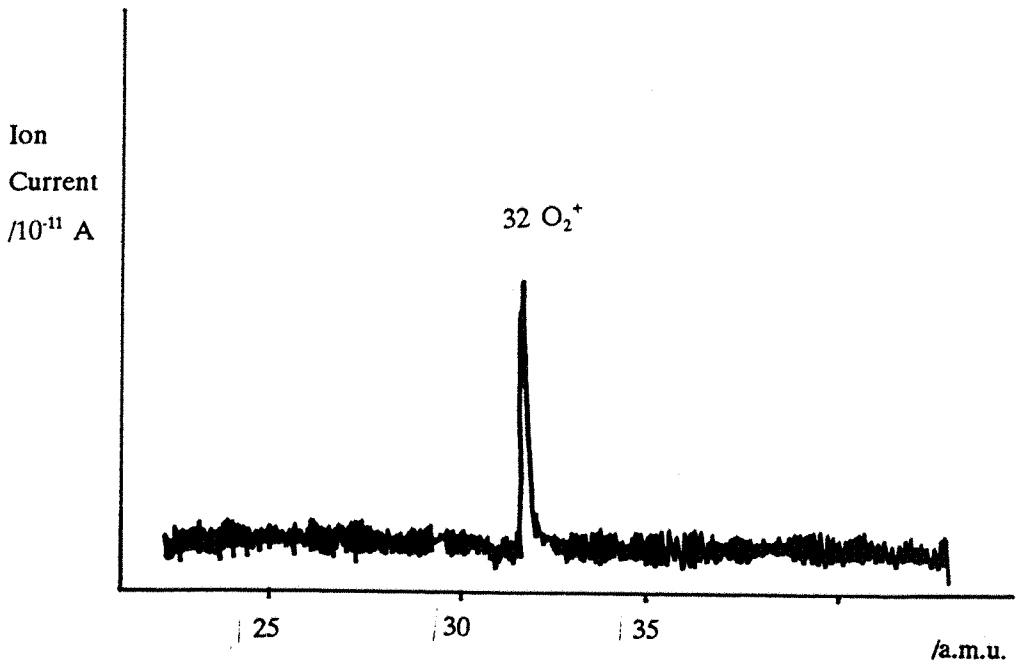

(b) The secondary ion spectrum

Figure 4.2 (a) The electron spectrum of Ba + $O_2(X^3\Sigma_g^-)$
(b) The secondary ion spectrum

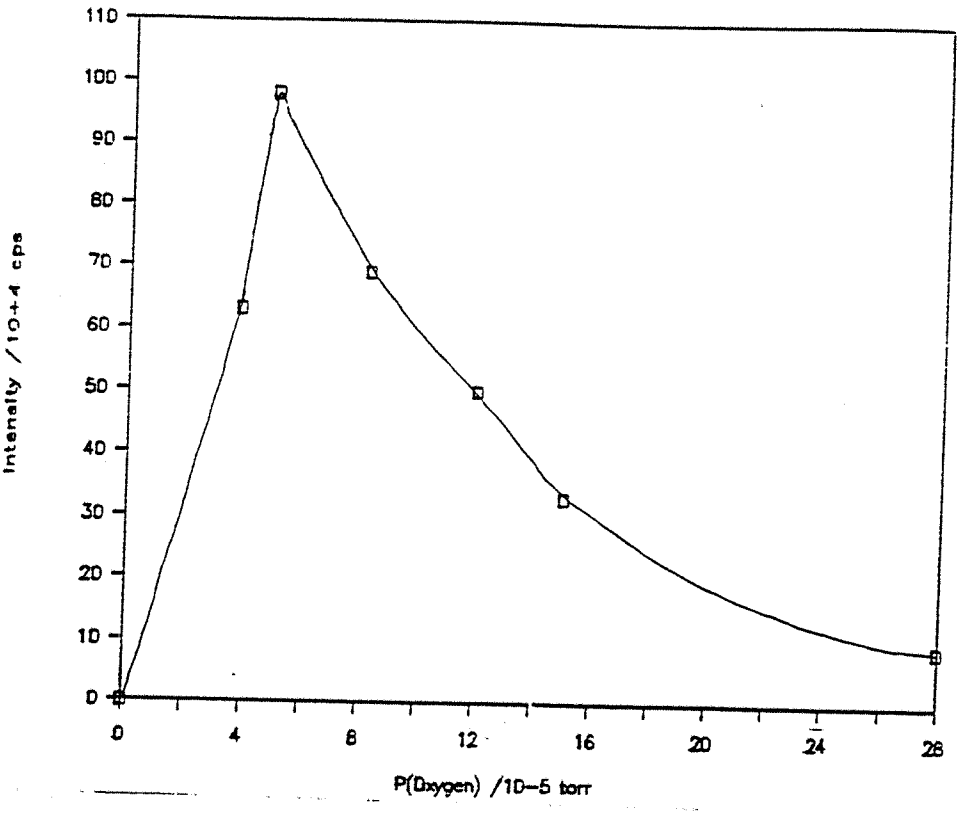

Figure 4.3 The oxygen partial pressure variation with the Ba + $O_2(X^3\Sigma_g^-)$ band intensity at the band maximum

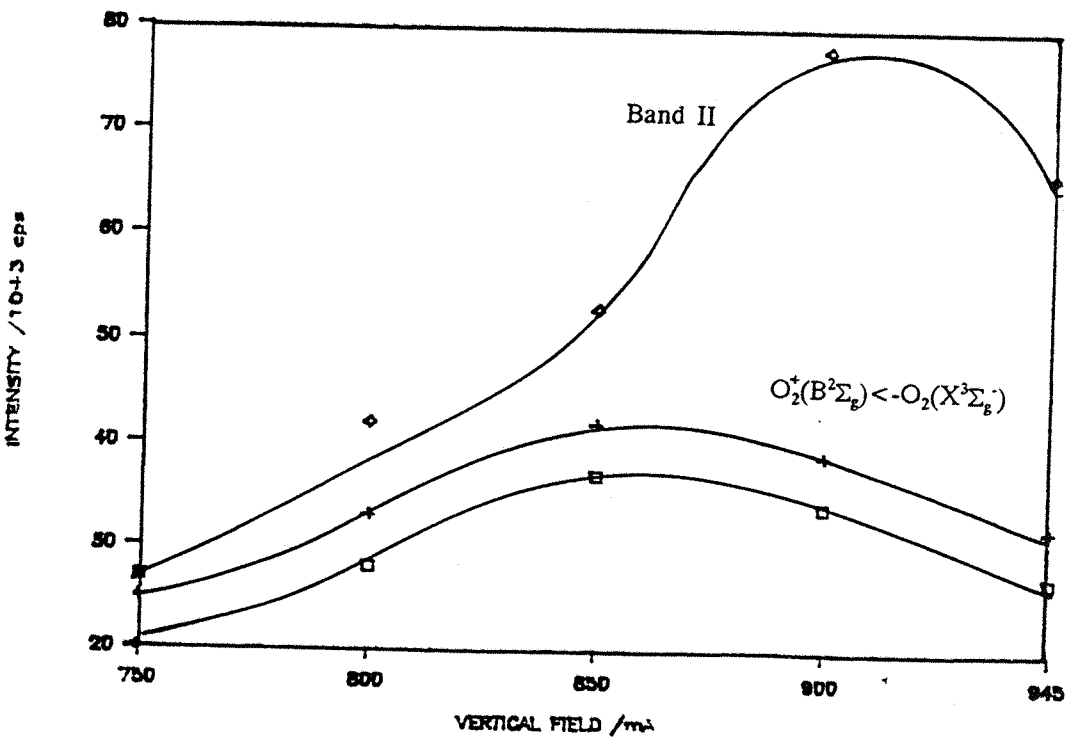

Figure 4.4 The variation of the band maximum intensity with the vertical magnetic field for the reaction Ba + $O_2(X^3\Sigma_g^-)$

different inertias of ions and electrons suggests that variation of the magnetic field in the Helmholtz coils (see Chapter 3) surrounding the instrument will affect the behaviour of the ions and electrons differently.

The force on a charged particle moving in a magnetic field is the Lorentz force and is given by $F = e(\underline{v} \times \underline{B})$, where e is the electronic charge, $\underline{v}$ is the velocity vector and $\underline{B}$ is the magnetic field. The acceleration of a negative ion will depend on its velocity, which will be less than that of an electron with the same energy. The effect of the Lorentz force will be different for an electron and a negative ion although it is not easy to predict how this will manifest itself in the spectrum. The small variation in magnetic field due to changing the current in the Helmholtz coils may not change the detected energy of the electrons or ions. It may however have a more pronounced effect on the focusing properties of the analyser with a resulting larger variation of band intensity.

A series of investigations to measure the dependence on the magnetic field variation on the bands shown in Figure 4.2(a) was performed. The Helmholtz coils surround the entire instrument and the current in each coil is independently variable. The currents in the coils as indicated in Figure 3.1 under optimised conditions are typically Vert = 0.890 A, E/W = 0.400 A and N/S = 0.018 A, and generate a resultant magnetic field above the ionisation chamber of nearly zero, as measured by a Hall Probe. Variation of a current in a given coil causes greatest field variation in its specified direction and hence one component of the resultant magnetic field is changed most.

To quantify the observed field variation the effect of varying the current in each of the Helmholtz coils on the resultant magnetic field as measured with a Hall probe was determined. The currents in the Helmholtz coils are optimised with respect to the HeIα photoelectron spectrum of O_2 as described in Chapter 3. A typical set of values is:

Vertical = 0.896 A, E/W = 0.400 A and N/S 0.018 A.

Variation of the current in the coils generating the vertical field throughout its range 1.3 A - 0.65 A showed a detected variation in the measured vertical field corresponding to -130 milligauss at 1.3 A and 100 milligaus at 0.65 A. The measured field was nearly zero (< 5milligauss) at the optimised value. Variation of the other coil currents had little effect on the field measured in this direction (< 2 milligauss). Variation of the current in the coil generating the N/S field showed a similar behaviour. Variation throughout its range 0.0 A to 0.5 A showed a N/S field variation from +8.4 milligauss at 0.00 A to -9.4 milligauss at 0.5 A. The measured field in the other directions varied by only 2 milligauss for variation of the N/S current. Similar behaviour was observed for the E/W field. A current of 0.5 A generated a field of -2.1 milligauss in the E/W direction and + 8.0 milligauss for 0.230 A. The variation in measured field in other directions over the same current range was small. These experiments showed that variation of the current in the Helmholtz coils most greatly affected the magnetic field in the direction of the coils' field with little variation for the other components. The resultant magnetic field at any point within the spectrometer is however the

vector sum of the three components (the field was measured with a Hall probe on top of the ionisation chamber).

Qualitatively, the vertical field changes the intensity in an electron spectrum by distorting the trajectories relative to the entrance slits. Similarly, the E/W field adds a component to the centripetal force of the electrons moving around the hemispheres and hence the electrons will be focused at a different applied voltage. The N/S field affects the focusing properties of the analyser having most effect on the resolution.

The ion spectrum presented in Figure 4.2 (b) shows one signal of m/z = 32, although the full mass range of the spectrometer was scanned. This is attributed to the formation of secondary ions by analogy with process 3.10 described in Chapter 3. This signal is not present when the extraction voltage on the ion lens falls below 12 V. No signals corresponding to ions of higher m/z were observed. This is a preliminary chemi-ion investigation, further experiments need to be performed to observe primary ions.

The reactions of Ba with $O_2(a^1\Delta_g)$ and $O(^3P)$ in the presence of $O_2(X^3\Sigma_g^-)$ showed no new features in the electron or ion spectra. The position of the band in the electron spectrum did not move outside the region of calibration previously determined, and its shape remained constant. A variation of signal intensity was observed, being somewhat smaller with the discharge present than without. This was consistent with the reduced $O_2(X^3\Sigma_g^-)$ partial pressure on discharging molecular oxygen.

4.4 Results of the reactions of Sr with $O_2(X^3\Sigma_g^-)$, $O_2(a^1\Delta_g)$ and $O(^3P)$.

Strontium metal (99.9% pure, Cerac) was evaporated from both Mo and W furnaces at a temperature of 950±20 K. Evaporations were again stable over a period of about three hours during which spectra could be recorded. The electron spectrum obtained for the reaction of Sr + $O_2(X^3\Sigma_g^-)$ is presented in Figure 4.5 and shows two bands arising from the reaction. The ion spectrum recorded under similar conditions is not shown but contains a single peak of m/z = 32 attributed to secondary ion formation (cf Figure 4.2). The following nomenclature is introduced to identify the bands: the band to higher kinetic energy is labelled Band I and that to lower kinetic energy is labelled Band II; by analogy the band in the Ba + $O_2(X^3\Sigma_g^-)$ spectrum is labelled Band II because of its similar properties. Band I for the Sr + $O_2(X^3\Sigma_g^-)$ reaction Figure 4.5, has a band maximum calibrated as 0.9 ± 0.1 eV. It is an asymmetric band with a tail to higher kinetic energy with a high kinetic energy onset at 1.4 ± 0.2 eV. It is relatively broad in shape and there is no reproducible vibrational structure. Band II shows a similar variation in calibrated band maximum from -0.1 to +0.2 eV to that observed for the Ba reaction. Again, this variation is well beyond the limits of experimental error and is a real effect.

As for the Ba reactions, the oxygen dependence of the band intensities was determined and the result is presented in Figure 4.6. At very low oxygen pressures and when no oxygen was admitted to the reaction cell, a very sharp and intense signal (10^4 cps at maximum intensity) was recorded

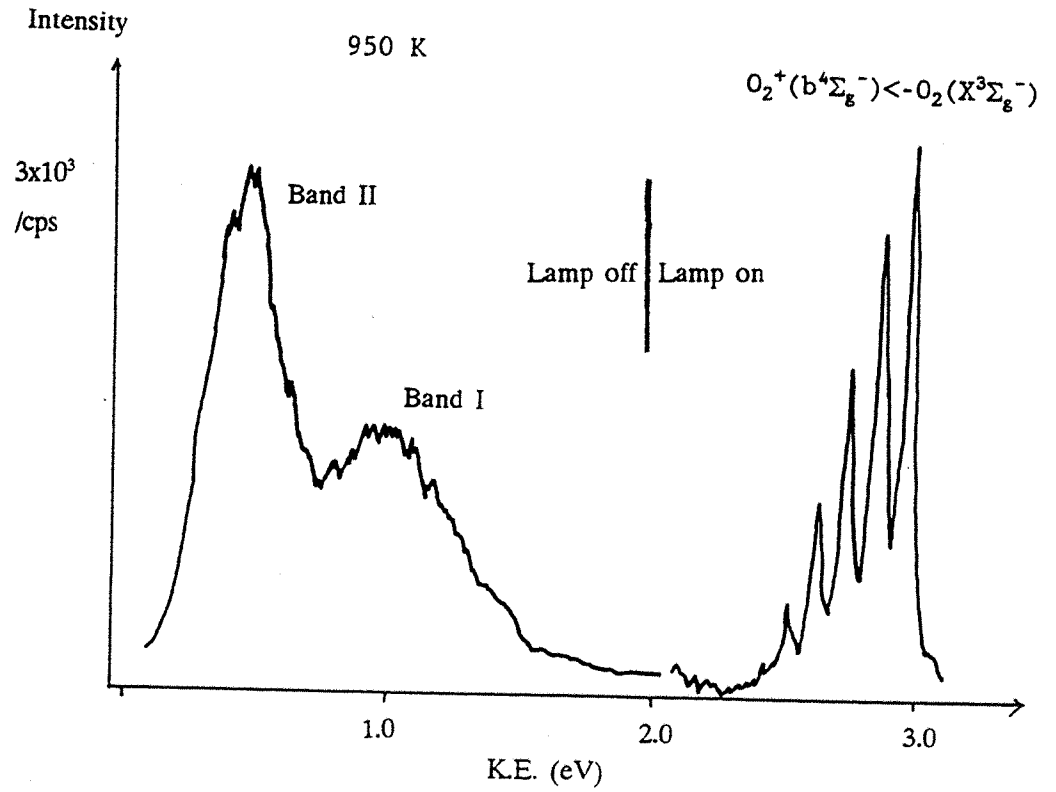

Figure 4.5 The electron spectrum for the reaction Sr + $O_2(X^3\Sigma_g^-)$

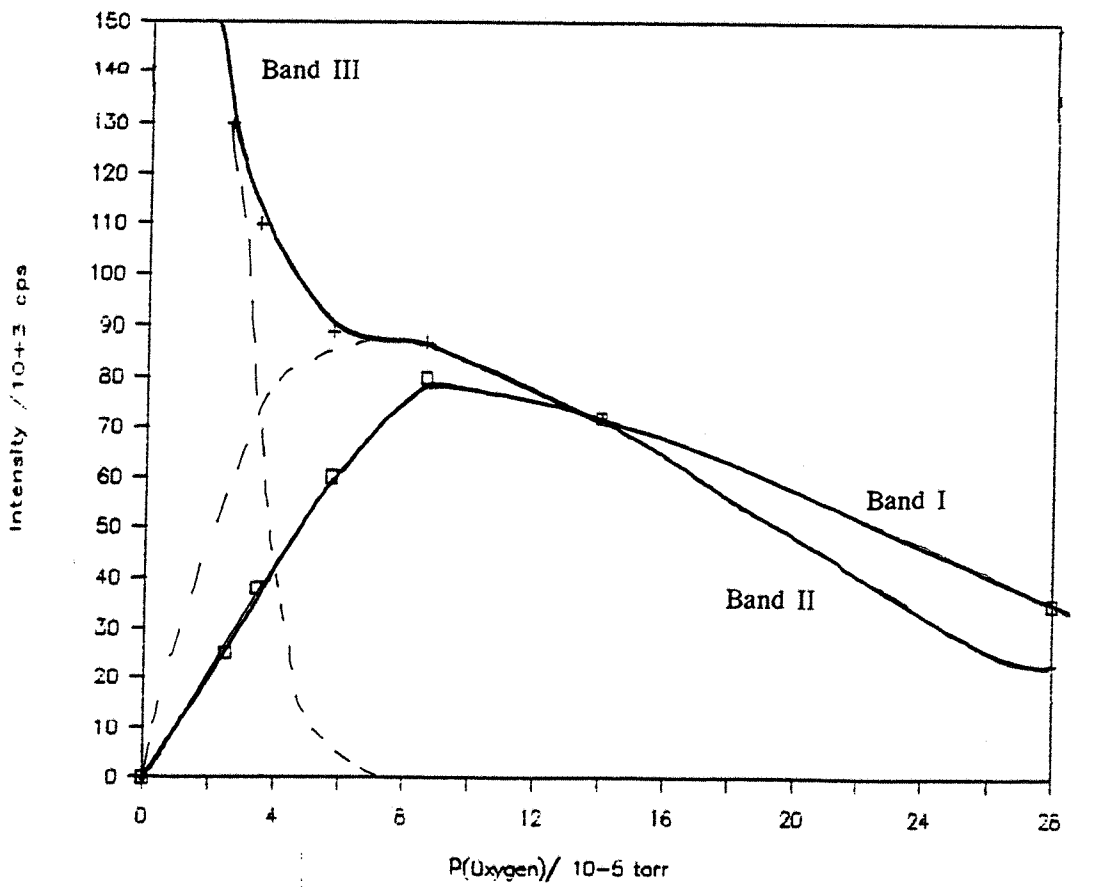

Figure 4.6 The oxygen partial pressure variation with the Sr + $O_2(X^3\Sigma_g^-)$ band intensity at the band maximum for Bands I and II, showing the onset of Band III

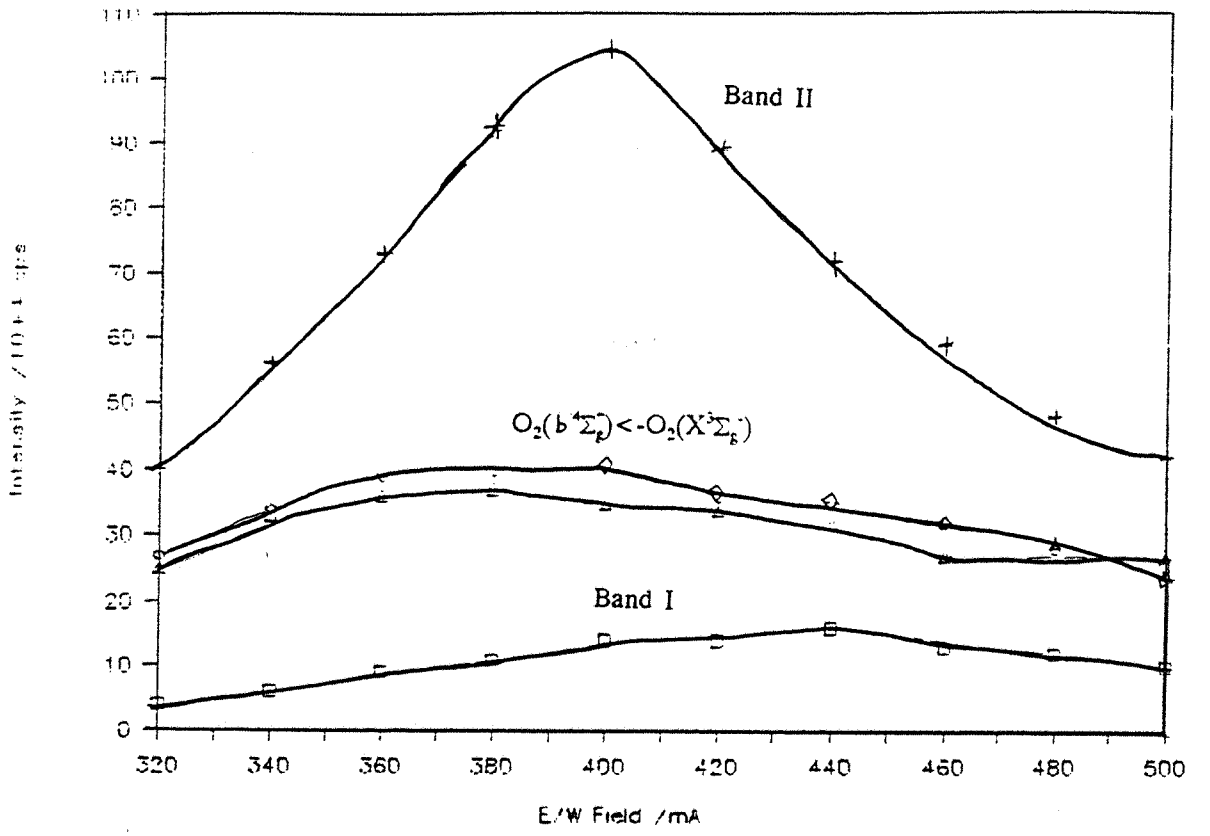

Figure 4.7 Variation of intensity (height) with E/W magnetic field for Bands I and II for the reaction Sr + $O_2(X^3\Sigma_g^-)$

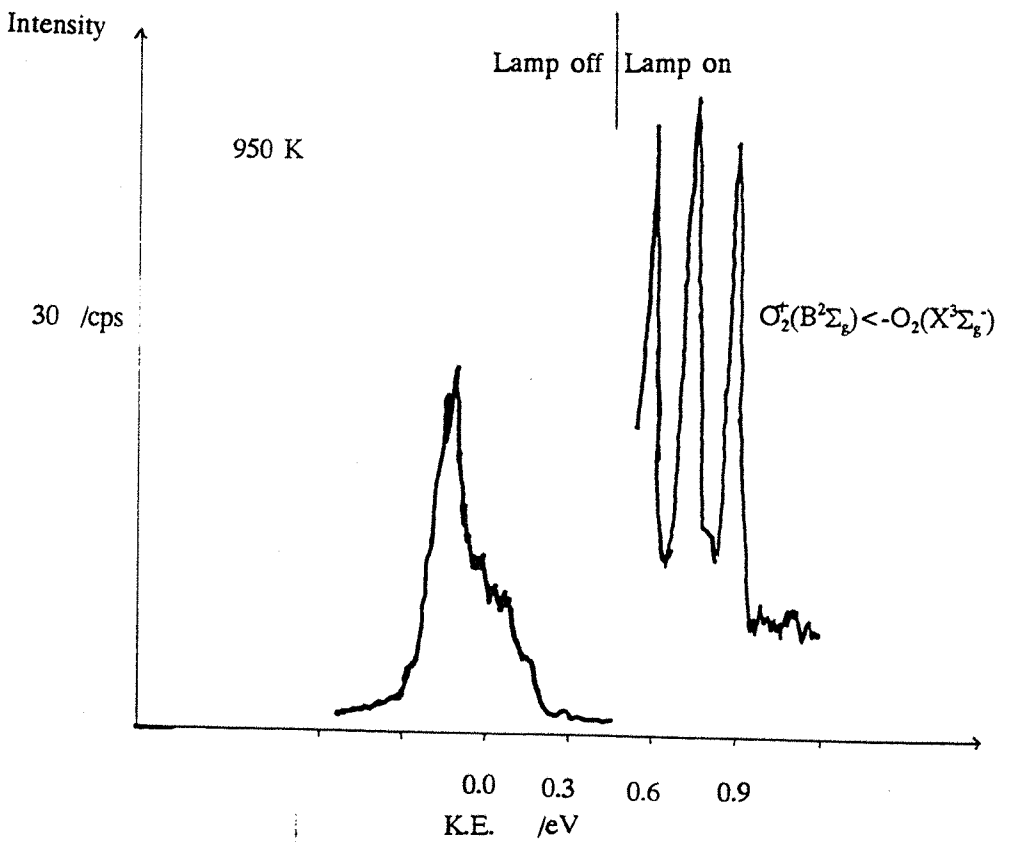

Figure 4.8 The electron spectrum for the reaction Sr + $O_2(X^3\Sigma_g^-)$ + $O_2(a^3\Delta_g^-)$ + $O(^3P)$

at about 0 eV band maximum. (It was not possible to calibrate the band maximum since there was no calibrant, oxygen, in the reaction cell.) This is band was labelled Band III. Its dependence on the sample vapour pressure was determined. If the furnace was allowed to cool, the signal disappeared. If a used but empty furnace was heated to 2200 K no electron signal was observed, also it was not observed at the end of the evaporation. Thus the signal cannot be attributed to a reaction with oxygen and alloyed furnace/Sr material. It was stable in time throughout an evaporation and found to be dependent only on a heated furnace containing a Sr sample.

The variation of the relative intensities of Bands I and II with furnace temperature has been studied. As the furnace temperature is increased two effects occur simultaneously; firstly the metal vapour pressure increases with temperature and secondly the translational energy of the metal also increases with temperature. If the vapour pressure variation with temperature is large then this effect will dominate. For the Sr + $O_2(X^3\Sigma_g^-)$ reaction at low temperature (≈1400 K) Band II was more intense than Band I by a factor of about five. As the temperature increases to 1600 K, Bands I and II were of comparable intensity. At 1700 K Band I had a slightly greater intensity although the difference was small.

A similar series of experiments, as outlined for Ba, was undertaken to determine the dependence of the two bands on magnetic field. This is a useful experiment since both Bands I and II are present in the spectrum and the different variation of the bands may be directly observed. The results are presented in Figure 4.7. It can be seen that the behaviour of Band II is significantly different from that of Band I when the applied E/W current is changed and this is consistent with the bands being associated with different negative species. The variation of Band I with magnetic field is found to follow the variation of the electrons from the photoelectron calibration band. The effects for the other fields are similar but less pronounced. These observations when considered with the calibration of Band II at negative energy suggest it is not attributable to electrons and is probably negative ions. It should be noted that Figures 4.4 and 4.7 present the variation with different components of the resultant magnetic field, Vertical and E/W respectively. Hence variation of the component magnetic fields had a different effect on the resultant magnetic field present in an individual experiment.

The reaction Sr + $O_2(a^1\Delta_g)$ in the presence of $O_2(X^3\Sigma_g^-)$ was carried out by discharging flowing oxygen and deactivating the oxygen atoms. The photoelectron spectrum of the oxidant mixture showed that deactivation was efficient and the resulting chemi-electron spectrum was due to reaction of the metal with $O_2(a^1\Delta_g)$ and $O_2(X^3\Sigma_g^-)$. No electron signals were observed for the reaction of Sr + $O_2(a^1\Delta_g)$ only a background count of 2 cps remained. When the glass wool was removed, $O(^3P)$ was allowed to enter the reaction cell the spectrum shown in Figure 4.8 was observed. The signal was very weak, about 10 cps at its maximum, but is of well defined shape. It was calibrated by the fifth band of oxygen and was found to have an energy at the band maximum in the range -0.1 and +0.1 eV; this uncertainty is greater than the experimental error. Experiments to determine its dependence on magnetic field show a variation similar to that observed Band II in the Ba + $O_2(X^3\Sigma_g^-)$, although with such a weak band there was some uncertainty. These results for the

reaction of Sr + $O_2(a^1\Delta_g)$ and Sr + $O(^3P)$ mixtures were reproducible: they were however unexpected and will be considered fully in the discussion.

4.5 Results of the reactions of Ca with $O_2(X^3\Sigma_g^-)$, $O_2(a^1\Delta_g)$ and $O(^3P)$.

The reaction of Ca with $O_2(X^3\Sigma_g^-)$ was investigated by evaporating Ca (99.9% pure, Interchem UK.) from both Mo and W furnaces. Evaporations were again stable over a period of up to three hours during which spectra could be recorded. The chemi-electron and chemi-ion spectra obtained are presented in Figure 4.9 (a) and (b), respectively. The chemi-electron spectrum, Figure 4.9, (a) shows two band systems labelled Bands I and II. Band I has a band maximum at 0.3 ± 0.1 eV calibrated against the fifth oxygen band. It had a tail to higher kinetic energy with a high kinetic energy onset at 0.9 ± 0.2 eV. It is similar in shape to Band I recorded for the reaction of Sr with $O_2(X^3\Sigma_g^-)$ but was found at lower energy. Band II is found have an energy calibrated at its band maximum in the range -0.1 to +0.1 eV - again, a greater uncertainty than experimental error. The dependence of the band intensities on furnace temperature was similar to that of Band II for the Sr + $O_2(X^3\Sigma_g^-)$ reaction, but at 1500 K Band II completely disappeared and only Band I remained. Band I is shown alone in Figure 4.10, and is of the same shape and band maximum (within experimental error) as that recorded at lower temperature. Some indication of vibrational structure in this band was seen, although this structure was not completely resolved. The behaviour of bands I and II with respect to oxygen partial pressure variation and magnetic field dependence is very similar to the behaviour of the Sr + $O_2(X^3\Sigma_g^-)$ Bands I and II, producing results similar to Figures 4.6 and 4.7.

The ion spectrum presented in Figure 4.9 (b) was the first spectrum found to contain signals attributable to metal containing ions, m/z = 40, Ca^+ and m/z = 56, CaO^+. It may be significant that these are of low mass-to-charge ratio given the discussion of quadrupole mass discrimination of the previous chapter. The spectrum was recorded using high extraction voltages on the ion lens, +20 V on the hat, 0.0 V on the second electrode and -5 V on the final electrode. No ion signals were observed when the hat voltage fell below +7 V. The relative intensities of the m/z = 40, 32, 56 signals showed some variation with oxygen partial pressure, the maximum of the m/z = 56 signal corresponding to 6×10^{-4} torr as measured on the ionisation gauge. The signals at m/z = 32 and 40 were the first to be observed at the onset of the reaction at an oxygen partial pressure of 1.8×10^{-4} torr. The precise pressure variation has yet to be determined and will be the subject of a further study.

The reactions of Ca + $O_2(a^1\Delta_g)$ and Ca + $O(^3P)$ were also carried out, both species being produced from the discharge in good yield. For the reaction Ca + $O_2(a^1\Delta_g)$ again in the presence of $O_2(X^3\Sigma_g^-)$ no electron spectrum was observed. The background level was 2 cps throughout the low energy range. The reaction Ca with $O(^3P)$ was studied by removing the glass wool from the inlet tube and the resulting spectrum is presented in Figure 4.11. It shows a very weak but well defined band. Calibration with the fifth oxygen band showed a variation in position between -0.2 to +0.1 eV. Experiments to measure its dependence on magnetic field revealed a behaviour very similar to

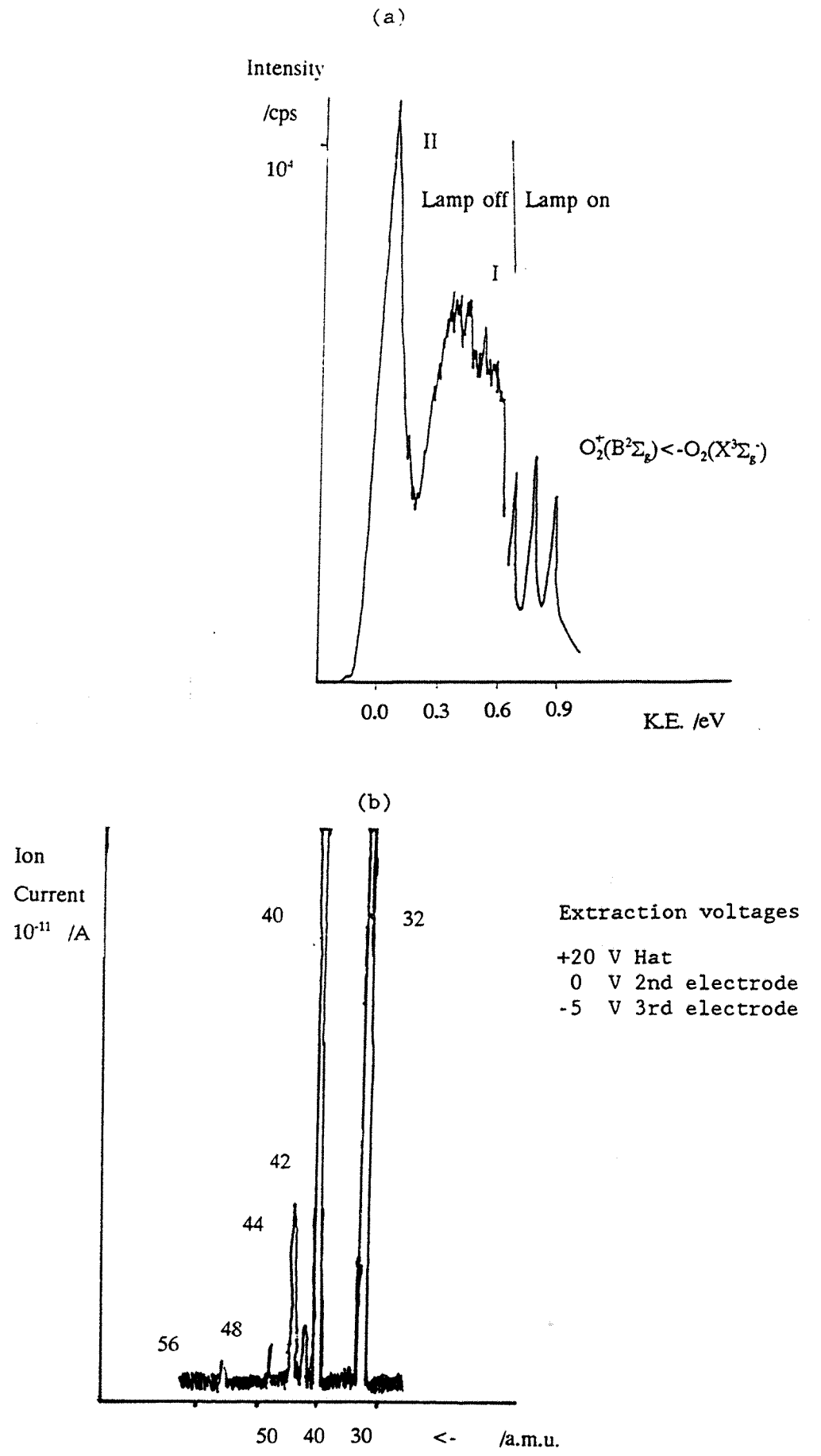

Figure 4.9 The electron and ion spectra for the reaction Ca + $O_2(X^3\Sigma_g^-)$

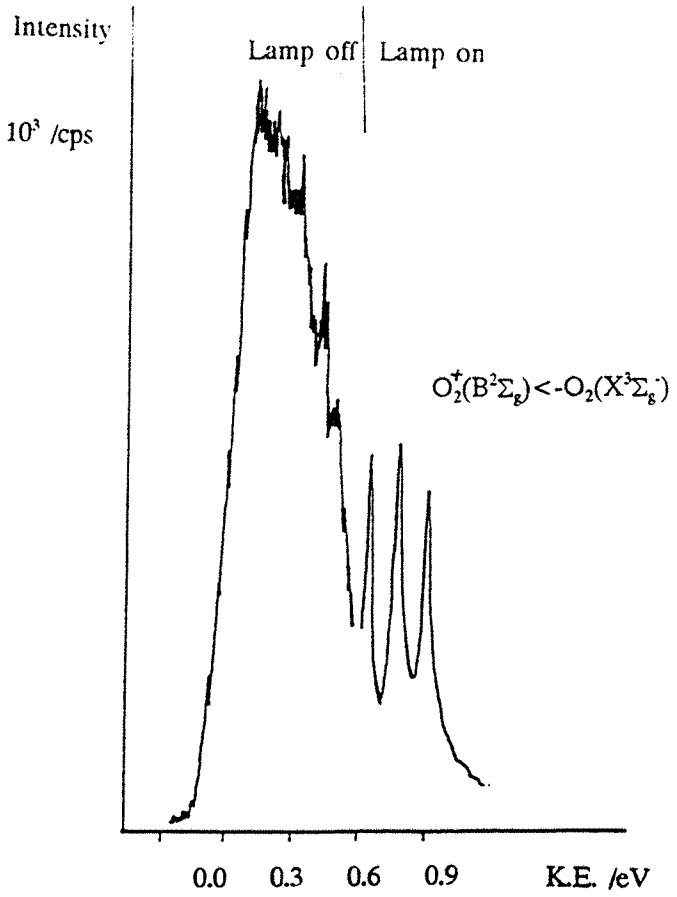

Figure 4.10 The electron spectrum for the reaction Ca + $O_2(X_3\Sigma_g^-)$ at 1500K

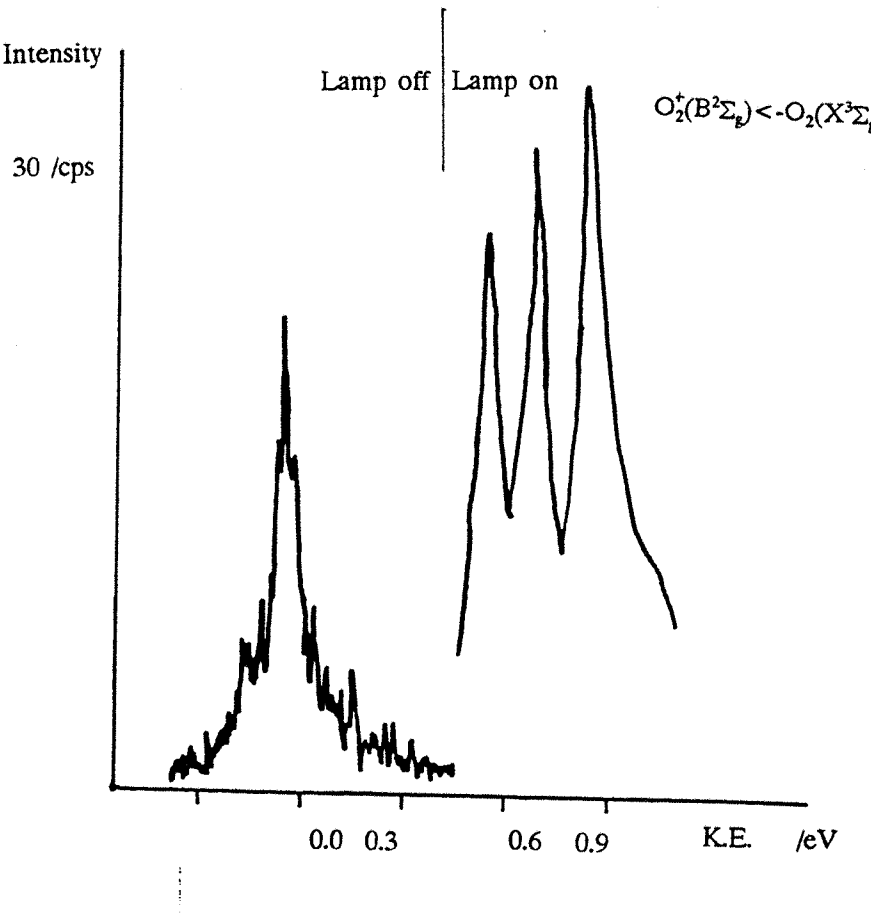

Figure 4.11 The electron spectrum for the reaction Ca + $O(^3P)$

Band II observed in the reactions of Ba and Sr with $O_2(X^3\Sigma_g^-)$. The band had very similar properties to that observed for the reaction of Sr with $O(^3P)$, it was also dependent on the metal vapour pressure and the oxygen partial pressure.

4.6 Results of the reactions of Mg with $O_2(X^3\Sigma_g^-)$, $O_2(a^1\Delta_g)$ and $O(^3P)$.

A similar series of investigations to those presented for the other alkaline earth metals was carried out for the reactions of Mg. However, no ions or electrons were observed for any of the reactions of Mg with the above mentioned oxidants.

4.7 Discussion - The Thermodynamic Model.

The electron spectra obtained for the reactions of Ca, Sr and Ba with the oxidants used are presented in summary in Figure 4.12. The measurements made from the spectra are presented in Table 4.2. These spectra have been obtained by the evaporation of the pure metal samples from Mo and W furnaces which produces an effusive beam directed into the ionisation chamber. It is possible that observed spectra may not be due to the reaction of the atomic metal with the oxidant. There are several other possible sources of electrons and ions of instrumental origin or from reactions associated with species other than the atomic metal present in the effusive beam. Consideration of these possible sources will be given before a model is presented to interpret the results obtained.

One possible source of electrons and ions comes from interaction of a hot furnace surface with the atmosphere in the ionisation chamber. Heating the furnace to 2200 K might give rise to the production of electrons by thermionic emission. However, experiments at these temperatures with an empty furnace has shown no detectable ions or electrons in the spectra recorded. A further source of ions and electrons in the ionisation chamber is the ionisation gauge but again this has been eliminated as a source of the observed signals by measurement of spectra both with and without the ionisation gauge. Finally, there is also a small partial pressure of helium in the ionisation chamber originating from the v.u.v. discharge lamp. This may possibly form He^* metastable species on contact with the hot furnace surface which may cause Penning ionisation producing electrons. Spectra have been recorded both with and without He passing into the lamp - no change is observed.

A further possible source of electrons in the ionisation chamber may be exoelectron production from the initial stages of oxidation of fresh metal surfaces (11). During the formation of a metal oxide surface small "exopatches" form which are neither completely metal or metal oxide in electronic character. The exopatches emit exoelectrons during the slow formation of an oxide layer. During the evaporation of a metal sample in a chemi-ionisation experiment the sample deposits on the surfaces of the ionisation chamber and slowly oxidises. These surfaces are possible exoelectron sources. However the processes which lead to exoelectron production are observed at pressures of 5×10^{-10} torr whereas the lowest ionisation chamber pressure achieved in these investigations was 2.5×10^{-5} torr. At such pressures surface oxidation will occur very quickly. Thus

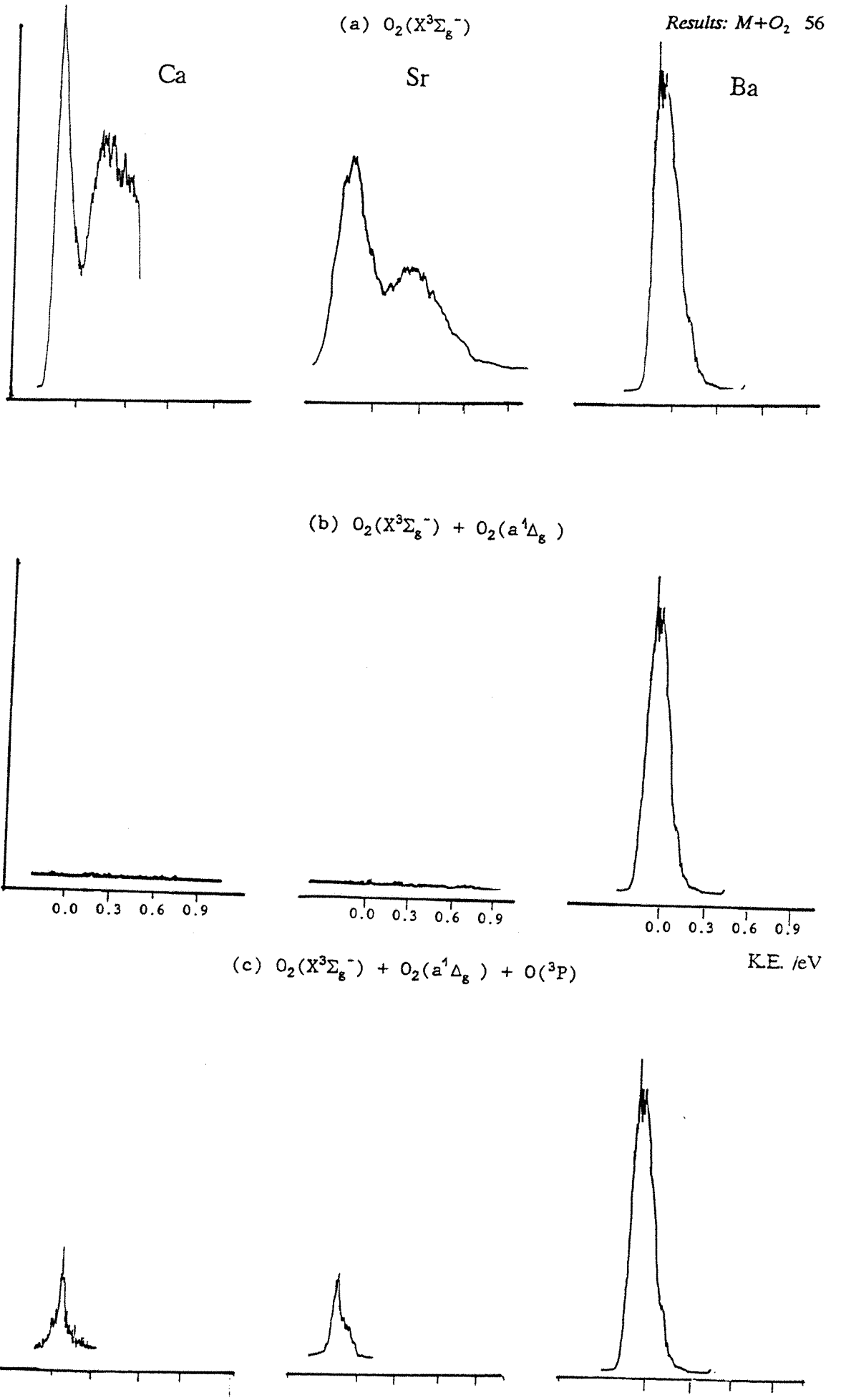

Figure 4.12 A summary of the electron spectra recorded for the reactions of the alkaline earth metals with the oxidants $O_2(X^3\Sigma_g^-)$, $O_2(a^1\Delta_g)$ and $O(^3P)$

Table 4.2

Measurements made from the electron spectra for the reactions of Ca, Sr, and Ba with the oxidants $O_2(X^3\Sigma_g^-)$, $O_2(a^1\Delta_g^-)$ and $O(^3P)$

All Values are in eV

$M+O_2(X^3\Sigma_g^-)$ Band I	Ca	Sr
Band Maximum	0.3±0.1	0.9±0.1
High Kinetic energy Onset	0.8±0.2	1.4±0.2
Estimated Reaction[a] Enthalpy	0.8±0.2	1.4±0.2

$M+O_2(X^3\Sigma_g^-)$ Band II	Ca	Sr	Ba
Observed Range of Band Maximum	0.2-0.0	-0.4-0.0	-0.2-0.2

$M+O_2(a^1\Delta_g^-)$ Band II	Ca	Sr	Ba
Observed Range of Band Maximum	-	-	-0.2-0.2

$M+O(^3P)$	Ca	Sr	Ba
Observed Range of Band Maximum	-0.1-0.0	-0.1-0.0	-0.2-0.2

(a) Reaction enthalpy is equated to the high kinetic energy onset, see Chapter 2.

production of detectable electrons by this process is thought unlikely at the pressures of the experiment.

All of the above possible sources of electrons are from regions of the ionisation chamber outside the reaction cell. An advantage of pre-acceleration is that only electrons diffusing from the reaction cell are accelerated. Thus only if electron sources elsewhere are producing electrons of absolute energy greater than the acceleration voltage (typically -1.7 V), will they appear at greater than zero on the electron energy scale. Further, if the acceleration voltage is changed signals produced by processes outside the reaction cell will move with respect to signals recorded for electrons produced in the reaction cell - no such shift has been observed for any of the spectra presented in this work.

From the above considerations the observed spectra have been shown to be dependent only on the sample metal beam reacting with the oxidant. However there are possible uncertainties in the composition of the beam. Possible contamination of the metal beam depends on the degree of oxidation of the sample during preparation. At the temperatures of evaporation all the metals studied have a vapour pressure of the atomic metal in equilibrium above the solid of 0.1 - 1.0 torr (12) and this is known to be the major constituent. However there are two sources of contamination: (i) interaction of the metal with the furnace material to produce volatile tungstites or molybdites; and (ii) evaporation of the metal oxide formed on the surface of the sample during the initial phase of the experiment. The oxides of Mg, Ca, Sr and Ba have been shown to react with Mo and W furnaces at high temperatures to produce a number of species detectable by mass spectrometry (13). Ions derived from $MgWO_3$ and $CaMo_3$ have been detected by electron impact mass spectrometry but all measurements have been made at elevated temperatures (2400 K) about 1000 K higher than the temperatures used in this experiment. Whilst the formation of these compounds may still be possible at lower temperatures, they are thought to be a minor component of the effusive beam. Further sample contamination may result from the evaporation of the oxide formed during the early part of the experiment. Evaporation of the solid metal monoxides studied in this work, has been investigated elsewhere (14) and it has been found that the products of evaporation depend on the partial pressure of oxygen in the atmosphere above the sample. The dominant vapour phase component is the atomic metal. However a number of metal oxides have been observed e.g. MO and MO_2, and their possible role in the reaction scheme will be considered after the thermodynamic model has been presented.

A thermodynamic model has been put forward to explain the results obtained on the assumption that the effusive beam contains primarily the atomic metal in its ground electronic state. The validity of this assumption will be discussed later. A table of reaction enthalpies derived from available thermodynamic data is presented for some possible bimolecular reactions of the metals with oxygen (both atomic oxygen $O(^3P)$, and molecular oxygen, $O_2(X^3\Sigma_g^-)$), Table 4.3. Inspection of the reaction enthalpies in this table shows that there are no exothermic reaction channels leading to ionic products for simple bimolecular reactions (although the error limits on some values are large.). Indeed, even the gas phase oxidation reaction to form the monoxides, reaction 3, is endothermic for

Table 4.3

Calculated reaction enthalpies for possible bimolecular reactions involving the group II metals with molecular and atomic oxygen. (values in eV)

$O_2(X^3\Sigma_g^-)$ and $O(^3P)$	Ca	Sr	Ba	Ref.
(1) $M+O_2 \rightarrow MO^+ + O + e^-$	+2.55±0.05	+1.72±0.05	+6.33±0.05	(a)
(2) $M+O_2 \rightarrow MO^+ + O^-$	+1.09±0.05	+0.36±0.05	+0.77±0.05	(b)
(3) $M+O_2 \rightarrow MO+O$	+1.17±0.05	+0.74±0.05	-0.56±0.05	(a)
(4) $M+O_2 \rightarrow M^+ + O_2$	+6.10±0.05	+5.30±0.05	+4.81±0.05	(a)
(5) $M+O_2 \rightarrow MO_2$	-	-	-5.2±0.4	(c)
(6) $M+O_2 \rightarrow MO_2^+ + e^-$	-	-	+0.2±0.5	(d)
(7) $M+O \rightarrow MO^+ + e^-$	+2.55±0.05	+1.72±0.05	+1.17±0.05	(a)
(8) $MO+O \rightarrow MO_2^+ + e^-$	-	-	+0.7±0.5	(d,c)

(a) Reference 27

(b) Reference 28 (a,b)

(c) Reference 29

(d) Reference 30

Ca and Sr and only mildly exothermic for Ba. The possibility of a reaction becoming exothermic at 1000 K due to increased translational energy of the reactants is remote. The most likely channel to explain the observed results from the data presented in Table 4.3 is the associative ionisation reaction 6 which for Ba + $O_2(X^3\Sigma_g^-)$ may be thermoneutral given the uncertainty in the data. Unfortunately it is not possible to calculate the reaction enthalpy of reaction 6 for the reactions of Sr and Ca with $O_2(X^3\Sigma_g^-)$ as the required thermodynamic data are not known. Similar reactions to those presented in Table 4.3 for $O_2(a^1\Delta_g)$ are more exothermic by 0.98 eV, the excitation energy of the excited state (15).

Consideration of the collision process between M and O_2 suggests that the encounter complex will be MO_2^* where the asterisk denotes the energy of bond formation still present in the complex i.e. it has not been stabilised. The excess energy may be removed for example, by collision with a third body or by ionisation. The fate of the collision complex, assumed to be long lived, determines the products of the reaction and is the basis of the proposed thermodynamic model. Some possible reactions of the long lived complex are presented in Table 4.4 with their reaction enthalpies calculated from available thermodynamic data. Reactions 1 and 5 of Table 4.4 correspond to autoionisation of the collision complex to form $MO_2^+ + e^-$ and this process is attributed to Band I observed in the spectra for the reactions of Ca and Sr with ground state molecular oxygen. The data underlined in Table 4.4 are the observed high kinetic energy onsets of Band I in each case. This is consistent with the approximation that the available reaction enthalpy departs with the electron, equation 2.4 of Chapter 2. Consequently the high kinetic energy onset may be equated with the reaction enthalpy. However there is a larger experimental error in determining the high kinetic energy onset than the band maximum for both Sr and Ca with $O_2(X^3\Sigma_g^-)$ as it is obscured by the fifth oxygen calibration band and must be calibrated with the fourth oxygen band.

Reactions 2 and 6 in Table 4.3 are available reaction channels leading to the formation of O_2^- (a stable thermodynamic species (16)) which is attributed to Band II as observed in the spectra recorded for the M + $O_2(X^3\Sigma_g^-)$ reactions. This is consistent with the evidence which distinguishes behaviour of Band II and the photoelectrons by their magnetic field dependence. Further this may explain why Band II is calibrated as having very low or apparent negative energy and also its observed variation in position. The validity of this assignment will be considered later. The small band observed when the $O(^3P)$ concentration is high is also attributed to ions formed by process 9 of Table 4.4.

Literature support for these assignments can only be provided for the Ba + $O_2(X^3\Sigma_g^-)$ reaction. From studies of this reaction there is some evidence for the formation of a long-lived gas phase BaO_2 intermediate (5,6,7). This was proposed on the basis of observed forward-backward symmetry in the angular distribution of the BaO product from the reaction Ba + O_2. The observed product distribution symmetry can be explained in terms of a long-lived collision intermediate with a lifetime longer than the rotational period of the collision complex (7). BaO_2 has also been inferred from chemiluminescence studies of the Ba + $O_2(X^3\Sigma_g^-)$ reaction at high total pressures (10^{-3} torr.) (17). From these investigations the bond energy of BaO_2 has been estimated within the range 2.38 - 6.50

Table 4.4

Possible reactions of a long-lived collision complex $[MO_2]^*$ with calculated reaction enthalpies from available thermodynamic data.

$$M + O_2 \rightarrow [MO_2]^*$$

$M + O_2(X^3\Sigma_g^-)$	Ca	Sr	Ba	Ref.
(1) $[MO_2]^* \rightarrow MO_2^+ + e^-$	-0.8±0.2	-1.4±0.2	+0.2±0.5	(a)
(2) $[MO_2]^* + O_2 \rightarrow MO_2^+ + O_2^-$	-1.2±0.2	-1.8±0.2	-0.2±0.5	(b)
(3) $[MO_2]^* + O_2 \rightarrow MO_2 + O_2$	-	-	-5.2±0.4	(c)
(4) $[MO_2]^* + O_2 \rightarrow MO + O_2 + O$	+1.17±0.05	-	-5.2±0.4	(c)
$M + O_2(a^1\Delta_g^-)$				
(5) $[MO_2]^{**} \rightarrow MO_2^+ + e^-$	-1.7±0.2	-2.2±0.2	-0.8±0.5	(a)
(6) $[MO_2]^{**} + O_2 \rightarrow MO_2^+ + O_2^-$	-2.1±0.2	-2.7±0.2	-1.2±0.5	(a,c)
(7) $[MO_2]^{**} + O_2 \rightarrow MO_2 + O_2$	-	-	-5.2±0.4	(c)
(8) $[MO_2]^{**} + O_2 \rightarrow MO + O_2 + O$	+0.76±0.05	-0.26±0.05	-1.56±0.05	(c)
$M + O(^3P)$				
(9) $[MO]^* + O_2 \rightarrow MO_2^+ + O^-$	-2.2±0.2	-2.8±0.2	-1.6±0.6	(c)

(a) All values underlined are determined in this work
(b) Reference 30
(c) Reference 29
(d) Reference 27
(e) Reference 28

eV, the most recent value (7), is 5.20 ± 0.43 eV determined by measuring the maximum translational energy of BaO_2 from the decay of a BaO_3 collision complex from the reaction Ba + O_3. This value is used in this work. BaO_2, SrO_2 and CaO_2 have also been observed in matrix isolation studies and their infrared spectra have been recorded (18,19) The vibrational spectra may be interpreted in terms of a molecule of C_{2v} symmetry. This conclusion is reached on the basis of observation of two equivalent O atoms within the molecule deduced from ^{16}O - ^{18}O isotopic studies. The observed frequency was found to be close to that of free O_2^- (19).

The shape of the observed electron energy distributions for Band I obtained from the reactions of Sr and Ca with $O_2(X^3\Sigma_g^-)$ may be interpreted by simple application of the two state potential energy curve model. The shape of the electron energy distribution is consistent with the classical turning point case, as described in Chapter 2. From the above discussion the geometry of all MO_2 molecules are assumed to be C_{2v}. The molecular orbital description of the electronic structure would predict a singlet ground state for a molecule of C_{2v} geometry since the number of electrons in the reacting atoms is even and a bent triatomic molecule has non-degenerate orbitals (whether of C_{2v} or of C_s symmetry) (20). Thus reactants approaching on a singlet potential energy surface may correlate with the ground state of MO_2. However, molecules approaching on a triplet surface will not correlate with the ground state but with a triplet excited state: spin must be conserved along the potential energy surface. This explains the lack of observed spectra for the reactions of Sr and Ca with $O_2(a^1\Delta_g)$. Here both reactants approach each other on a singlet potential energy surface which correlates with the ground state of MO_2 and collisional deactivation to the ground state can occur. This is in contrast to the Sr and Ca reactions with $O_2(X^3\Sigma_g^-)$ were the complex cannot undergo collisional deactivation to the ground state and may undergo autoionisation and collisional ionisation forming Bands I and II respectively. These simple ideas are presented in Figure 4.13.

This simple potential energy curve model neglects all interactions with other potential energy surfaces. One surface thought to be important in the reactions of alkali and alkaline metals with oxidants in the gas phase (21) is the ionic potential curve leading to a $M^+O_2^-$ ground state molecule. The ionic model has been shown to work very well for such reactions and is consistent with the observed electron spin resonance spectra of the alkali metal peroxides (21); studies of this type have yet to be extended to the alkaline earth metal peroxides. Infrared spectra recorded for both alkali and alkaline metals peroxides are consistent with a predominantly ionic ground state electronic structure (19). Transition to an ionic $M^+O_2^-$ potential energy surface from a covalent neutral surface is thought to occur at long range *via* an electron jump 'harpoon' mechanism (see Chapter 2). From equation 2.7, an estimate of the crossing internuclear separation may be obtained. The crossing point distances R_c in Figure 4.14, for Ba, Sr, and Ca reactions with $O_2(X^3\Sigma_g^-)$ can be calculated as

$$R_c(Ba) = 3.0 \text{ Å}, \; R_c(Sr) = 2.7 \text{ Å}, \; R_c(Ca) = 2.5 \text{ Å}$$

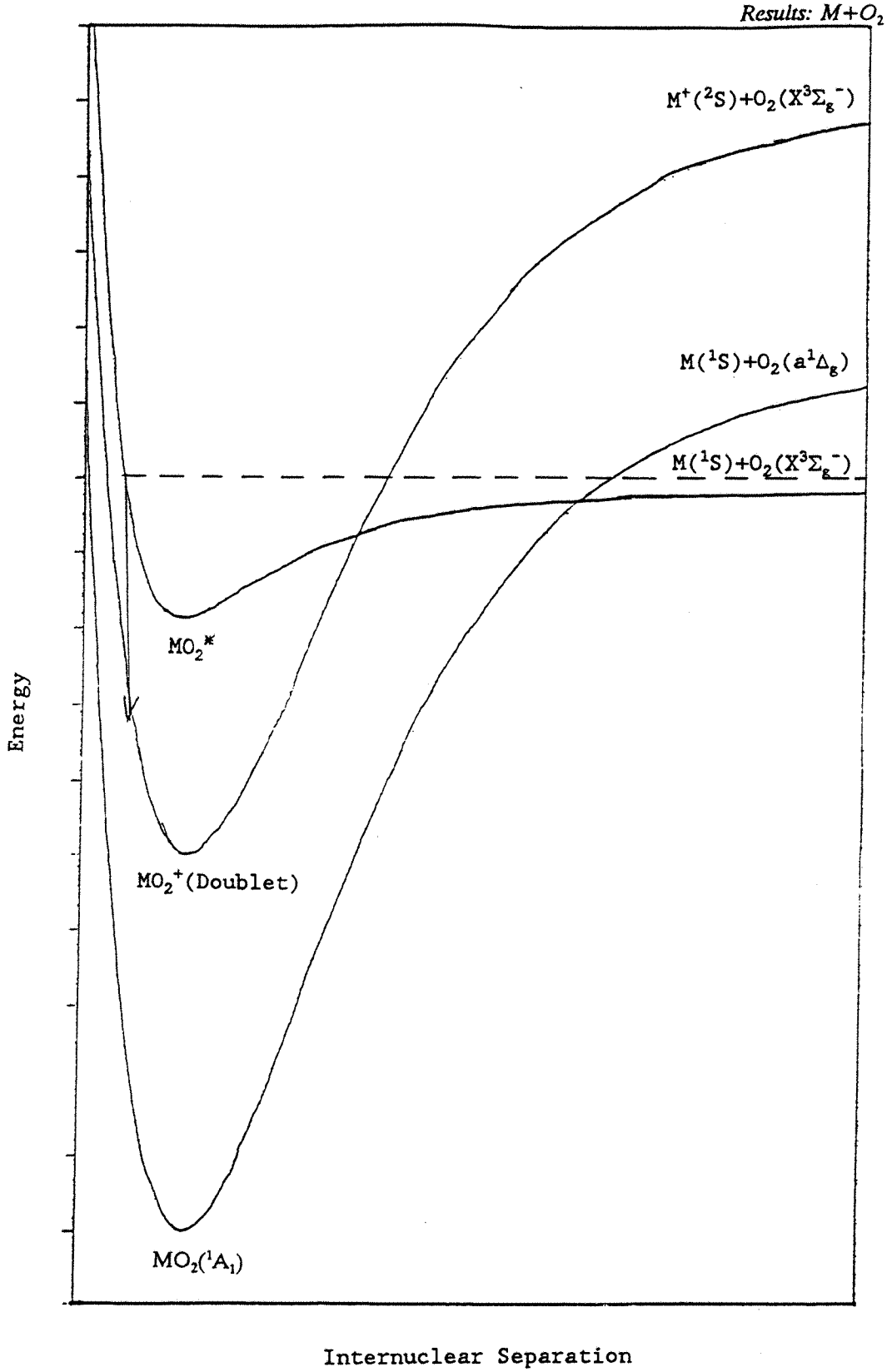

Figure 4.13 A potential energy diagram showing the simple classical turning point mechanism for the M + O_2 -> MO_2^+ + e^- electron energy distribution

from the first ionisation energies of the metals (22) and the electron affinity of O_2 (23). These are similar to crossing distances calculated elsewhere for the reactions of Ca with Cl_2 (24).

The refined potential energy model is presented in Figure 4.14 and forms a basis for the understanding of the reactions of the alkaline earth metals with both $O_2(X^3\Sigma_g^-)$ and $O_2(a^1\Delta_g)$. For the reaction of Sr and Ca with $O_2(X^3\Sigma_g^-)$ the ground state reactants approach on a triplet neutral surface. At about 3 Å the surface becomes predominantly ionic in character following an electron transfer - it remains of triplet spin multiplicity. The resulting complex is long-lived and may either autoionise emitting electrons detected as Band I or may be collisionally ionised forming negative ions detected as Band II. For the case of Ba + $O_2(X^3\Sigma_g^-)$ the collision complex formed must have a relatively low autoionisation cross-section but can be ionised on collision with O_2 to form the ions detected as Band II. For the reactions of Ca and Sr with $O_2(a^1\Delta_g)$ the two reactants approach on a singlet surface which correlates directly with the ground state of MO_2. Collisional quenching to form the stable ground state neutral is presumably kinetically favoured as no electrons or ions are seen from this reaction. Transition to a surface which is ionic in character may also occur at an internuclear separation dependent on the electron affinity of $O_2(a^1\Delta_g)$, and again spin will be conserved in this process.

The results obtained for the reactions involving Ba are different to those of Ca and Sr in that reaction with either $O_2(X^3\Sigma_g^-)$ or $O_2(a^1\Delta_g)$ led to similar spectra. Band II in the Ba reaction with an $O_2(a^1\Delta_g)/O_2(X^3\Sigma_g^-)$ mixture is reduced in intensity relative to that observed for the Ba + $O_2(X^3\Sigma_g^-)$ reaction, consistent with the reduced partial pressure of $O_2(X^3\Sigma_g^-)$ after discharge. Thus the reaction of Ba with $O_2(a^1\Delta_g)$ does not appear to be sufficiently fast to remove the available barium for the Ba + $O_2(X^3\Sigma_g^-)$ reaction as appears in the Ca and Sr cases.

It is possible that another neutral reaction should also be considered to explain the results shown in Figure 4.12. The reaction

4.2 $$M + O_2(a^1\Delta_g) \rightarrow MO + O$$

is likely to be rapid and may remove gas phase metal atoms that could react with $O_2(X^3\Sigma_g^-)$ and give rise to Bands I and II via reactions 1 and 2 of Table 4.4. If such a reaction were fast then it would quickly remove the metal which would no longer be available to react by other processes. However if this reaction were fast it would lead to a large concentration of O atoms which would further react with the metal to form the band observed when $O(^3P)$ is produced from the discharge. Whilst this reaction is exothermic (Table 4.3), there is no evidence to support its involvement in rationalising the spectra shown in Figure 4.12,as the bands are not observed for the Sr + O and Ca + O reactions in the absence of discharge oxygen atoms.

The ion spectra measured for the Ba and Sr reactions with $O_2(X^3\Sigma_g^-)$ showed only the presence of O_2^+ attributable to secondary ions formed because of the extraction voltages used (see Chapter

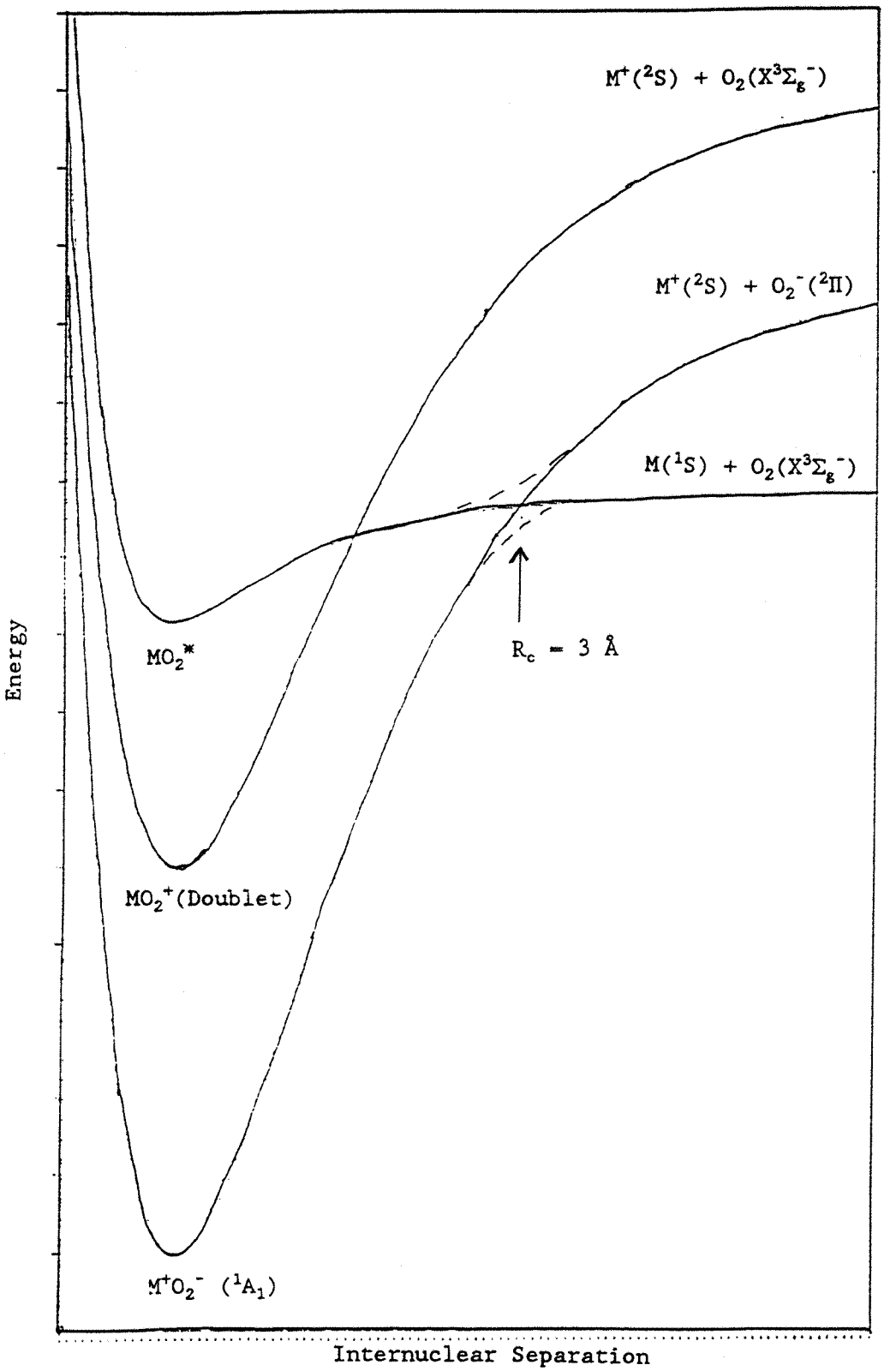

Figure 4.14 A schematic potential energy curve diagram showing a crossing R_c, between an ionic surface and a covalent neutral surface. MO_2 is assumed to be of C_{2v} symmetry.

3). However the ion spectrum for the reaction Ca + $O_2(X^3\Sigma_g^-)$, presented in Figure 4.9, shows signals that may be attributed to Ca^+, m/z = 40, O_2^+, m/z = 32 and CaO^+, m/z = 56. (Other signals were also observed at m/z = 48, 44, 42, corresponding to the natural isotopic abundance of Ca.) These are inconsistent with the primary ions formed in the reaction as expected from the thermodynamic model. The extraction voltages required for the observation of these ions were very high such that any primary ions formed may have up to 20 eV of translational kinetic energy. Under such extraction conditions at the pressures used, secondary ion-molecule reactions are likely to occur. The observed signal intensities are consistent with the following secondary ion reaction scheme:

4.3 $$CaO_2^+ + X \rightarrow Ca^+ + O_2 + X$$

4.4 $$Ca + CaO_2^+ \rightarrow CaO + CaO^+$$

4.5 $$CaO_2^+ + O_2 \rightarrow CaO_2 + O_2^+$$

where X is a third body, likely to be O_2. The secondary ion process investigated for the lanthanum reaction in Chapter 3 must also be considered. For CaO_2^+ this would be

4.6 $$CaO_2^+ + O_2 \rightarrow CaO_2^+ + O_2^+ + e^-$$

The pressure dependence of the ion intensities has not been studied although this may provide useful experimental information which will assist in determining the reaction scheme. Ultimately, however, positive support for the thermodynamic model would come from detection of the primary ions, MO_2^+. Clearly under the conditions used the detection of primary ions will be difficult since to avoid ion-molecule reactions extraction voltages will have to be low and the extraction efficiency will consequently be poor.

A thermodynamic model has been used to explain the experimental chemi-electron spectra but no allowance has been made for the rates of consecutive reactions that are thought to occur in the reaction cell. However the model used does not explain the observed variation in ion signal or electron signal intensity with oxygen partial pressure and furnace temperature. It does however require the MO_2^* reaction intermediate to live long enough to react *via* consecutive reactions. The number of possible reactions within the reaction cell is dependent on the mean free path of the complex and the experimental pressure. Estimating the collision cross-section ($\approx 10^{-18}$ m^2) and a pressure of 10^{-3} torr in the reaction cell, the mean free path of the MO_2^* complex is calculated to be of the order of ≈2mm. Thus the complex will almost certainly undergo a number of collisions giving rise to ions or electrons which leave the reaction cell or ion lens for detection. Hence the kinetic properties of the reaction mixture will be dependent on a consecutive reaction scheme.

A simple consecutive reaction scheme may be constructed and is presented here to form the basis of a qualitative explanation of the observed pressure dependence of O_2^- formed by reaction 2 of Table 4.4, Band II. The reaction scheme is as follows:

4.7	$M + O_2 \rightarrow MO_2^*$	k_1
4.8	$MO_2^* + O_2 \rightarrow MO_2^+ + O_2^-$	k_2
4.9	$MO_2^* + X \rightarrow$ Products	k_3

Reaction 4.7 is the initial formation of the collision complex proceeding with rate constant k_1, reaction 4.8 is the process leading to O_2^- formation with rate constant k_2, and reaction 4.9 represents all other reactions leading to loss of the collision intermediate including the autoionisation process leading to Band I and the neutral reaction 4.2. With the assumptions that the partial pressure of O_2 is constant, and the initial concentration of the metal $[M]_{t=0} = M_0$, and <u>not</u> in a steady state regime it is possible to construct a differential equation for the time dependence of $[O_2^-]$. Solution of this differential equation leads to the following expression for the variation of $[O_2^-]_t$ with time

4.10 $$[O_2^-]_t = (k_1k_2M_0/\beta)\{1/\beta \exp(-\beta O_2 t) - 1/\alpha \exp(-\alpha O_2 t)\}$$

where $\alpha = k_2+k_3$ and $\beta = k_1-\alpha$. The form of equation 4.10 for a constant reaction time and different partial pressures of oxygen, is consistent with the shape of Figure 4.3 or Figure 4.6 showing a partial oxygen pressure at which the yield of O_2^- is greatest. The optimum pressure is determined by the values of α and β.

The observations of band intensity change with temperature is particularly pronounced for the reaction of Ca with $O_2(X^3\Sigma_g^-)$. At lower temperatures, 1000 K, the spectrum contains two bands labelled Bands I and II as presented in Figure 4.9(a) but as the temperature is increased to 1500 K Band II disappears completely as shown in Figure 4.10. This might suggest some variation on autoionisation lifetime with temperature, becoming shorter at higher temperature, making the reaction faster than that leading to the production of negative ions, Band II. This is also observed for the reactions of Sr with $O_2(X^3\Sigma_g^-)$ but the effect is less pronounced; Bands I and II are present at all temperatures investigated, Band I being favoured at higher temperatures.

The stability of the autoionising state may also explain the very different reactions of Ba with $O_2(X^3\Sigma_g^-)$ and $O_2(a^1\Delta_g)$, see Figure 4.12. Thus the reaction leading to Band II dominates for all oxidant mixtures even when the autoionisation reaction process 5 of Table 4.4 is exothermic as for Ba + $O_2(a^1\Delta_g)$. The role of kinetics in the reactions of the alkaline earth metals and oxidants is important under the conditions used and needs to be considered with the thermodynamic model for a complete understanding of the reactions investigated.

4.8 Conclusions.

In this work, a study of the reactions of the alkaline earth metals Mg, Ca, Sr and Ba with $O_2(X^3\Sigma_g^-)$, $O_2(a^1\Delta_g)$ and $O(^3P)$ by electron spectroscopy has been presented along with preliminary ion mass spectrometric results. The electron spectra are interpreted using a thermodynamic model of the reaction scheme based on the existence of a long lived collision complex $M\text{-}O_2^*$. There is some

independent evidence for the stability of the $M\text{-}O_2^*$ species from an argon matrix isolation study and from gas phase studies of the reaction Ba + $O_2(X^3\Sigma_g^-)$ under molecular beam conditions. The reaction enthalpies for the reactions

4.10 $$M + O_2 \rightarrow MO_2^+ + e^-$$

are not available for all the metals Ca, Sr, and Ba and this study represents the first estimation of these reaction enthalpies, see in Table 4.2.

The results obtained in this work disagree with those obtained from initial investigations performed by electron spectroscopy (9). In the previous study, only one band was observed for the reactions of Ba and Sr with $O_2(X^3\Sigma_g^-)$ with calibrated band maxima 0.56±0.04 eV and 0.83±0.03 eV respectively. Re-inspection of the spectra shows a band shape and structure very similar to Band II observed in this study. Further, the calibration involved a large extrapolation with a consequently large error. In the present study, the position of Band II was found to vary for different experiments and this effect together with the poor calibration of reference (9) suggests the spectra from the previous investigation were observations of Band II for each reaction with a large calibration error.

A thermodynamic model has been constructed on the assumption that the reaction occurs between the atomic metal and the oxidant without regard to small partial pressures of other species that may be present in the vapour phase. Evaporation of the metal sample will however include some small partial pressures of metal oxide components due to surface oxidation of the sample during preparation. Evaporation of alkaline metal monoxides leads to a mixture of vapour phase components consisting predominantly the atomic metal but also metal suboxides, superoxides and peroxides depending on the oxygen partial pressure above the solid. Small partial pressures of other species may affect the chemistry within the consecutive reaction regime.

To determine the possible role of a metal monoxide in gas phase oxidation reactions of the alkaline earth metals, a series of experiments evaporating the $MO_{(s)}$ is planned. Preliminary investigations suggest that a gas phase reaction of the type MO + $O_2(X^3\Sigma_g^-)$ (where M = Ca,Sr,Ba) lead to observed electron spectra. The observed bands may arise from the reaction of atomic metal with the oxidant, the metal being formed by decomposition of the monoxide on heating. A further possible reaction involving the monoxides of Ba and Sr which produces electrons (25) is the reaction with water. These reactions will also form the basis of another study but preliminary investigations have shown that CaO, SrO and BaO react in the vapour phase with water to form electrons of ≈2 eV kinetic energy - the atomic metals have been shown not to react with water.

Investigation of the reactions of trace vapour components with oxygen and water is important if these components undergo chemi-ionisation reactions. These chemi-ionisation reactions in general may have large reaction cross-section and thus small partial pressures of other gas phase species may have a large effect on observed electron spectra. Band III observed in the reaction Sr + $O_2(X^3\Sigma_g^-$) has been shown to be independent of the oxygen pressure but may arise from the reaction of vapour species formed on evaporation of samples with oxidised surfaces.

The performance of the modified instrument throughout the investigation has been encouraging. The re-designed furnace assembly has worked well producing stable evaporations over longer periods than could previously be achieved. The sensitivity of the electron spectrometer has been enhanced by the inclusion of the reaction cell which has further allowed the advantages of pre-acceleration to be exploited. The ion spectrometry has been a little disappointing. The ion lens system and the quadrupole mass spectrometer have worked well together for the La + $O_2(X^3\Sigma_g^-)$ investigations described in Chapter 3, but have been less successful for the reactions of the group II metals where no primary ions were observed. This may however be a property of the ion-molecule chemistry of the group II gas phase metal oxidation reactions studied and further experimentation will be required to resolve this problem satisfactorily.

Further instrumental development will be necessary for the detection of both positive and negative primary ions. Modification of the mass spectrometer to enable the detection of both positive and negative ions is planned. The behaviour of negative ions relative to electrons in a magnetic field will also be studied and some computer modelling is underway to compute the magnetic field effects on electron and ion trajectories. This will be useful to quantify observed changes in band positions and intensity on field variation.

This work has suggested that the reaction below is another candidate for inclusion into the steady state model of upper atmosphere metal-oxygen reactions presented in Table 4.1.

4.10 $$M + O_2 \rightarrow MO_2^+ + e^-$$

It is a possible source of MO_2^+ ions for the alkaline earth metals (cf.reaction 2, Table 4.1). Study of the reactions of Ca^+ with O_2 leading to the formation of CaO_2^+, by flowing afterglow techniques, suggests that ion molecule reaction routes to this ion are not significant. The reaction

4.11 $$Ca^+ + O_2 + He \rightarrow CaO_2^+ + He$$

has a rate constant thought to be $k < 2\times10^{-30}$ cm^6 $molecule^{-2}$ s^{-1} (26) and consequently will be very slow. However, reaction 4.10 is likely, by analogy with other associative ionisation reactions, to be fast, possibly gas kinetic and represents an efficient route to MO_2^+ for the alkaline earth metals in the upper atmosphere.

In conclusion, reactions of the alkaline earth metals with $O_2(X^3\Sigma_g^-)$, $O_2(a^1\Delta_g)$ and $O(^3P)$ have been studied and interpreted in terms of a thermodynamic model based on a long-lived collision intermediate. For the reactions of the metals with $O_2(X^3\Sigma_g^-)$ the observed spectra are consistent with the following reaction scheme:

$$M + O_2(X^3\Sigma_g^-) \rightarrow MO_2^* \rightarrow MO_2^+ + e^- \quad \text{Band I}$$
$$\rightarrow MO_2^* + O_2 \rightarrow MO_2^+ + O_2^- \quad \text{Band II}$$

Observed pressure dependencies are consistent with a kinetic model based on this reaction regime.

The reactions of Ca and Sr with $O_2(a^1\Delta_g)$ show no observable bands in their electron spectra consistent with conservation of spin along the potential energy surface forming a stable peroxide $M^+O_2^-$ of C_{2v} symmetry in its singlet ground state. The reaction of Ba with $O_2(X^3\Sigma_g^-)$ proceeds at a comparable rate to the neutral channels involving Ba + $O_2(a^1\Delta_g)$, and the electron spectrum seen for Ba + $O_2(X^3\Sigma_g^-)$ is observed for all oxidant mixtures.

The reactions of Ca and Sr with $O(^3P)$ produce spectra consistent with the formation of negative ions from the following reaction:

$$M + O(^3P) \rightarrow MO^* + O_2 \rightarrow MO_2^+ + O^-$$

No bands were seen in the electron spectrum for the Ba + $O(^3P)$ reaction although it may be masked by the band formed from Ba + $O_2(X^3\Sigma_g^-)$ reaction.

Several issues remain to be resolved before this study of the alkaline earth metal gas phase oxidation reactions is complete. Direct detection of the primary ionic products, whether positive or negative, needs to be made before the proposed reaction regime can be confirmed. The role of kinetics needs to be further investigated. When these studies have been undertaken the conclusions of the work will be of direct importance to the understanding of meteor chemistry.

References

(1) E.Murad. *J.Geophys.Res.* 83,5525,(1978).

(2) W.Swider. *Planet.Space.Sci.* 17,1233,(1969).

(3) D.R.Herschbach. Nobel Lecture. *Angw.Chem.* 26,1221,(1987).

(4) (a) R.B.Cohen, C.S.Young, & S.Wexler. *Chem.Phys.Lett.* 19,99,(1973).

(b) H-J.Meyer, Th.Schulze & U.Ross. *Chem.Phys.* 90,185,(1984).

(c) R.B.Cohen,P.Majeres & J.Raboff. *Chem.Phys.Lett.* 32,176,(1975).

(d) G.J.Diebold, F.Eagelebe, H.U.Lee, J.Whitehead & R.Zare. *Chem.Phys.* 30,265,(1977).

(e) U.Ross, H-J.Meyer & Th.Schulze. *Chem.Phys.* 84,359,(1984).

(f) R.H.Burton, J.H.Brophy C.A.Minis, & J.Ross. *J.Chem.Phys.* 73,1612,(1980).

(5) P.J.Dagdigian, H.W.Cruse, A.Schultz R.N.Zare. *J.Chem.Phys.* 61,4450,(1974).

(6) T.P.Parr, A.Freedman, R.Bahrens, R.Herm. *J.Chem.Phys.* 72,5163,(1980).

(7) H.F.Davis, A.G.Suits, H.Hou, Y.T.Lee. To be Published (1990).

(8) D.Husain & G.Roberts. *Chem.Phys.* 138,187,(1989).

(9) M.Feher. PhD Southampton University (1987).

(10) W.J.Van Der Meer, P.Van der Menlen, M.Volmer & C.A.DeLange. *Chem.Phys.* 126,385,(1988).

(11) G.C.Allen, P.M.Tucker, B.E.Hayden & D.F.Klemperer. *Surface.Sci.* 102,207,(1981).

(12) A.N.Nesmeyanov in *Thermodynamic Reference Tables.* Ed. R.Gray. Elseveir, London (1963).

(13) G.Verhagen, R.Colin, G.Exsteen & J.Drowart. *Trans.Faraday.Soc.* 61,1372,(1965).

(14) (a) R.H.Lamoreaux, D.L.Hildenbrand & L.Brewer. *J.Phys.Chem.Ref.Data.* 16,419,(1987).

(b) J.B.Pedley & E.Marshall. *ibid* 12,967,(1985).

(15) G.Herzberg & K.P.Huber. *Constants of Diatomic Molecules.* Van Nostrand, New York (1979)

(16) Sir Harrie Massey. *Negative Ions.* C.U.P. 3rd Ed (1976).

(17) J.M.Mestdagh *et al.* *Chem.Phys.Lett.* 164,5,(1989).

(18) S.Abramovitz & N.Aquista. *J.Res.Nat.Bureau.Stan.* USA 75,23,(1971).

(19) (a) L.Andrews & B.S.Ault. *J.Mol.Spec.* 68,114,(1977).

(b) L.Andrews & B.S.Ault. *J.Chem.Phys.* 62,2312(1975).

(c) L.Andrews & B.S.Ault. *J.Chem.Phys.* 62,2320(1975).

(20) D.A.Dixon, D.D.Parrish, D.R.Herschbach.
Faraday.Disc.Chem.Soc. 55,385,(1973).

(21) D.R.Herschbach & D.M.Lindsay. *Chem.Phys.Lett.* 25,175,(1974).

(22) C.E.Moore. *Atomic Energy Levels* Nat.Bureau.Standards (1949).

(23) M.J.Travers, D.C.Cowles & G.B.Ellison. *Chem.Phys.Lett.* 164,449,(1989).

(24) M.Menzinger in *Gas Phase Chemiluminescence and Chemi-ionisation.*
Ed. A.Fontijn. North Holland, Amsterdam (1985).

(25) J.M.Dyke, M.Feher, B.W.J.Gravenor & A.Morris.
J.Am.Chem.Soc. 91,4476,(1987)

(26) K.G.Spears & F.C.Fehsenfeld. *J.Chem.Phys.* 56,5698,(1972)

Table References.

(27) U.S. Air Force Report. AFGL-TR-77-0235 E.Murad (1985).

(28) (a) M.J.Travers, D.C.Cowles & G.B.Ellison.
Chem.Phys.Lett. 164,449,(1989).
(b) L.M.Branscomb. *Phys.Rev.* 111,504,(1958)

(29) H.F.Davis, A.G.Suits, H.Hou, Y.T.Lee. To be Published (1990).

(30) R.B.Cohen, C.S.Young, & S.Wexler. *Chem.Phys.Lett.* 19,99,(1973).

Concluding remarks and prospects for future work.

The study of chemi-ionisation reactions by chemi-electron and chemi-ion spectroscopy has been developed in this thesis and extended to the reactions of the alkaline earth metals with $O_2(X^3\Sigma_g^-)$,$O_2(a^1\Delta_g)$ and $O(^3P)$. The observed spectra are consistent with the reactions proceeding *via* a long-lived collision intermediate. which is able to autoionise or react further by collision. These reaction channels compete with other available channels which lead to neutral products. From the observed spectra it has been possible to derive reaction enthalpies for the associative ionisation channel for the reactions of Sr and Ca with $O_2(X^3\Sigma_g^-)$. These reactions represent further possibilities for inclusion into a kinetic model of metal oxidation reactions in the upper atmosphere.

A number of problems remain unresolved in the study of alkaline earth metal reactions with oxygen, suggesting areas of further investigation. Other reactions will be of use in testing the thermodynamic model proposed to explain the M + O_2 results obtained. Preliminary investigations of the reactions of MO + $O_2(X^3\Sigma_g^-)$ for M = Ca, Sr and Ba suggest that these reactions also lead to ionic products, probably electrons at low kinetic energy. This work further complements the molecular beam studies of the Ba + O_3 reaction which is thought to proceed *via* a long-lived BaO_3^* intermediate. The MO + O_2 reactions may also proceed *via* an MO_3^* intermediate and a study of these reactions may complement results obtained on the M + O_3 systems. It should also be possible to carry out investigations on the M + O_3 reactions themselves to investigate possible chemi-ionisation channels.

Reactions of the alkaline earth metals with other oxidants may also be studied. Preliminary results suggest that Ba and Ca react with N_2O to produce electrons with a band centred at ≈4 eV electron kinetic energy but this result requires further study. Chemi-ionisation reactions of the metals Ba, Sr, and Ca with OH are also known to occur but these have not been studied by chemi-electron spectroscopy. Preliminary results suggest there may be a small reaction with discharged water but a simple discharge of water is a poor source of OH.

The reactions that will be studied first as a continuation of the present study are the reactions of the alkaline earth metal oxides with water. These produce a single asymmetric electron band from the reaction MO + H_2O, for M = Ca, Sr and Ba. The reactions of Sr and Ba have been previously studied and found to have band maxima at 1.76 ± 0.05 eV and 1.56 ± 0.05 eV respectively, although these values must be regarded as uncertain as they depend on a long extrapolation (reference 9 Chapter 4). These values compare with preliminary measurements in this work which suggests the band maxima are 0.8 ± 0.5 eV for CaO + H_2O, 0.6 ± 0.5 eV for SrO + H_2O, and 0.4 ± 0.5 eV for BaO + H_2O. The uncertainty in these data arises from the calibration. The HeIα

photoelectron spectrum of water does not contain a calibration band close to the chemi-electron bands and consequently the extrapolation error is large. To improve these data an inert calibrant, e.g. N_2, will have to be used. It is likely these reactions are

$$MO + H_2O \rightarrow M(OH)_2^+ + e^-$$

and it should be possible to study these simple reactions by both chemi-electron and chemi-ion spectroscopy.

Reactions of other metals with oxidants have been studied previously in this laboratory, notably the reaction of lanthanide metals with oxygen. This work may be extended to include the reactions of the lanthanides with N_2O. Preliminary results suggest both Ce and La react with N_2O producing spectra containing a number of bands at low kinetic energy. This will require further careful study.

With some small modifications to the furnace region it may be possible to extend the study of reactions of metals in their ground state to metals in an excited state. An electric discharge at the base of the furnace assembly would produce a yield of metal atoms in excited states. The disadvantage with this technique is its lack of state selectivity for the metal but this would provide a simple extension of the range of reactions available for study.

The instrument has performed well throughout the period of this work, especially encouraging has been the success of the high temperature flange. With extended evaporation times now available, the prospects for performing parallel chemi-electron, chemi-ion spectroscopy experiments are promising. This will require the design of an ion lens capable of extracting simultaneously the electrons and ions in opposite directions. Once this has been achieved direct correlation of electron bands and ion signals will be possible to determine the primary ionic products of a reaction.

Development is also possible on the theoretical interpretation of an observed electron energy distribution to derive more information about the reaction mechanism other than the high kinetic energy onset derived at present. This could be coupled with some *ab initio* calculations on the states involved which should be possible for systems containing lighter atoms e.g. CaO_2 and CaO_2^+.

In conclusion, chemi-electron and chemi-ion spectroscopy have shown great potential for the study of gas phase reactions producing ionic products. Improvements to the instrument will allow better quality data to be acquired and development of the theoretical methods should allow an improved understanding of chemi-ionisation reactions.